LOW TEMPERATURE ELECTRICAL AND MAGNETIC CHARACTERIZATION OF SUPERCONDUCTING-FERROMAGNETIC THIN FILMS DEPOSITED BY VARIOUS PHYSICAL VAPOR DEPOSITION TECHNIQUES

by

Erhan ONGUN

A dissertation submitted to

the Graduate Institute of Science and Engineering

of

Melikşah University

in partial fulfillment of the requirements for the degree of

Doctor of Philosophy

in

Materials Science and Mechanical Engineering

March 2016
Kayseri, Turkey

APPROVAL PAGE

This is to certify that I have read the dissertation titled "Low Temperature Electrical and Magnetic Characterization of Superconducting-Ferromagnetic Thin-Films Deposited by Various Physical Vapor Deposition Techniques" by Erhan ONGUN and that in my opinion it is fully adequate, in scope and quality, as a dissertation for the degree of Doctor of Philosophy in Materials Science and Mechanical Engineering, the Graduate Institute of Science and Engineering, Melikşah University.

_____

March 11, 2016 Asst. Prof. Dr. Ali Esad ÖZMETİN
Supervisor

I certify that this dissertation satisfies all the requirements as a dissertation for the degree of Doctor of Philosophy.

_____

March 11, 2016 Assoc. Prof. Dr. Ercan ŞEVKAT
Head of Department

Examining Committee Members

Title and Name		Approved
Asst. Prof. Dr. Ali Esad ÖZMETİN	March 11, 2016	_____
Assoc. Prof. Dr. Ercan ŞEVKAT	March 11, 2016	_____
Assoc. Prof. Dr. Mehmet HANÇER	March 11, 2016	_____
Assoc. Prof. Dr. Fehmi NAİR	March 11, 2016	_____
Assoc. Prof. Dr. Murat ÇITIR	March 11, 2016	_____

It is approved that this dissertation has been written in compliance with the formatting rules laid down by the Graduate Institute of Science and Engineering.

_____

Asst. Prof. Dr. M. Evren SOYLU
Director
March 11, 2016

LOW TEMPERATURE ELECTRICAL AND MAGNETIC CHARACTERIZATION OF SUPERCONDUCTING-FERROMAGNETIC THIN FILMS DEPOSITED BY VARIOUS PHYSICAL VAPOR DEPOSITION TECHNIQUES

Erhan ONGUN

PhD Dissertation - Materials Science and Mechanical Engineering
March 2016

Supervisor: Asst. Prof. Dr. Ali Esad ÖZMETİN

ABSTRACT

The mutual interaction between ferromagnetism and superconductivity states has been investigated in a coupled ferromagnetic/superconducting thin-film structure, the so-called F/S hybrid. A typical F/S hybrid has been designed and built-up of a layer of magnetic substructures overcoated with thin superconducting film, and electrical contact pads atop on silicon substrate. Ferromagnetic and superconducting films have been spatially separated by ultrathin Al_2O_3 insulating barrier.

Thermal & sputter combined physical vapor deposition techniques and various topographic micro-patterning processes have been utilized. The magnetically soft permalloy substructures have been grown in a pattern of periodic alternating stripes along and across the current flow direction. Thin superconducting $Pb_{82}Bi_{18}$ films have been grown by thermal-evaporation and quench-condensation mechanism at substrate temperature of 77 K. Using standard four-point probe transport measurement technique, I-V data streams have been collected at temperatures in the range of 3-10 K while the samples have been swept under an externally applied magnetic field from zero to 7 kOe.

It has been observed that the artificial periodic modulation of magnetic field in the superconducting film results in various T_C and H_{C2} (T) values exclusive to each sample. Dependent on the orientation of magnetic stripes in paralel or perpendicular to the current flow direction, the superconducting properties can be controlled, and also the F/S hybrid can be switched between superconducting and normal conducting states. The directional current flow dependency behavior can be used to realize a functional F/S device such as a low-power persistent current switch for superconducting applications.

Keywords: Physical Vapor Deposition, Ferromagnetic/Superconducting Hybrids, Low Temperature Transport Measurements, Scanning Hall Probe Microscopy.

FİZİKSEL BUHAR BİRİKTİRME TEKNİKLERİ İLE ÜRETİLEN SÜPERİLETKEN-FERROMANYETİK İNCE-FİLMLERİN DÜŞÜK-SICAKLIKTA ELEKTRİKSEL VE MANYETİK KARAKTERİZASYONU

Erhan ONGUN

Doktora Tezi – Malzeme Bilimi ve Makine Mühendisliği
March 2016

Tez Yöneticisi: Yrd. Doç. Dr. Ali Esad ÖZMETİN

ÖZ

Ferromanyetik/süperiletken (F/S) hibrit ince-filmlerin ferromanyetik ve süperiletken davranışları arasındaki karşılıklı etkileşim araştırıldı. Manyetik alt yapıların üzerine kaplı süperiletken ince film ve elektrik kontak uçlarından teşekkül eden tipik bir F/S hibrit yapısı tasarlandı ve üretildi. Manyetik altyapılar ile süperiletken üst katman arasında ince bir Al_2O_3 bariyeri ile yalıtım sağlandı.

Isıl buharlaştırma ve mıknatıslı saçtırma kaynağı kullanılarak fiziksel buhar kaplama teknikleri ve farklı topografik mikro desenleme metotları kullanıldı. Ferromanyetik permalloy alt yapılar, akım akış yönüne paralel ve dik yönlenmelerde olacak şekilde periyodik ardışık şerit desenlerde büyütüldü. İnce süperiletken $Pb_{82}Bi_{18}$ film, ısıl-buharlaştırma ve soğuk-yoğunlaşma mekanizması ile 77 K altlık sıcaklığında büyütüldü. Sıcaklık kontrollü dört-nokta temaslı iletkenlik ölçüm tekniği kullanılarak, 3-10 K arasında ve 0-7 kOe harici manyetik alan etkisi altında I-V ölçümleri yapıldı.

Süperiletken film üzerinde mikro ölçekte oluşturulan periyodik manyetik alan modülasyonu ile her bir süperiletken numunede farklı T_C ve H_{C2} (T) değerlerinin oluştuğu gözlemlendi. Süperiletken film üzerinden geçirilen akım yönüne referansla, manyetik mikro şeritlerin paralel veya dik olarak yönlenmesine bağlı olarak süperiletkenlik davranışının kontrol edilebildiği, böylece süperiletkenlik ile normal iletim durumları arasında anahtarlama yapılarak yönsel akım bağımlılığı davranışının fonksiyonel bir F/S hibrit tasarımında, örneğin düşük-güç tüketimli süperiletken anahtarda, kullanılabileceği ölçüm sonuçlarından anlaşıldı.

Anahtar Kelimeler: Fiziksel Buhar Kaplama, Ferromanyetik/Süperiletken Hibrit, Düşük-sıcaklık İletkenlik Ölçümü, Düşük-sıcaklık Taramalı Hall Uç Mikroskopisi.

DEDICATION

To my parents

ACKNOWLEDGEMENT

First and foremost, I would like to express my sincere thanks and gratitude to my adviser, Asst. Prof. Dr. Ali Esad Özmetin, for his generous supports, theoretical, experimental and hands-on instructions, and guidance in my research studies.

I would like to express my sincere thanks and appreciation to the Joint PhD Program Coordinators; Prof. Dr. M. Halidun Keleştemur from Melikşah University and Assoc. Prof. Dr. Mehmet Hançer from Erciyes University, and to the Examining Committee Members; Assoc. Prof. Dr. Ercan Şevkat, Assoc. Prof. Dr. Fehmi Nair, Asst. Prof. Dr. Gökhan Özgür, and Assoc. Prof. Dr. Murat Çıtır.

I would like to express my sincere thanks to Assoc. Prof. Dr. Osman Şahin and Asst. Prof. Dr. Mehmet Solmaz for their cooperation in our research studies.

My colleagues Mehmet Kuru, Murat Serhatlıoğlu, and Dr. Engin Yazıcı are gratefully acknowledged for their helps, technical assistance and contributions as a whole for being great team players.

TABLE OF CONTENTS

LIST OF TABLES

TABLE

LIST OF FIGURES

FIGURE

LIST OF SYMBOLS AND ABBREVIATIONS

SYMBOL/ABBREVIATION

F/S Hybrid	Ferromagnetic/Superconducting Hybrid
Py	Permalloy (Fe/Ni alloy)
PbBi	Lead-bismuth alloy
S-bridge	Superconducting thin-film
F	Ferromagnet
S	Superconductor
SEM	Scanning electron microscopy
EDX	Energy-dispersive X-ray spectroscopy
GIXRD	Grazing incidence X-ray diffraction
LT-SHPM	Low-temperature scanning Hall probe microscopy
STM	Scanning tunneling microscopy
AFM	Atomic force microscopy
PVD	Physical vapor deposition
DC	Direct current
RF	Radio frequency
T (K)	Temperature (Kelvin)
T_C (onset)	Superconducting critical transition temperature
H	Magnetic field (externally applied normal to the superconductor)
H_{C2}	Second critical field
MEMS	Micro electro-mechanical systems
QCM	Quartz crystal meter
RT	Room temperature (300K or 27°C)
LT	Low (cryogenic) temperature lower than 120K or -153°C

I/V	Current/Voltage
R	Resistance
mA	milliamp (1E-3 amp)
μA	microamp (1E-6 amp)
nm	nanometer (1E-9 m)
Oe	Oersteds (H-field in cgs units or amperes per meter in SI units)
IPA	Isopropyl Alcohol
DI	Distilled water

CHAPTER 1

INTRODUCTION

In the science and applications of thin-films, the magnetism and superconductivity are known to be great examples of mutually exclusive states. Within the last decade, the interplay between ferromagnetic and superconducting systems have been studied by experimental groups focusing on transport properties, and also imaging techniques have been employed.

As reported in [1-5], when combined in micron scale, the interplay between the stray field from the ferromagnetic substructures and the superconductor leads to unusual, exotic superconducting characteristics.

Several ferromagnetic/superconducting (F/S) hybrid systems have been studied both theoretically and experimentally in recent years [6-15]. Two comprehensive reviews are also available by Lyuksyutov and Pokrovsky [16], and by the Schuller group [17].

The main idea is to make ferromagnetic/superconducting (F/S) hybrids, where superconducting vortices can interact directly with the stray magnetic fields of the ferromagnetic substructures. Several experiments using arrays of magnetic dots or magnetic layers with lattice of holes deposited on top or under a superconducting film confirmed that ferromagnetic arrays substantially suppress vortex motion close to the critical transition temperature [17]. Also, it was reported that vortex pinning by magnetic domain walls could be a natural factor for increasing transport currents in continuous F/S hybrids [9, 11].

1.1 MAGNETIC THIN-FILMS

The magnetic properties of a bulk material differ from the identical material in thin-film form. Also, a patterned magnetic thin-film exhibits different magnetic properties from its flat film form. It was reported in [18] that size, shape, anisotropy and other properties determine the magnetic behavior of a patterned thin-film, and there is an increasing interest in making well-defined magnetic substructures in micron scale. The macroscopic properties of a thin-film material are influenced by the morphology (size & shape) of its constituent substructures, and also the fabrication techniques play an essential role in determining the electrical, magnetic, and mechanical properties.

Thin-films with magnetic substructures have many potential applications in various types of magnetic microsystems. They can operate as micro transducers, micro actuators, trapping devices, vibration energy harvesters, MEMS devices, and as solid state switches [19]. The use of these micro magnet arrays for trapping and confinement of magnetic micro objects is also being studied for lab-on-chip applications. Magnetic substructures behave as microflux sources and produce spatially modulated stray fields, which have many potential applications in the field of magnetic MEMS, and the manipulation and trapping of particles [20].

The preparation of thin-films of magnetic alloys is generally acknowledged to be a challenging task. Physical vapor deposition (PVD) techniques have proven to be suitable for the preparation of high quality magnetic thin-films [20]. To produce magnetic field distributions and field gradients, the magnetic films need to be patterned in micron scale using either topographic or thermomagnetic patterning techniques [19] followed by a heat treatment process to transform into ferromagnetic microstructure.

For characterization of stray magnetic fields produced by magnetic substructures, the scanning Hall probe microscopy (SHPM) technique [19] is used as well as to optimize the design of magnetic pattern. The spatial variation in field and field gradient over the magnetic substructures are measured. The transverse components of stray magnetic field distribution over the micro patterned film are measured. We shortly introduced the SHPM system and its basic principles of operation in Appendix-A.

1.2 SUPERCONDUCTING THIN-FILMS

Type I superconductors exhibit a complete flux expulsion behavior when the applied field is less than a certain critical field $H < H_C$. But, when H reaches H_C, the field becomes uniformly distributed across the cross section and superconductor is destroyed. Therefore, a type I superconductor features perfect diamagnetism provided that the field is smaller than the critical field H_C.

Type II superconductors do not exhibit perfect diamagnetism except for very weak applied fields $H < H_{C1}$ (Meissner Phase). On the other hand, they show partial flux expulsion maintaining the superconducting state within a certain field range $H_{C1} < H < H_{C2}$ (Vortex phase). In Vortex phase, the applied magnetic field starts to partially penetrate the superconductor. Partial flux penetration was first experimentally observed by Shubnikov in 1937, Figure 1.1. This phase is called the Shubnikov or Vortex state [24].

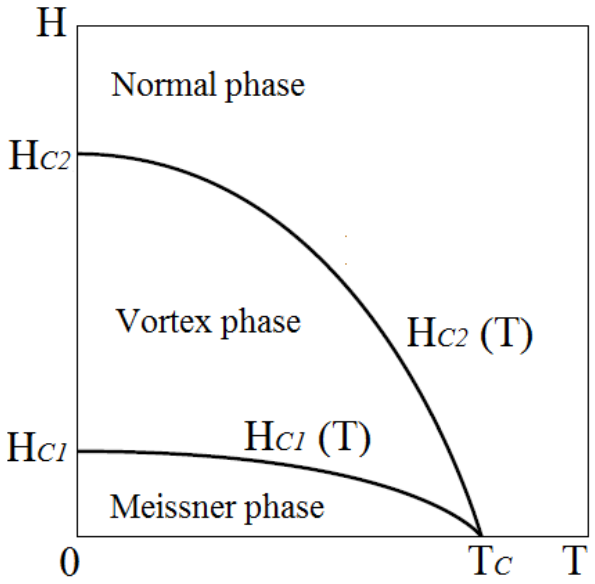

Figure 1.1: Phase diagram of a typical Type-II superconductor showing Meissner, Vortex, and Normal Phases [24].

In Vortex state, the applied field penetrates the specimen through quantized flux tubes called vortices. Each vortex has a normal core of radius on the length scale of coherence length and a supercurrent encircles this normal core. Supercurrent around each vortex generates one flux quantum of magnetic flux over the length scale of

coherence length. In the vortex state, the presence of vortices drastically modifies the magnetic and transport properties of the superconductor [24].

In case of an applied current (i), each vortex feels a Lorentz force perpendicular to the current flow direction and the applied field ($Ø_0$). In the absence of a balancing pinning force, the vortices will start moving in the direction of Lorentz force as shown in Figure 1.2.

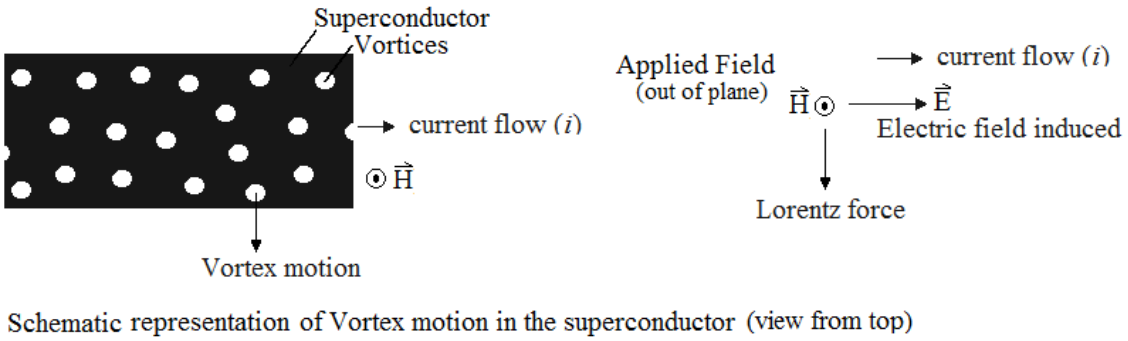

Figure 1.2: Schematic representation of Vortex motion in the superconductor (view from top). The applied field penetrates the specimen through quantized flux tubes called vortices. In case of an applied current (i), each vortex feels a Lorentz force perpendicular to the current flow and the externally applied magnetic field.

When the pinning forces are larger than the Lorentz force acting on the vortex, it will stay pinned in a particular location. These locations are called the pinning sites. Depending on the pinning energy and the vortex-vortex interaction, vortices can either stay in their random pinning sites forming a vortex glass or form an ordered lattice. This ordered lattice is referred to as the vortex lattice or Abrikosov Lattice [21, 22].

As the applied magnetic field or the current density increases, more and more vortices will leave their pinning sites and start moving under the influence of Lorentz force. Eventually, all the vortices will enter a steady flow state, in other words the superconductor will enter a vortex liquid phase.

As a result, moving vortices induce an electric field along the direction of the current density. There will be a form of resistive dissipation proportional to the applied field unless the vortices are prevented from moving or pinned.

1.3 MAGNETIZATION CONTROLLED SUPERCONDUCTIVITY

Another interdisciplinary field of research is highly focused on the mutual interaction between magnetism and superconductivity, and the exotic behaviors arise when these two states are combined in a hybrid structure as shown in Figure 1.3.

Due to relative high permeability of ferromagnetic substructures, the externally applied magnetic field is effectively channeled through the ferromagnetic pattern. The ratio of the flux lines channeled through the ferromagnetic substructures depends on the size and the period of these elements, and can be calculated as well as measured with scanning Hall probe microscope [19]. This channeling effect continues as the applied field is increased until the particular ferromagnetic material reaches saturation. Using this property, hybrid systems can be designed in such a configuration to form high and low magnetic field regions in the superconducting film. If this field variation is strong enough, parts of the superconductor can be driven normal resulting in a dependence of superconductor on current direction [24].

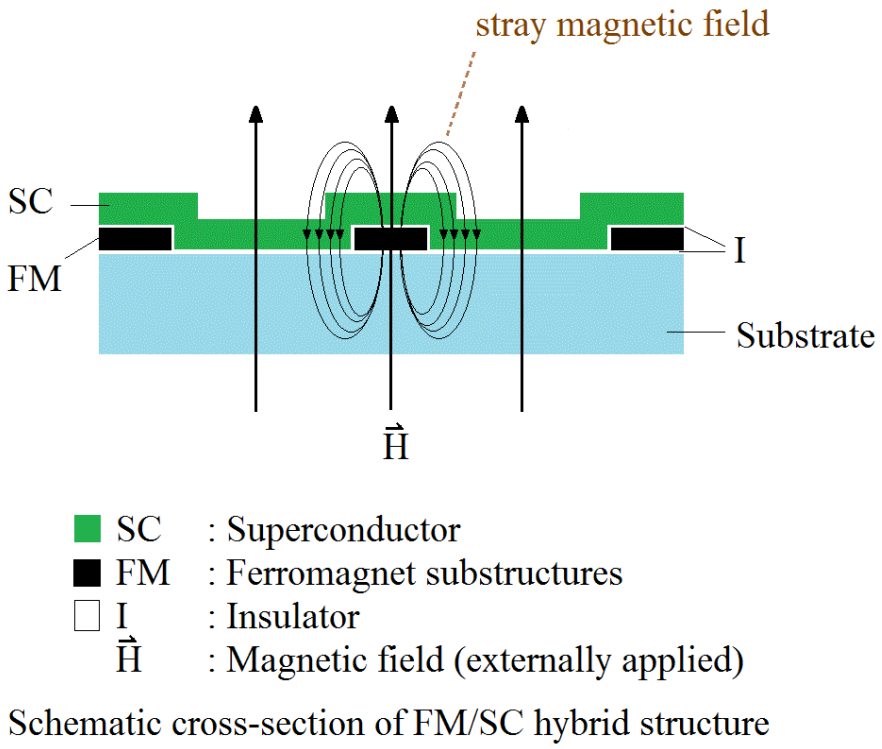

Figure 1.3: Illustration of stray magnetic field distribution in the superconductor. Due to relative high permeability of ferromagnet substructures, the externally applied magnetic field is effectively channeled through the ferromagnet pattern.

1.3.1 The Enhancement of Superconductivity Properties (H_{C2}, J_C)

In [4], superconducting properties of PbBi-films under a spatially varying magnetic field distribution by a hybrid structure of iron and brass layers have been researched by Ozmetin et al.

It was reported that externally applied homogenous magnetic field was redistributed in the superconducting film in a pattern of alternating parallel stripes with regions of low and high magnetic field. Thus, the values of second critical field (H_{C2}) and critical current density (J_C) have been much higher for current parallel to the magnetic stripes than in a control superconducting film without any field modulation. For the current perpendicular to the magnetic stripes, the superconductor behaved like an inhomogeneous resistor with regions of low and high transition temperatures (T_C) in series.

In [5], Lyuksyutov et al have reported about the vortex motion phenomenon in superconductors. It has been revealed that the applied magnetic field channels through the ferromagnetic stripes, and thus a periodically varying magnetic field distribution is obtained. It is similar to a simple sinusoidal modulation with a period of the width of magnetic stripes.

It was also reported that the stray fields of the magnetic patterns can suppress superconductivity and form channels for vortex flow. In the high field regions superconductor is either weakened or destroyed, in the low field regions locally superconductivity persists. It is understood that a homogeneous magnetic field cannot pin vortices; however, an inhomogeneous external magnetic field forms barriers for vortex motion.

These results demonstrate that it is possible to strongly enhance J_C and H_{C2} by simple redirection of magnetic flux with a soft magnetic microstructure.

Also, manipulating such channels by external magnetic fields can be used to engineer asymmetric diode-like V-I curves and superconducting switch behavior [23].

1.3.2 The Directional Current Flow Dependence

When the magnet-superconductor hybrid is placed in a constant homogeneous magnetic field (*H*), the field is amplified and redistributed over the superconducting film due to high permeability of underlying magnetic substructures. This leads to the formation of alternating regions of low and high magnetic fields. In the regions of the superconducting film directly above the magnetic substructures, the local magnetic field can be high enough to exceed the second critical field (H_{C2}). As a result, superconductivity in this portion of the film is suppressed. On the other hand, the local magnetic field in regions above the non-magnetic portions is still well below H_{C2}. Therefore, this portion of the film remains superconducting. For any current flowing in the superconducting layer, there could be two possible configurations depending on the relative orientation between the ferromagnetic stripes and the current flow direction as illustrated in Figure 1.4 [1].

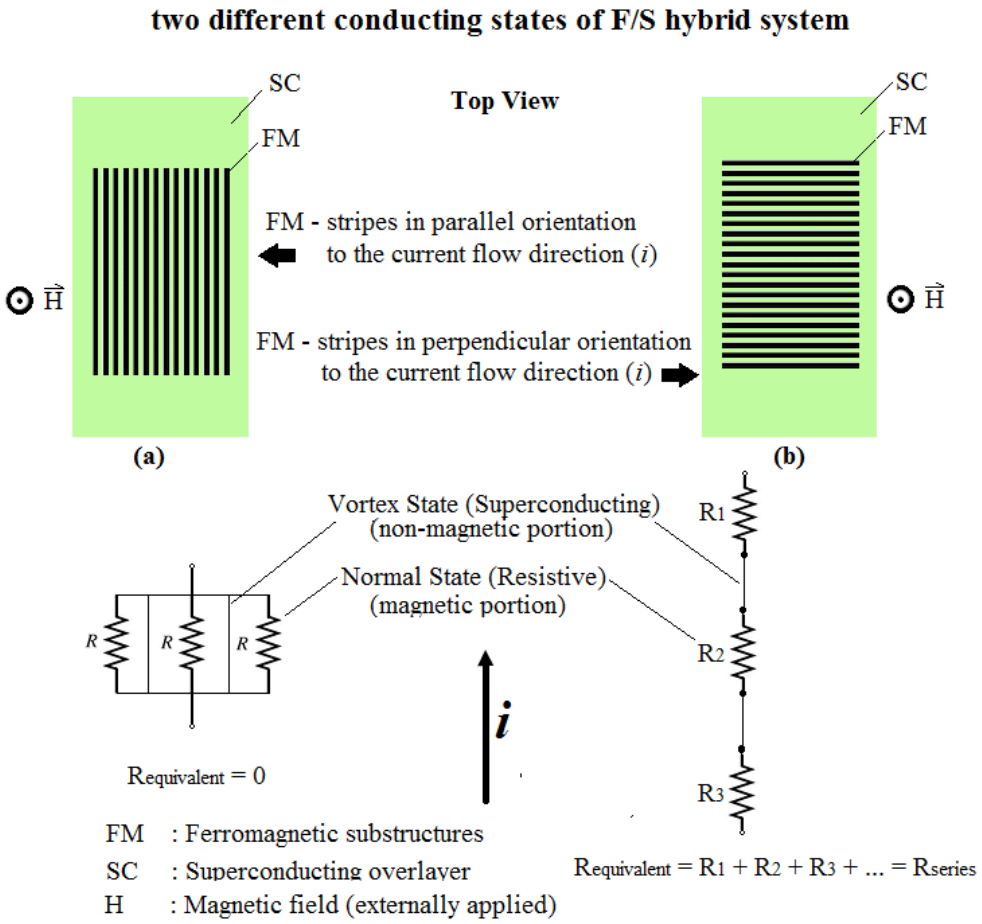

Figure 1.4: Two conducting states of F/S hybrid system dependent on the current flow direction with respect to the orientation of underlying magnetic stripes.

In the case of current flowing parallel to the magnetic stripes, the flow path is made up of a grating consisting of intermittent superconducting and resistive ribbons, and the current flows over the superconducting ribbons. In the case of current flowing perpendicular to the magnetic stripes, the path is made up of a series connection of superconducting and resistive ribbons, thus the current experiences an overall resistance and a voltage drop is generated between voltage leads.

Therefore, this directional current flow dependence naturally forms both normal and persistent conducting states. By changing the direction of the current flow relative to the orientation of the magnetic stripes, the F/S hybrid can be switched between normal and persistent conducting states. This could be achieved by rotating the underlying ferromagnetic stripes 90° with respect to the superconducting film [23, 24].

1.4 SCOPE OF DISSERTATION

We investigated the mutual interactions between neighboring ferromagnetic and superconducting thin films, the so-called ferromagnetic/superconducting (F/S) hybrids [25].

A typical F/S hybrid architecture has been proposed such that parts of the superconducting film (S-bridge) over the non-magnetic portions stay in superconducting state, while parts over the magnetic portions stay in normal resistive state. In order for achieving such a spatial magnetic/nonmagnetic modulation above the S-bridge, magnetic thin-films were grown in a pattern with an array of parallel and equally-spaced alternating stripes of magnetically soft permalloy (Py) material. The high and low amplitude periodic field distribution in the surface of the S-bridge (PbBi) is expected to regulate exclusive superconducting properties depending on the orientation of the underlying magnetic stripe edges along or across the S-bridge. So, we aimed to reveal numerical facts and directional current flow dependency of superconducting properties.

We used sputter & thermal combined physical vapor deposition (PVD) techniques together with alternative topographical micro-patterning processes. Since the most challenging task is to grow magnetic substructures in micron scale, and to properly anneal the samples for transforming into ferromagnetic microstructure, we mainly focused on this most critical part of the complete fabrication sequence.

Several topographical micro-patterning processes were experimented, and reported below:

- Preliminary mechanical lithography process (with shadow-masks): Our first attempt was to use G400P coded grid-stamps as shadow-masks to obtain magnetic Py-stripes simply all in one-step process during sputter-deposition. The chapters involving fabrication and characterization efforts in this dissertation were mainly based on this micro-fabrication process.
- Optical lithography process (with photo-mask): This micro-patterning technique provides more precise and higher quality patterns in micron scale. However, lateral patterning of magnetic films by means of optical lithography requires a number of micro-fabrication steps, and it is quite complicated due to the reactive nature of the constituent materials. We experienced this micro-patterning technique by transferring stripe patterns to the photoresist layer through a printed acetate film, which is a simple and low-cost solution. Several scanning electron micrographs of lithographically patterned samples were included in Chapter 3.
- Direct femtosecond laser assisted lithography process (without any mask): Continuously-grown magnetic Py-films were selectively etched by femtosecond laser irradiation. An experiment was conducted to investigate on this precision micro-patterning technique, and was briefly reported in Chapter 3.

Having completed the micro-fabrication of magnetic Py-stripes, superconducting PbBi-films were grown by thermal evaporation followed by quench-condensation onto the Si-substrates cooled to 77 K. In the so-called rapid solidification process, PbBi-films were formed by condensing atoms from vapor phase and quenching them onto a cold substrate. As a final phase of the complete fabrication sequence, thin electrical contact pads were grown by thermal evaporation of pure silver pieces on top of superconducting films through a steel shadow-mask. In order to reveal the directional current flow dependency of superconductivity properties with respect to the orientation of underlying magnetic Py-stripes, a standard four-point probe transport measurement technique was utilized to collect I-V data from the F/S hybrid samples under various applied magnetic fields from zero to 7 kOe and at temperatures in the range of 3-10 K.

An experimental study on the fabrication and characterization of superconducting MgB_2 thin-films was also conducted, and briefly reported in Chapter 5.

CHAPTER 2

THIN-FILMS FABRICATION

2.1 INTRODUCTION TO THIN-FILMS LABORATORY

The thin-films fabrication laboratory at Melikşah University has been equipped with the fabrication system, equipment and materials listed in Table 2.1.

Table 2.1: Fabrication equipment and materials at the Thin-Films Lab of Melikşah Uni.

The Equipment and Tools
Physical Vapor Deposition System (thermal & sputter combined PVD system)
20 lit LN_2 Dewar IC20D and withdrawal device
Vacuum annealing furnace (home-made), Hand soldering iron kit
Digital ceramic heating plate (550 °C), 40x optical zoom microscope, Ultrasonic cleaner
Precision balance, Digital multimeter, Precision tools (screwdrivers, sample holders)
Sputtering Targets & Sources
Permalloy/Hymu 80 ($Ni_{80}Fe_{20}$) sputtering target, 2.0" dia. x 0.125" thick
Aluminum Oxide (Al_2O_3) sputtering target, 2.0" dia. x 0.250" thick
Titanium (Ti) sputtering target, 2.0" dia. x 0.125" thick
DC and RF magnetron sputter guns (2 magnetron sputtering sources)
Evaporation Materials & Sources
Pieces of arc molten lead-bismuth alloy ($Pb_{82}Bi_{18}$), a type II superconductor
Pieces of silver wire, 1.5 mm dia., 99.99% pure for electrical contact pads
4 thermal evaporation sources, Basket heaters, ceramic crucibles, resistance heated boats
Other Materials and Consumables
Argon, Helium, Nitrogen pure gases and LN_2 liquid nitrogen
Acetone, Isopropanol alcohol, Distilled water, MICRO-90 cleaning agents and solutions
Silicon (100), single-side polished, and mechanical grade sapphire substrates
G400P TEM grid-stamps, and custom-designed steel shadow-masks
Indium (In) soldering kit 1" x 0.002" ribbon for ceramic target bonding
Indium wire, 1.0 mm diameter, 99.999% pure for wire-bonding
Lint-free cleaning wipers, scribers, razors, glassware (beakers, glass slides), toothpick,
kapton tape for high-vacuum and cryogenic applications, silver paint, 50 μm dia. copper wire

2.2 FABRICATION TECHNIQUES

Before reporting the fabrication process, a brief introduction was placed here below about the physical vapor deposition system, its basic operation principles and fabrication techniques with a guide for handling sputtering targets including target bonding, placing & removing a magnetic target, packing & storing targets applied as standard of practice.

2.2.1 Physical Vapor Deposition (PVD) System

2.2.1.1 System Configuration

Figure 2.1 introduces a thermal & sputter combined PVD system, NVTS 400, in our thin-films fabrication laboratory. This combined PVD system has been equipped with 4 thermal and 2 sputter sources (DC/RF) which enables us to realize co-evaporation or co-sputtering for fabricating multilayer hybrid films of different materials without breaking vacuum. In the stainless steel prismatic box-type deposition chamber, we could reach at a base pressure level of $\sim 1\,x\,10^{-8}\,Torr$ by a turbo molecular high-vacuuming pump.

Figure 2.1. The thermal & sputter combined PVD system, NVTS-400, at the thin-films fabrication laboratory of Melikşah University.

The PVD system has also been equipped with dual-channel thickness-rate measuring unit (QCM) with 0.1 Å/s precision, halogen lamps for chamber lighting and

baking, digital mass flow meter controlled gas inlets (Ar, N_2, O_2), and an integrated kit of sample rotation feedthrough, sample shutter and sample heaters. An LN_2 cold finger reservoir extending inside the chamber at top, and a homemade LN_2 cold trap station fitted in line with the gas supply inlet were used for trapping water vapor and any other impurity molecules during thin-film deposition process.

Figure 2.2 introduces the PVD chamber and its associated components inside. This combined deposition system has been equipped with four thermal evaporation sources, one DC magnetron sputtering source, and one RF magnetron sputtering source.

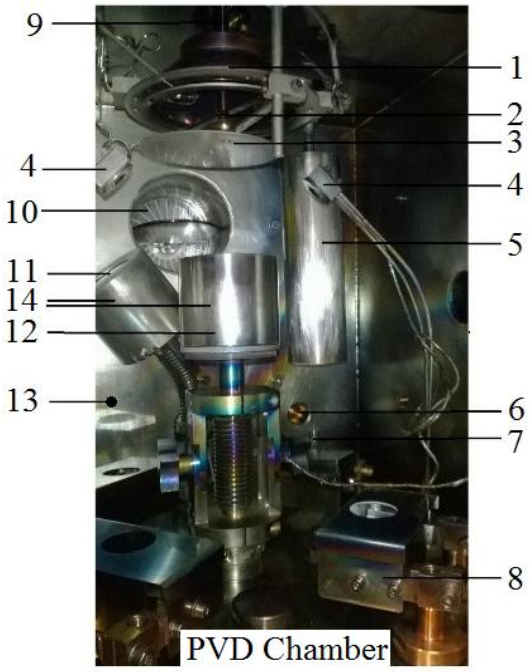

1 Substrate heater (halogen lamps)
2 Substrate holder joint/fixing rod
3 Substrate shutter
4 Quartz crystal meter (QCM) for deposition thickness measure
5 LN_2 cold finger reservoir
6 Pirana vacuum gauge
7 Halogen lamps for interior lighting and baking
8 Resistive thermal evaporation sources (4 units)
9 Rotary motion feedthrough
10 Turbomolecular vacuum pump
11 Rear - Magnetron sputter gun
12 Mid - Magnetron sputter gun
13 Stainless steel prismatic box-type vacuum chamber
14 Ground shield (anode cap)

Figure 2.2: A photograph introducing the parts and components of the PVD chamber.

One magnetron sputter gun has been fixed in the middle and the other at the rear side of the box-chamber. We allocated the middle sputter gun as thin-films sputtering source. So, the deposition distance from sputtering target to the substrate could be manually set by simply lifting up and down the outer part of the gun tail under the chamber without breaking vacuum. Thereof, we could determine and fix the deposition distance in millimeter accuracy as the deposition rate changes with the distance squared. We allocated the rear sputter gun for Ti sublimation purposes. Ti sputtering target has been positioned on the rear side of the chamber facing toward sidewall not to contaminate the film during deposition process.

We designed a homemade LN_2 cold-trap station fitted in line with the gas supply inlet of the PVD chamber in order to remove out any contaminants from the argon process gas. Figure 2.3 shows the cold-trap station with a one liter capacity LN_2 reservoir which has been utilized for argon purification purpose.

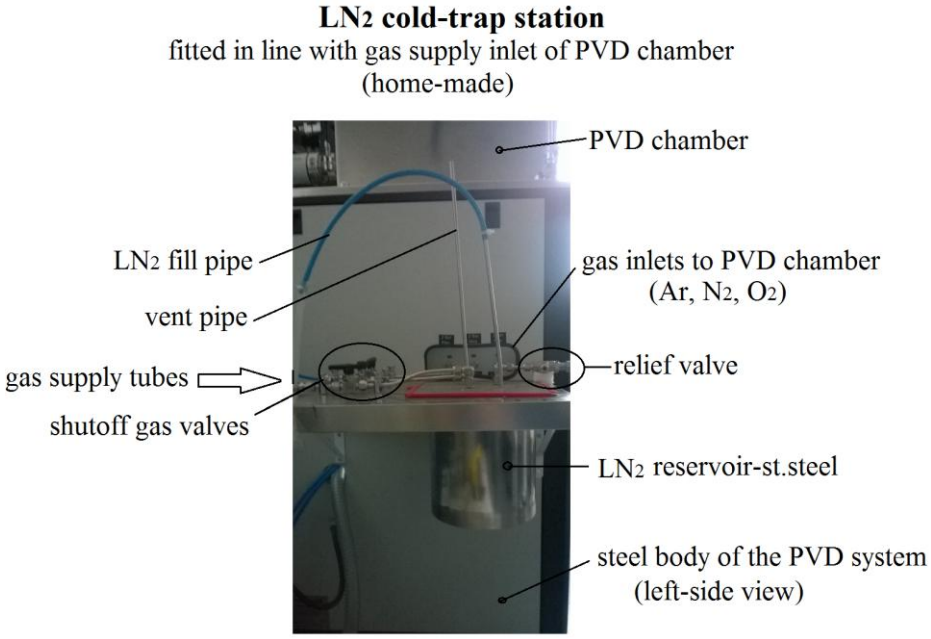

Figure 2.3: A homemade LN_2 cold-trap station fitted in line with gas supply inlet of the PVD chamber. It is utilized for purification of argon gas.

Argon process gas, which contains air and gas contaminants, is forced to pass through the LN_2 cooled trapping subsystem. A large amount of air and gas contaminants are trapped inside the steel reservoir, and thereof argon gas is further purified beyond its commercial level of 1 ppm O_2 just before introducing into the chamber. The purity of process gas has a vital importance to be able to fabricate high-quality thin-films.

2.2.1.2 Basic System Operation

(A) Cleaning the PVD Chamber

All metallic parts and inner wall surfaces of the chamber were wiped using clean lint-free tissue moistened with acetone and IPA. Vacuum gaskets and seals, and any rubber materials were only cleaned with IPA. This cleaning procedure has been applied as standard after completion of any deposition process.

Also, dependent on the usage frequency and the contamination degree of deposition chamber, we disassembled metallic, ceramic parts and fittings inside the chamber, and cleaned them in a bath of Micro-90 solution followed by rinsing with IPA, DI water, and drying with lint-free tissues. Micro-90 cleaning solution is very effective for cleaning soils including oil, grease, wax, tar, flux, particulates, hard water stains and biological debris, and for cleaning lab ware, ceramics, and stainless steel parts (2% Micro was diluted in DI water).

(B) Control of Ground Shield

Before locking and pumping-down the chamber, we measured the insulation resistance between sputtering target (cathode) and ground shield (anode cap) of the gun using a standard handheld multimeter; it shall be in the range of a few mega ohms. If it is only a few ohms, it is then understood that there may be a flake somewhere on the inside of the anode cap. If the clamping ring of cathode and anode cap have been used for a long time without cleaning, then the clearance between these two steel parts will decrease due to the collection of materials on the inside edges of the steel parts. This may cause a short of the target (cathode) with the ground shield (anode cap) when power is supplied to the sputtering gun. One of our sputtering gun head has a screw-type anode cap, while the other has a threaded-type. In case of an unbalanced positioning of the screw-type anode cap, this could also cause a short of an inside edge of the anode cap with the clamping ring of cathode. Any ground shield problem could then prevent the strike of the plasma.

(C) Pumping-Down and Pre-Conditioning of the Deposition Chamber

After final inspection of the chamber inside; sputtering targets, ground shield, substrate holder and its rotation by the rotary feedthrough, sample shutter, halogen heaters, etc., we started evacuation of the chamber. There are two types of vacuum pumps equipped with the system, mechanical pump for rough-vacuuming and turbo molecular pump for high-vacuuming. The chamber was evacuated until reaching a base pressure level of about $\sim 7\ x\ 10^{-7}\ Torr$. During evacuation process, we pre-conditioned the chamber for achieving better deposition conditions.

The pre-conditioning involves baking of the chamber using halogen lamps inside, and also heating the chamber box externally using a heat gun. Attention was paid not to expose heat against plastic joints, gasket rings of the front lid, etc. This heating process has been used in order for outgassing adsorbed molecules from inner surfaces of chamber box and surroundings, and also for desorbing and pumping out any moisture and contaminations. We also utilized LN_2 cold finger, part number-5 as introduced in Figure 2.2 above, to trap and condense any residual gas molecules and water vapor still remaining in the chamber so to reach better vacuum conditions.

(D) Striking the Plasma

When a pressure level of about $7\ x\ 10^{-7}\ Torr$ has been reached, we introduced argon process gas into the chamber with a partial pressure of about 30 mTorr. Then, we supplied power to the sputtering gun to strike the plasma at not more than 35 W. Sometimes, it could not be possible to strike a DC plasma, then in this case we first striked an RF plasma. The ability of striking the plasma is very sensitive to the clearance in between the clamping ring of cathode and the ground shield (anode cap). When not being able to strike the plasma, a number of solutions were applied:

- Mg and Ti targets were sputtered to consume the remaining oxygen in the chamber, and to facilitate striking the plasma. Magnesium powders with particle size of 44 μm were used to manufacture homemade 2" dia. Mg sputtering targets for this purpose.

- Cleaning of cathode clamping ring and the anode cap. We frequently cleaned the steel parts of cathode clamping ring and the anode cap in a diluted bath of Micro-90 solution to get rid of any deposits of sputtered materials or any flakes;
- The screw-type clamping ring was tightened unevenly. Loosening all fixing-screws, we retighten each screw evenly and smoothly;
- There might be impurities or a thin-oxide layer on the target surface which can give rise to a charge buildup preventing a DC plasma. To overcome this problem, we change cables and sputter the target for a short while using RF plasma, and then we change it back. If problem still continues after switching it back to DC, then we consider using RF sputtering;
- DC/RF power cables not fastened properly. We check the power connections;
- In case the plasma is not stable, then we try sputtering at a higher partial pressure of argon and/or power rate.

2.2.1.3 Handling Sputtering Targets

(A) Target Bonding

Before sputtering process, Al_2O_3 sputtering target was bonded onto a home-made copper backing plate to improve the heat conduction during deposition and to control ramping cycles. We used thin indium ribbon as soldering agent to bond the target and the copper backing plate, so the heat generated on the surface of the target during sputtering is transferred into the copper backing plate through this conductive thin indium interface. The copper backing plate is in contact with the water cooled gun head, so the heat is removed through the circulating cooling water. By target bonding, we also aimed to prevent Al_2O_3 ceramic target from getting cracked during sputtering process due to thermal shocks.

For bonding process we applied the following operation; a homemade copper backing plate was heated to about 150°C on our digital heating plate. Top surface of the copper backing plate was equally covered with pieces of thin indium ribbon. In a few seconds, indium completely wet the surface. Following, 2" diameter Al_2O_3 target was gently put and slightly forced onto the backing plate for a proper bonding. Finally, the bonded-backing plate was left to cool down to RT.

Indium bonding is the preferred method for bonding sputtering targets because it has the best thermal conductivity (83 W/mK) of all available bonds and is the most efficient at sinking heat away from the target. Indium metal is very soft and easily fusible with a melting point of about 156 °C.

(B) Placing the Magnetic Target

Since the magnetic interaction between the magnetron and the magnetic target is strong, it is easy for a piece of hand glove to get stuck underneath the target. To avoid this accident; first, we placed the target on its edge, then used a screwdriver to slowly lower the target down onto the copper head without using fingers.

(C) Removing the Magnetic Target

Since it is difficult to remove the magnetic target out from gun head, we always managed this task in a safe way avoiding any damage of both the magnetic target and the gun head. Sliding the magnetic target sideway, we pivoted the target up onto its edge by using a thin-blade screwdriver gently without exerting any force on the copper surface of the gun head. Then, we carefully picked up the target, and put it in its plastic bag immediately.

(D) Packing and Storing the Target

We protected reactive sputtering targets like permalloy in special plastic bags inside a vacuum desiccator to avoid moisture and dust pickup. We also used vacuum bags to store the reactive targets and samples. Extreme attention was paid during handling and storing the magnetic targets. Excessive material loss from target surface due to oxidation results in a deep circular groove deformation, and so causing early scrap of costly magnetic targets.

2.3 INTRODUCTION TO THE PROPOSED F/S HYBRID

Our principal aim is to observe the mutual interaction between ferromagnetic substructures and the neighboring superconducting overlayer, and also to reveal the directional current flow dependency of superconducting properties.

We proposed a typical F/S hybrid basically consisting of an underlying thin magnetic stripe pattern overcoated by a thin superconducting film, and electrical contact pads atop. We used permalloy (Py) and lead-bismuth alloy ($Pb_{82}Bi_{18}$) as the ferromagnet and superconductor constituents of the proposed F/S hybrids, respectively. The schematic top and cross-sectional diagrams of the multilayered F/S hybrid structure is shown in Figure 2.4.

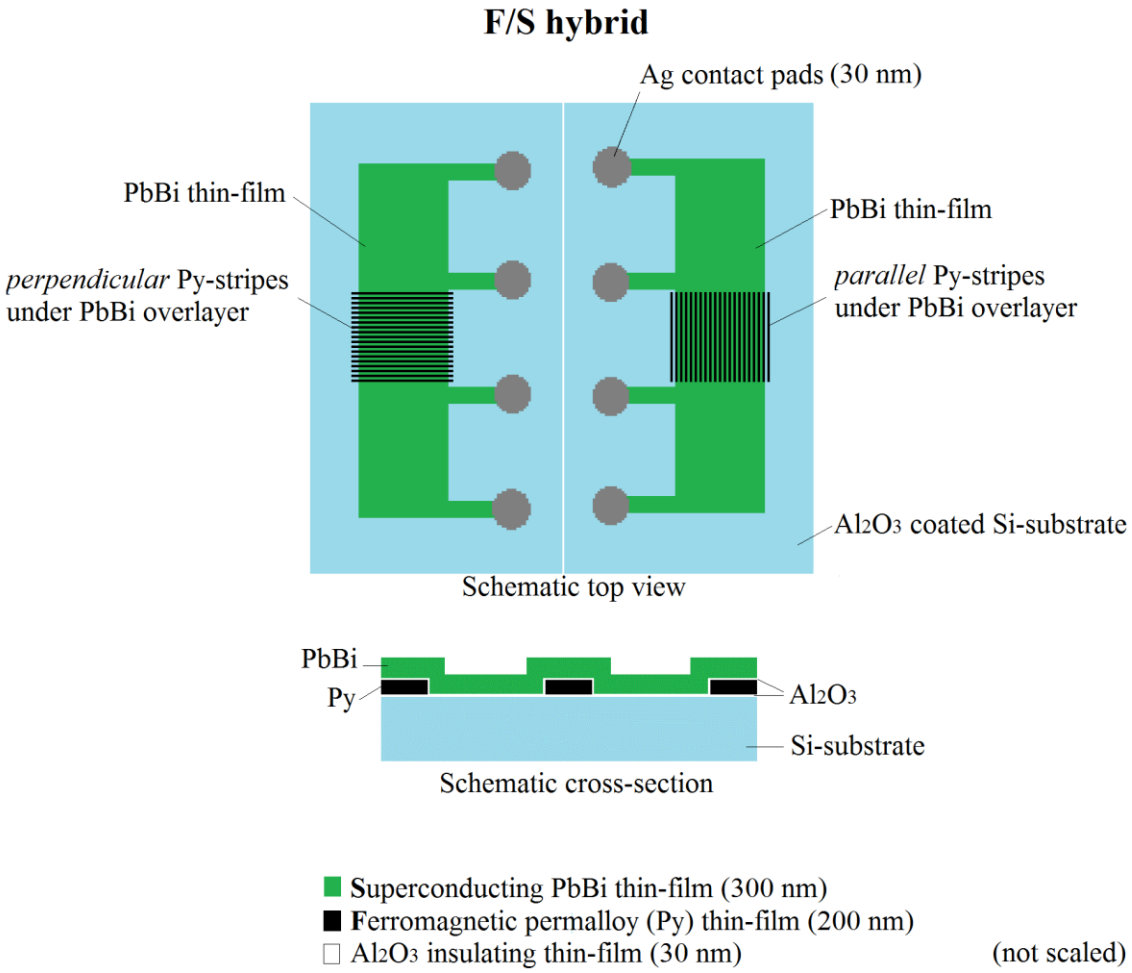

Figure 2.4: Schematic diagrams of the multilayered F/S hybrid architecture from top view and cross section. A continuous PbBi film is deposited on top of Py stripes that is supported by an Al_2O_3 coated Si-substrate (not scaled).

The F/S hybrids are composed of parallel and perpendicular Py-stripes underneath thin PbBi film (S-bridge). An array of Py-stripes has been designed parallel, while an array of Py-stripes perpendicular to each S-bridge ensuring a total spatial coverage of the segment in between voltage leads of the S-bridge. Magnetic Py and superconducting PbBi layers have been spatially separated by an ultrathin Al_2O_3 insulating interlayer to protect magnetic substructures from oxidation.

As depicted in the schematic cross-section of the F/S hybrid structure in Figure 2.4, a corrugation of PbBi overlayer at the edges of rectangular Py-stripes is expected to cause a transverse deformation in the layered structure. The effects of resulting corrugations over the superconducting properties are ignored in our research.

To realize the proposed multilayered structure, we utilized combined physical vapor deposition (PVD) techniques such as DC-RF magnetron sputtering for fabrication of Py and Al_2O_3 thin-films, and resistive-thermal evaporation for fabrication of PbBi and Ag thin-films. Thin Al_2O_3 films were grown as buffering and capping layers for electrical insulation and diffusion barrier in the layered structure. A thin-film of Ag contact pads was grown atop for 4-point electrical connections of the F/S hybrid to the sample puck.

2.4 FABRICATION PROCESS

Figure 2.5 shows the progress chart for the fabrication of a typical F/S hybrid, which is consisted of three sequential phases numbered 1, 2, and 3. This progress chart is indexed as 'Fabrication Progress Chart-1' as it has been experienced the first in our thin-films fabrication efforts.

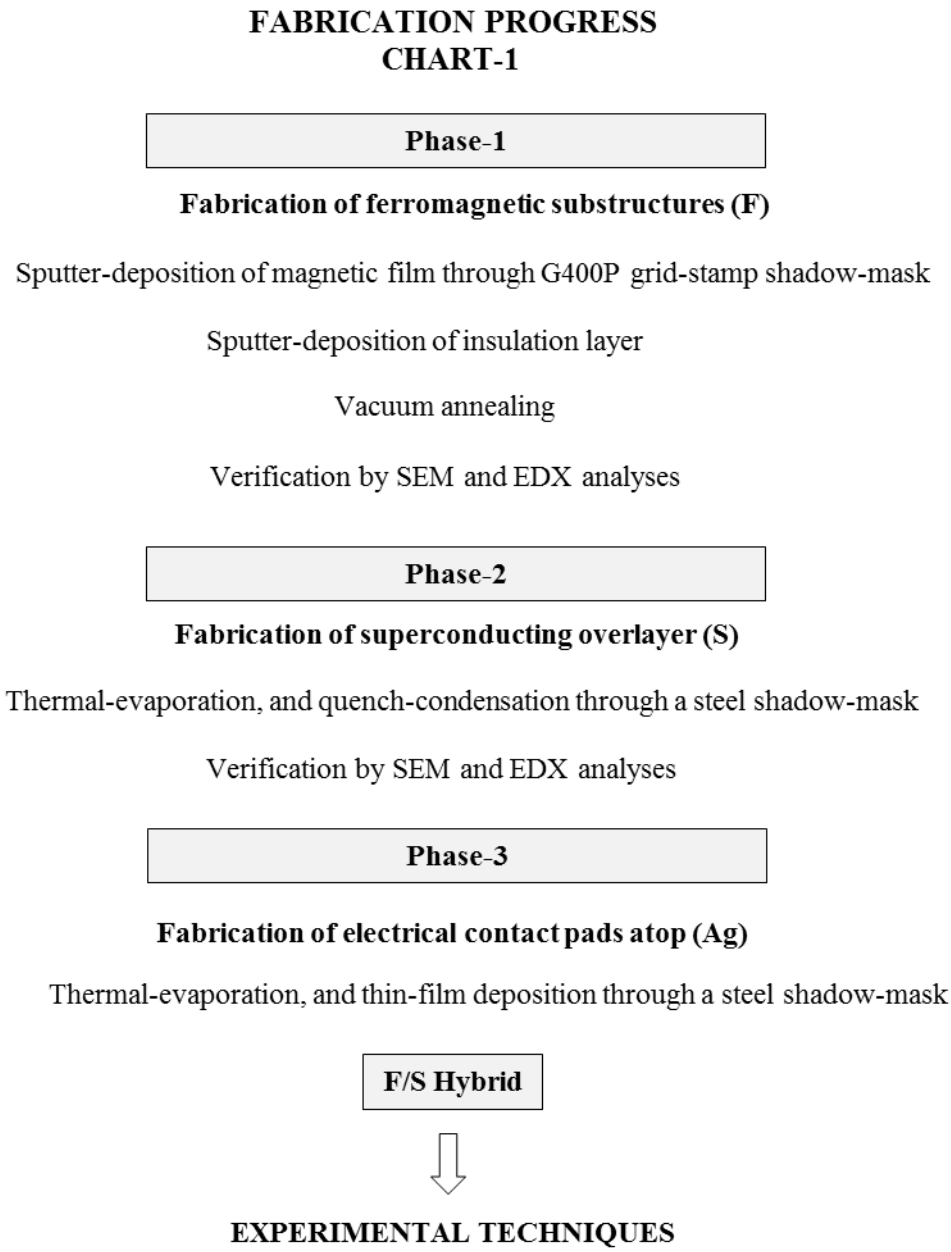

Figure 2.5: Fabrication Progress Chart-1 shows the fabrication process of a typical F/S hybrid consisting of three principal phases 1, 2, and 3 in order. This chart has been realized successfully, and the transport measurements were reported in Chapter-4.

Each phase has been subtitled as per below;

- **Phase-1**: Fabrication of ferromagnetic substructures (F)
- **Phase-2**: Fabrication of superconducting overlayer (S)
- **Phase-3**: Fabrication of electrical contact pads atop (Ag)

Each phase was reported in the following pages. The most challenging phase to manage was Phase-1, topographic patterning of permalloy (Py) films in micron scale. We experienced this micro patterning step in three different methods using different masking tools and techniques. We introduced all three methods herein, but the largest part in this dissertation was allocated for the growth of magnetic stripes through G400P grid-stamp shadow-mask.

The currently progressing photolithography and femtosecond laser assisted micro patterning techniques were also investigated and reported in Chapter 3 under the title of Alternative Fabrication Techniques for F/S Hybrid Systems.

Before starting up the fabrication process;

(a) All metallic parts and inner wall surfaces of the chamber were wiped using a clean lint-free tissue moistened with acetone or IPA. Vacuum gaskets and seals, and any plastics were only cleaned with IPA and a piece of dry lint-free tissue. Any tools, apparatus, fixing bolts, nuts, substrate holder, and what else used during the fabrication steps were all cleaned before vacuuming and vapor-deposition. We applied a standard cleaning procedure for the PVD chamber as introduced in clause 2.2.1.2 (A) above.

(b) Silicon substrates were cleaned in a bath of acetone and ethanol under ultrasonic agitation for 5 min each, rinsed with DI water, and finally dried with blowing nitrogen so to remove any contaminants such as atmospheric dust, lint from wipers, bacteria, solvent residue, water residue, oil, moisture, etc. from the silicon wafer surface.

2.4.1 Phase-1

2.4.1.1 Fabrication of Magnetic Substructures

In Phase-1, the proposed F/S hybrid requires ferromagnetic stripes that may be easily produced using a low-cost and practical topographic micro patterning method. We firstly experienced a preliminary patterning method in which a one-process step has been simply performed using commercial TEM grid-stamps as shadow-masks.

Figure 2.6 shows commercial G400P coded TEM grid-stamps used as shadow-masks for the fabrication of magnetic substructures. We preferred not to start up with lengthy and costly micro fabrication processes like photolithography in the very beginning. Being a one-process micro fabrication step, this method has proved to be a low-cost and a relatively simple way of obtaining regular arrays of magnetic stripes in micron scale.

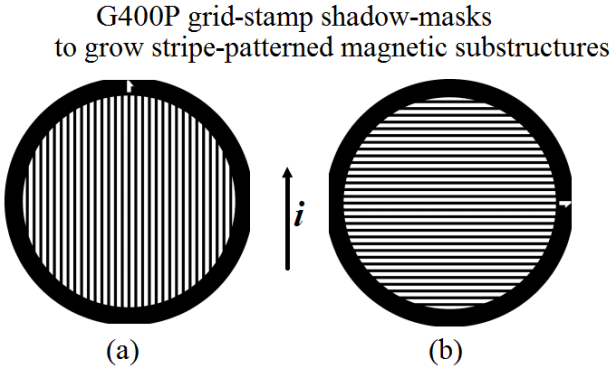

(a) parallel orientation to the current flow direction (***i***)
(b) perpendicular orientation to the current flow direction (***i***)

Figure 2.6: G400P grid-stamp shadow-masks to grow stripe-patterned magnetic substructures. (a) Parallel orientation to the current flow direction (*i*), and (b) Perpendicular orientation to the current flow direction (*i*).

A G400P grid-stamp is a 3.05 mm diameter and 18 μm thick copper mesh, and made of alternating parallel bars in dimensions of bar width=40 μm, hole=22 μm, and pitch=62 μm. Magnetic substructures were topographically grown in a stripe-pattern through 22 μm wide holes of this grid-stamp. Because thin copper stamp is too sensitive to any permanent deformation, we carefully handled it with the aid of a fine tip tweezers.

Figure 2.7 shows the steel shadow-mask which has been used for the growth of superconducting films. Although we used this steel shadow-mask in the subsequent Phase-2, we also used this mask during growth of magnetic stripes in Phase-1.

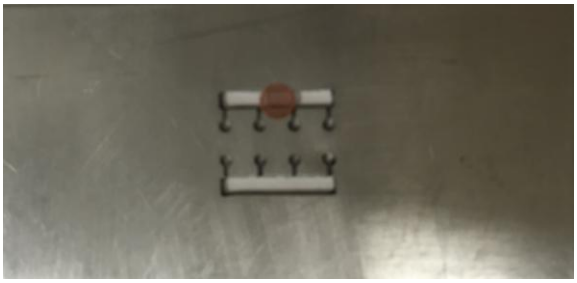

Figure 2.7: Steel shadow-mask used for the growth of superconducting film. It is also used as a supporting template for grid-stamps to grow magnetic substructures.

We positioned and fixed each grid-stamp over the segment in the center of S-bridge in between two voltage leads. To ensure a full and proper coverage of the grid-stamp over the segment, we performed all operations carefully under optical microscope view.

One grid-stamp was oriented and fixed transverse to the S-bridge for the growth of perpendicular Py-stripes, and the other stamp was oriented and fixed along the S-bridge for the growth of parallel Py-stripes so to fabricate two F/S hybrid samples under equivalent deposition conditions.

We used pieces of Kapton tape to fix the grid-stamps and Si-substrates on the steel shadow-mask. All through-openings outlying the grid-stamp was also closed using pieces of kapton tape. Following, Si-substrates were properly positioned and fixed on the steel shadow-mask. The finally obtained triple of Si-substrates/grid-stamps/steel shadow-mask arrangement has been precisely positioned and fixed on the substrate holder using clamps. The rigidity of the final arrangement was ensured.

After a close inspection over the final arrangement under optical microscope view, the substrate holder was placed onto the rotation ring of rotary motion feedthrough in the deposition chamber. To ensure the proper rotation of the substrate holder, we tested it by pressing the sample rotation switch on the control unit. Using this simple but delicate fabrication setup, we managed to grow two F/S hybrid samples simultaneously one with parallel and one with perpendicular magnetic stripes under

identical deposition conditions. Before starting up vapor deposition process, the chamber was flushed with argon gas couple of times to purge the chamber from any impurity gases, and subsequently the base pressure was brought to $\sim 7\ x\ 10^{-7}\ Torr$.

Before introducing into the chamber, argon gas was forced to pass through a liquid-nitrogen (LN_2) cold trap station in order to further purify beyond its reported commercial level of 1 ppm O_2. Meanwhile, liquid-nitrogen was also charged into the cold-finger reservoir to trap and confine water vapor and other impurities inside the chamber. During sputtering process, partial pressure of argon gas was maintained at around $\sim 4\ x\ 10^{-3}\ Torr$.

Our PVD system has been equipped with dual magnetron sputtering system allowing us for simultaneous DC and RF power sputtering. We used a 2" diameter and 0.125" thick permalloy target as sputtering source, which was fixed onto the mid gun and positioned at a distance of 10 cm to the substrate. A 2" diameter and 0.125" thick Ti sputtering target was used as sublimation source on the rear gun.

The rear gun with Ti target was turned aside towards chamber wall. Ti was sublimated in order to trap any oxygen impurities inside the chamber. By means of Ti sublimation process, the inner chamber walls are also coated with a thin Ti film so acting as a getter surface to trap oxygen during deposition process. The oxygen contamination of the film was one of the most challenging tasks to overcome in our fabrication process.

As permalloy is very sensitive to oxidation, a thin oxide layer is formed on the surface of the target when not in use. To efficiently remove out this oxide layer from the surface of target, it was pre-sputtered for 5-10 min with Ar flow at a rate of 100-125 sccm. During Ti sublimation and permalloy pre-sputtering, substrate shutter was kept closed avoiding any contamination on Si-substrate. Having completed the start-up procedures prior to film growth, we reduced the rate of argon flow rate down to 20 sccm, and manually adjusted the striking voltage of glow-discharge at a preset discharge current rate of about 112 mA. We succeeded fine adjustment by gently turning the voltage-knob on the power unit. We watched the glow-discharge through the UV-protected observation window, and we also checked the power monitor of the control

unit. Figure 2.8 shows a schematic diagram of permalloy film deposition through G400P grid-stamp shadow-mask.

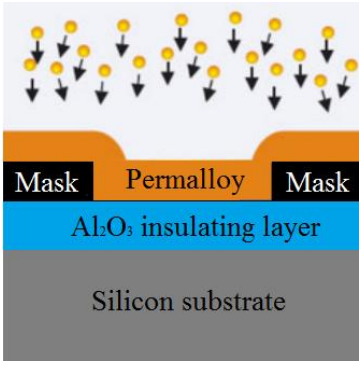

Figure 2.8: Schematic cross-section diagram of permalloy (Py) thin-film deposition through G400P grid-stamp shadow-mask (not scaled).

Once a self-sustaining plasma with a stable discharge current was maintained, then we fixed the voltage. The continuity and stability of glow-discharge were continuously monitored through the whole deposition. In case of any breakdown of glow-discharge or any current ripple, we immediately stepped in and took the control of process again. Under these fabrication conditions, film growth was continued at a fixed deposition rate of 1.0 Å/s until 2000 Å was read on the QCM thickness monitor. The DC power density was calculated about 1.75 W/cm^2 during sputtering permalloy target. The deposition rate, magnetron power ratings, argon partial pressure and flow rate, and all other control parameters were continuously tracked, controlled, and recorded during the whole deposition process. Table 2.2 shows an example track record noted during a permalloy film deposition process.

Table 2.2: An example track record of permalloy thin-film deposition process.

Permalloy film growth by DC Magnetron Sputtering process

time	Deposition Rate (Å/s)	Film Thickness (nm)	Chamber Pressure (Torr)	DC Sputter			Ar flow (sccm)
				I (Amp)	V (Volts)	Power (VA)	
5' pre-sputtering done		shutter closed	7,00E-03	0,070	310	21,7	125
0'	0,3	0	6,67E-03	0,045	336	15,12	20
12'10"	0,5	31	6,71E-03	0,063	336	21,17	20
22'10"	1,0	78	6,70E-03	0,112	317	35,5	20
32'47"	1,0	141	6,72E-03	0,112	336	35,5	20
42'50"	1,0	200	6,71E-03	0,112	336	35,5	20

Substrate was kept at room temperature through the film growth process
Tooling ratio was set as 200% (mid gun)
Chamber was evacuated down to 2,5E-7 Torr level before charging Argon gas into the chamber

2.4.1.2 Sputter-deposition of Insulation Layer

A 30 nm thick insulation capping layer was grown over the magnetic substructures. In this process, we used a 2" diameter and 0.250" thick Al_2O_3 sputtering target. Magnetic substructures and the subsequently grown superconducting film were spatially separated by this ultrathin insulation interlayer to protect the ferromagnetic substructures against oxidation. Since Al_2O_3 ceramic target has a low thermal conductivity making it susceptible to thermal shock and fracture development, we ramped up and down the power slowly at a limited rate of ≈10 watts per minute. After completion of deposition, we cooled the chamber slowly to the RT before venting, and extreme care was taken when handling the substrate as the ultrathin ceramic film is very sensitive to get cracked resulting in poor protection of the underlying magnetic substructures.

2.4.1.3 Vacuum Annealing

The sputter-deposited magnetic Py-films were annealed under vacuum condition with partial argon atmosphere. To manage this heat-treatment process properly, we utilized a split-type vacuum-tube furnace as shown in Figure 2.9.

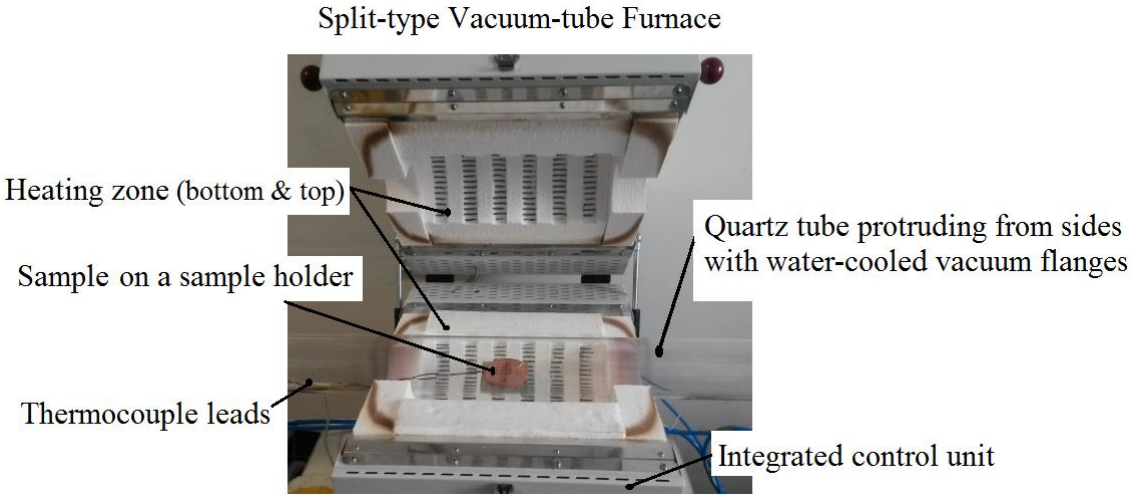

Figure 2.9: Split-type vacuum-tube furnace for heat treatments of magnetic films.

First, we experienced several trials to optimize the complete annealing cycle. After defining the necessary annealing parameters, we treated the films at 550 °C for 5 minutes. The sputter-deposited magnetic Py-films were placed on a copper disk plate, and carefully positioned inside the quartz tube. Quartz tube was vacuum-sealed with

blank flanges, and evacuated down to about 1 mTorr. The annealing cycle of samples was completed under partial argon atmosphere to avoid oxygen contamination of magnetic Py-film samples. The annealing cycle was simply controlled through a programmable user interface.

2.4.1.4 Verification of Ferromagnetic Py-films

The elemental and microstructural analyses were conducted by energy-dispersive X-ray spectroscopy (EDX) and scanning electron microscopy (SEM), respectively.

Elemental Analysis by EDX

An EDX analysis revealed an elemental composition of 82.33 at% Ni and 17.67 at% Fe exhibiting a successful growth of ferromagnetic Py-film, Figure 2.10.

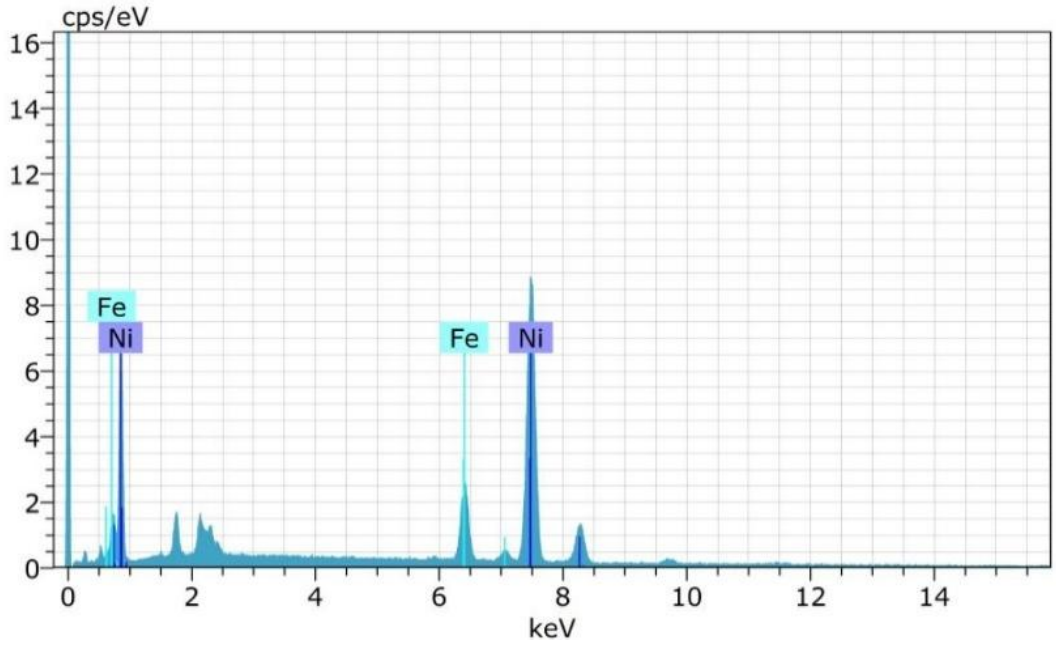

Figure 2.10: EDX analysis revealed an elemental composition of 82.33 at% Ni and 17.67 at% Fe exhibiting a successful growth of ferromagnetic Py-film.

Microstructural Analysis by SEM

Figure 2.11 shows a top-view scanning electron micrograph (SEM) of thin Py-film at 70,000x magnification. The surface topography reveals granular morphology with grains of 30 to 50 nm in diameter. Dimensions of grains shown on the micrograph are in μm.

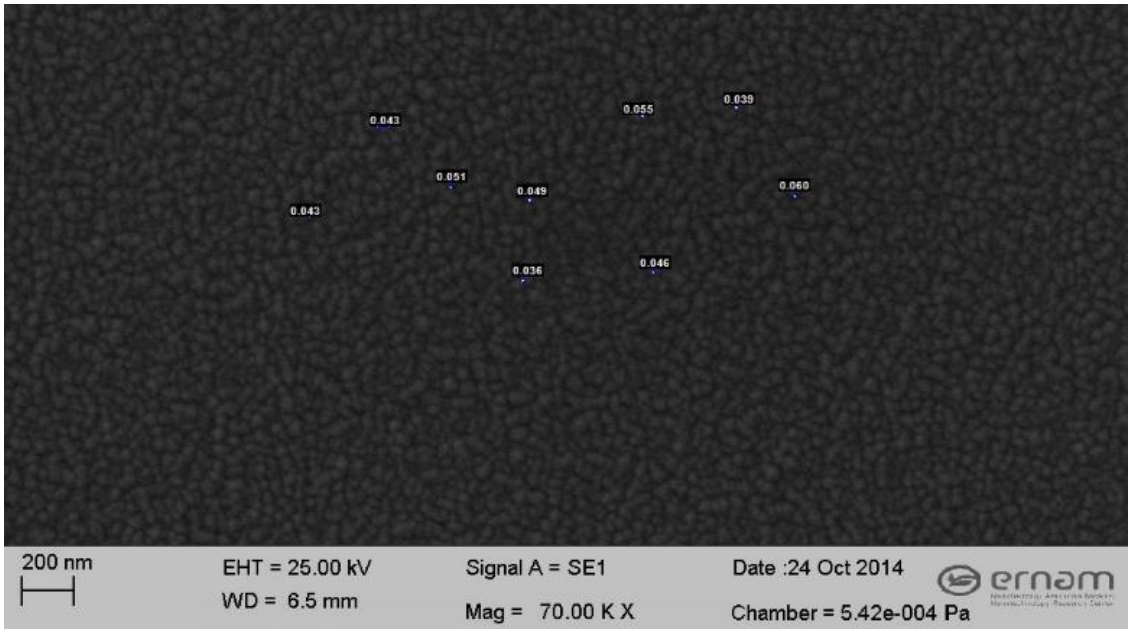

Figure 2.11: A top-view scanning electron micrograph (SEM) of Py-film at 70,000x magnification. The surface topography reveals granular morphology with grains of 30 to 50 nm in diameter (dimensions shown are in μm).

2.4.2 Phase-2

2.4.2.1 Fabrication of Superconducting Overlayer

We used bulk pieces of lead-bismuth alloy which had already been prepared by arc melting the precursors with compositions of 82 at% lead and 18 at% bismuth. We fabricated three samples simultaneously under equivalent deposition conditions; one F/S hybrid sample with perpendicular Py-stripes, one F/S hybrid sample with parallel Py-stripes, and one bare control sample of PbBi without Py-stripes. Thin PbBi-films (S-bridges) were grown by thermal-evaporation and quench-condensation growth-mechanism onto the Si-substrates cooled to about 77 K through a steel shadow-mask.

Figure 2.12 introduces the steel shadow-mask which was designed and used for the growth process of superconducting films, or the so-called S-bridges. It has a

through-opening in the shape of 10 mm long and 1.5 mm wide rectangular, which was cut on a piece of 0.35 mm thick steel sheet by wire-erosion. Four through-holes in equal spaces were also opened for the growth of electrical contact pads. The body of S-bridge and contact pads are connected through 0.25 mm wide channel openings.

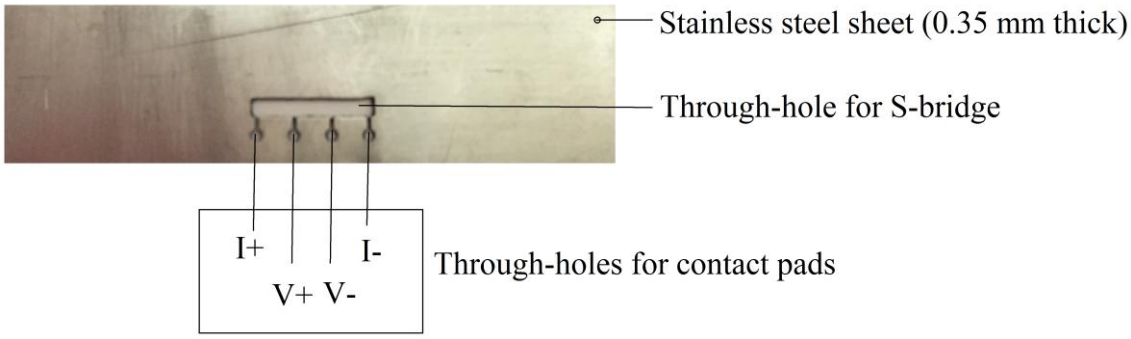

Figure 2.12: Introduction of steel shadow-mask which has been designed and used for the growth of superconducting films, or the-so-called S-bridges.

A few grams of PbBi alloy was placed in a ceramic crucible. Si-substrates with and without Py-stripes were positioned properly and fixed onto the steel shadow-masks using pieces of kapton tape. The steel shadow-masks were sticked in contact with bottom of the stainless steel cold-finger reservoir by applying a thin-layer of vacuum grease. Figure 2.13 shows a photo of the PbBi-film fabrication setup inside the chamber just before enclosing the PbBi deposition zone for spatial isolation.

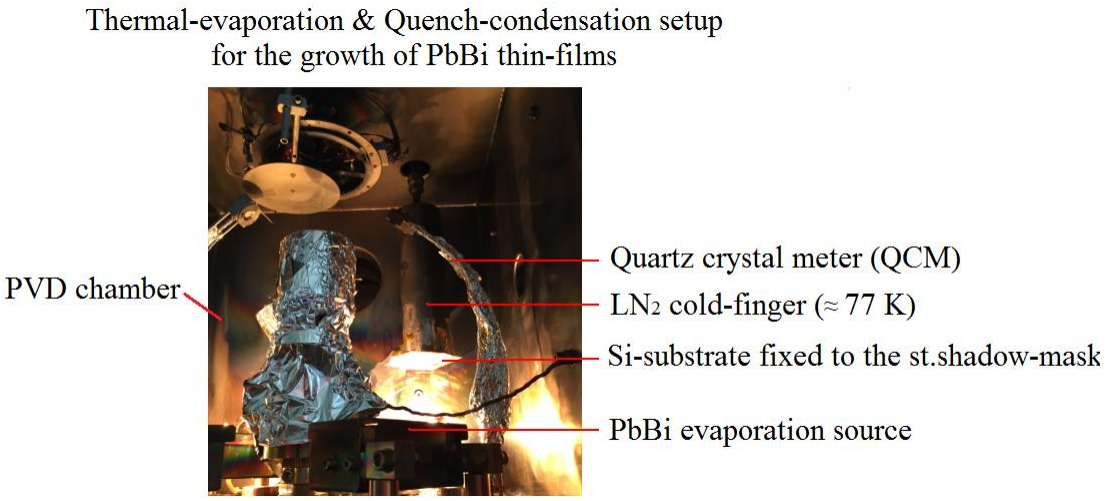

Figure 2.13: A photo from the inside of the PVD chamber. PbBi-films were grown by thermal-evaporation followed by quench-condensation mechanism. The PbBi deposition zone surrounding the PbBi evaporation source, samples, cold-finger reservoir and quartz crystal (right) was spatially isolated from the rest of chamber.

Since PbBi vapor severely contaminates all surroundings in the chamber, the PbBi deposition zone surrounding the PbBi evaporation source, samples, cold-finger and the quartz crystal (right) was spatially isolated from the rest of the chamber. We used aluminum foil and thin-brass sheet materials to build up this enclosure.

After the above preparatory works, we locked and evacuated the chamber until reaching a base pressure level of $\sim 9.5\ x\ 10^{-7}\ Torr$. As pumping down the chamber, we carefully and slightly heated the walls of chamber box with a hot air blow-off using a heat gun. Also, halogen lamps inside the chamber were used to help outgassing the adsorbed impurity gasses from inner surfaces of the chamber. When reaching at $\sim 1\ x\ 10^{-6}\ Torr$, we also continuously charged LN_2 into the colder finger reservoir to trap water vapor and any impurities in order for better vacuum conditions.

Superconducting PbBi-films were grown by rapid-solidification process called quench-condensation. Bulk PbBi pieces were thermally-evaporated under high vacuum condition, and the resultant PbBi vapor was rapidly quench-condensed on the cryogenically-cooled Si-substrates at about 77 K. Si-substrates were subject to direct thermal contact with LN_2 cold-finger during the whole deposition. LN_2 was supplied from the StirLIN-1 Compact Nitrogen Production Plant at TAUM, Erciyes University, and safely maintained in a vacuum-insulated 20 lit Dewar at our laboratory. Thickness of PbBi-film was continuously monitored through a quartz crystal microbalance (QCM). Having reached the targeted film-thickness, we stopped the evaporation process by switching-off the power supply, and left the samples in the chamber for warming up to room temperature (RT).

Table 2.3 shows an example track record noted during a PbBi deposition process. The deposition rate, evaporation source I/V ratings, base pressure, and LN_2 level of the cold-finger reservoir were all continuously observed, controlled, tracked, and recorded during the whole deposition process.

Table 2.3: An example track record of PbBi thin-film deposition process.

PbBi film growth by thermal evaporation + quench condensation at LN2 temperature

	Deposition	Film	Chamber	Evaporation Source		
time	Rate (Å/s)	Thickness (nm)	Pressure (Torr)	I (Amp)	V (Volts)	Power (VA)
Chamber was first evacuated down to 9,5E-7 Torr level before deposition process was started						
0'	0,5	0	9,80E-07	27	2,4	64,8
6'	0,8	29	7,70E-07	24	2,0	48,0
12'	0,9	60	5,70E-07	23	1,9	43,7
24'	0,6	109	3,70E-07	23	1,9	43,7
35'	0,6	150	3,40E-07	23	1,9	43,7
		stop				

Substrate was kept at LN2 temperature through the film-growth process
Since the tooling ratio was defined half the real value,
film thickness is calculated as twice the value read on the QCM
approx. film thickness = 2 x 150nm = **300nm** (read from QCM)

Warming up to RT, we vented the chamber to atmosphere, unloaded the samples carefully, and protected the samples in sample-boxes inside a vacuum desiccator. We applied the standard cleaning procedure to make the deposition chamber ready for the next coming deposition process. As the continuity and intact of the PbBi-films are of vital importance for the transport measurements, we carefully inspected the quality of samples under optical microscope view at the end of each Phase-2 process.

2.4.2.2 Verification of Superconducting PbBi-films

The elemental and microstructural analyses were conducted by energy-dispersive X-ray spectroscopy (EDX) and scanning electron microscopy (SEM) techniques.

Elemental Analysis by EDX

An EDX analysis of PbBi-film revealed that the film was formed at elemental compositions of 78.22 at% Pb and 21.78 at% Bi, indicating the film with Bi slightly richer than the precursor as shown in Figure 2.14.

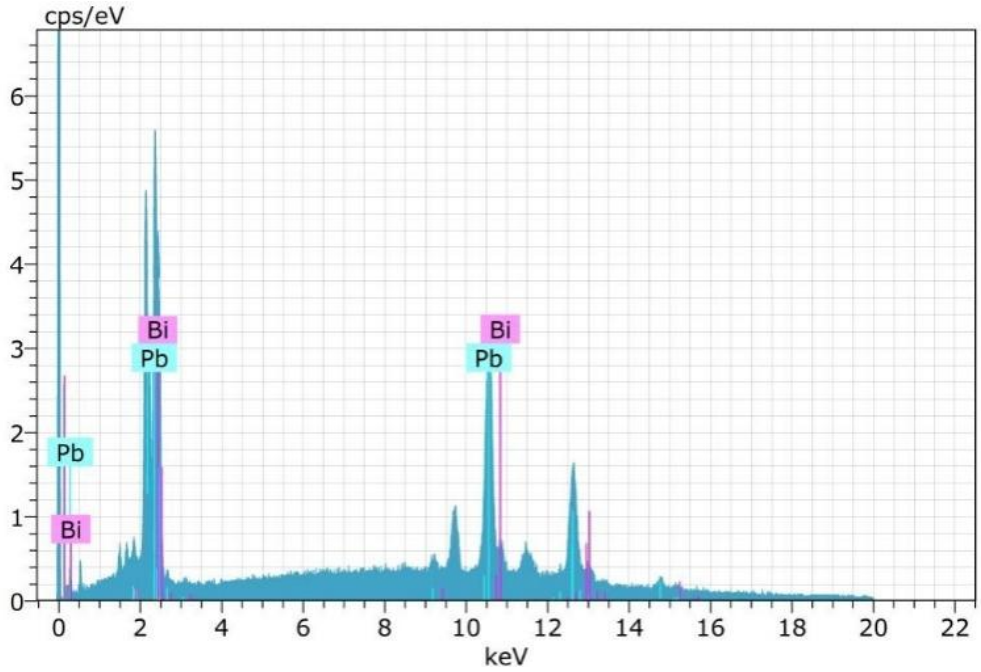

Figure 2.14: EDX analysis revealed elemental compositions of 78.22 at% Pb and 21.78 at% Bi, indicating the film with Bi slightly richer than the precursor.

Microstructural Analysis by SEM

Figure 2.15 shows a top-view scanning electron micrograph of PbBi film which was quench-condensed on Si-substrate at 77 K to obtain amorphous film structure. It is revealed that film surface topography features a granular morphology, shown in μm.

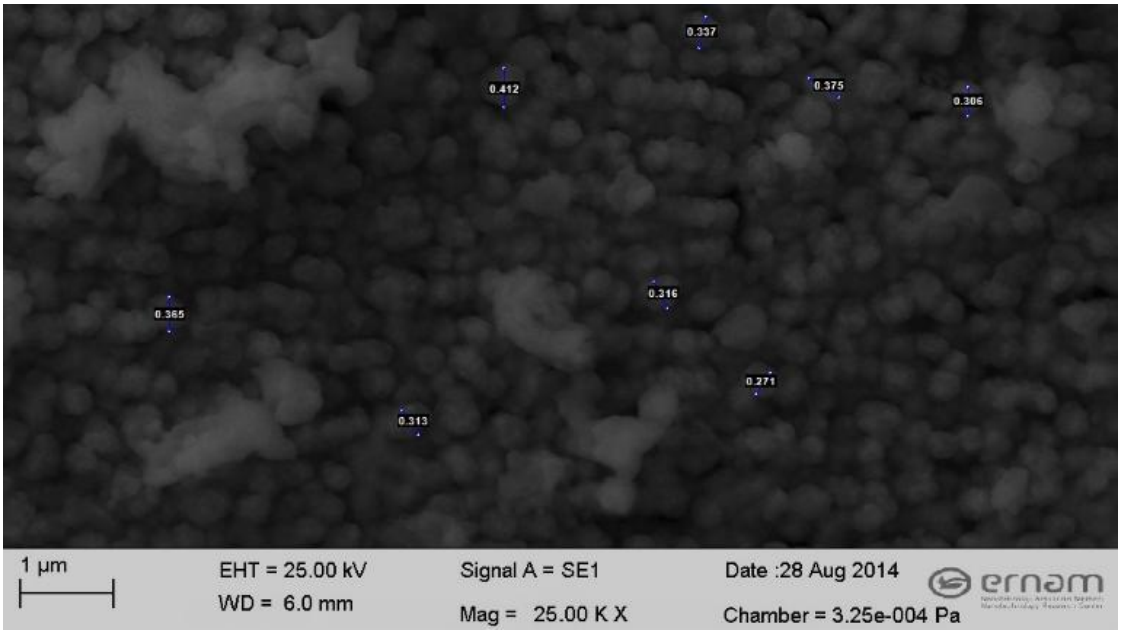

Figure 2.15: A top-view scanning electron micrograph of quench-condensed PbBi-film revealing that the surface topography features a granular morphology.

The vapor pressure of Bi is close to that of Pb, and this is the reason why Pb is alloyed with Bi to obtain a type-II superconductor.

2.4.3 Phase-3

2.4.3.1 Fabrication of Electrical Contact Pads

In Phase-3, we deposited thin silver contact pads using the steel shadow-mask, which has been introduced in the preceding Phase-2. The through-holes outlying the circular pad-holes on the steel mask were all closed with pieces of kapton tape. Thin silver pads were grown in 30 nm thickness by resistive thermal-evaporation technique.

2.4.4 F/S Hybrid

Figure 2.16 shows a photograph of the finalized F/S hybrid sample ready for 4-point probe dc transport measurements.

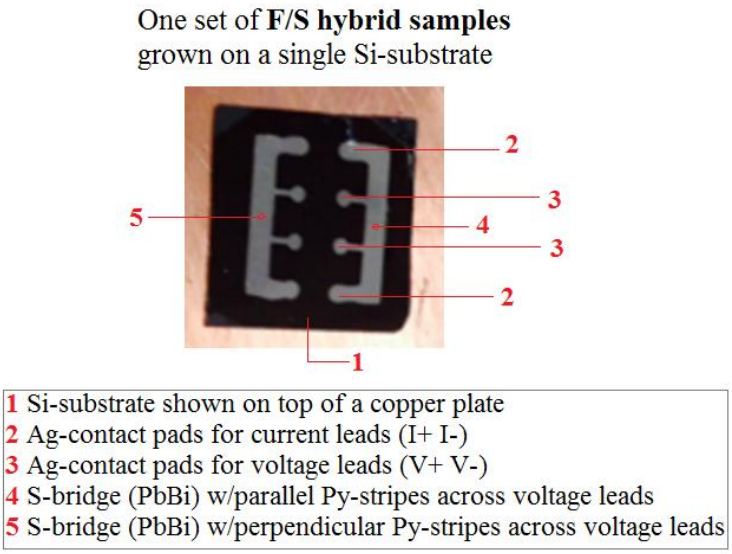

Figure 2.16: A photograph of the finalized F/S hybrid samples ready for 4-point probe transport measurements. One set of F/S hybrid samples was grown on a single Si-substrate with underlying parallel and perpendicular Py-stripes oriented across voltage leads.

We also studied on two alternative fabrication techniques for F/S hybrid systems. The currently progressing techniques, photolithography and femtosecond pulsed-laser assisted micro-patterning techniques, were experimented and reported in Chapter 3.

CHAPTER 3

ALTERNATIVE FABRICATION TECHNIQUES FOR F/S HYBRID SYSTEMS

In this chapter, we investigated and experimented alternative fabrication techniques developed with two distinct classes of micro-fabrication processes:

(1) Micro-fabrication with photolithography process, and

(2) Micro-fabrication with femtosecond-laser lithography process.

3.1 MICRO-FABRICATION WITH PHOTOLITHOGRAPHY PROCESS

The proposed F/S hybrid requires ferromagnetic stripes that may be easily realized using low-cost and scalable micro patterning techniques, such as photolithography. And also, we aimed to optimize our micro fabrication process with a much practical, faster and integrated method so to produce higher-quality and finer feature-sized magnetic substructures. With this motivation, we defined a new fabrication progress chart as introduced in Figure 3.1.

In this chapter, we reported our experimental studies on Phase-1 only of the complete fabrication sequence, and also newly designed steel shadow-masks necessary for subsequent Phase-2 and Phase-3 were introduced in detail.

FABRICATION PROGRESS
CHART-2

Phase-1

Fabrication of ferromagnetic substructures (F)

Topographic micro-patterning with Photolithoghraphy Technique
a dark field photo-mask printed on acetate film
pattern transfered onto resist-layer (resist -mask)

Sputter-deposition of magnetic film through filling in the trenches on the resist-mask

Removal of the resist-mask by lift-off process

Cleaning with IPA, DI water, and drying with N2 blow-off

Sputter-deposition of insulation layer

Vacuum annealing

Verification by SEM and EDX analyses

Phase-2

Fabrication of superconducting overlayer (S)

Thermal-evaporation, and quench-condensation through a steel shadow-mask

Verification by SEM and EDX analyses

Phase-3

Fabrication of electrical contact pads atop (Ag)

Thermal-evaporation, and thin-film deposition through a steel shadow-mask

F/S Hybrid

Figure 3.1: Fabrication process with photolithography micro-patterning technique. Fabrication Progress Chart-2 is currently under development.

The multilayer architecture of the proposed F/S hybrid consists of three major constituent layers together with insulation interlayers grown in a sequential order as shown in Figure 3.1. To manage the fabrication of this multilayer hybrid structure, we needed three masks organized in down-top design. Figure 3.2 exploits the AutoCAD drawings of these three major layers in overlapped view.

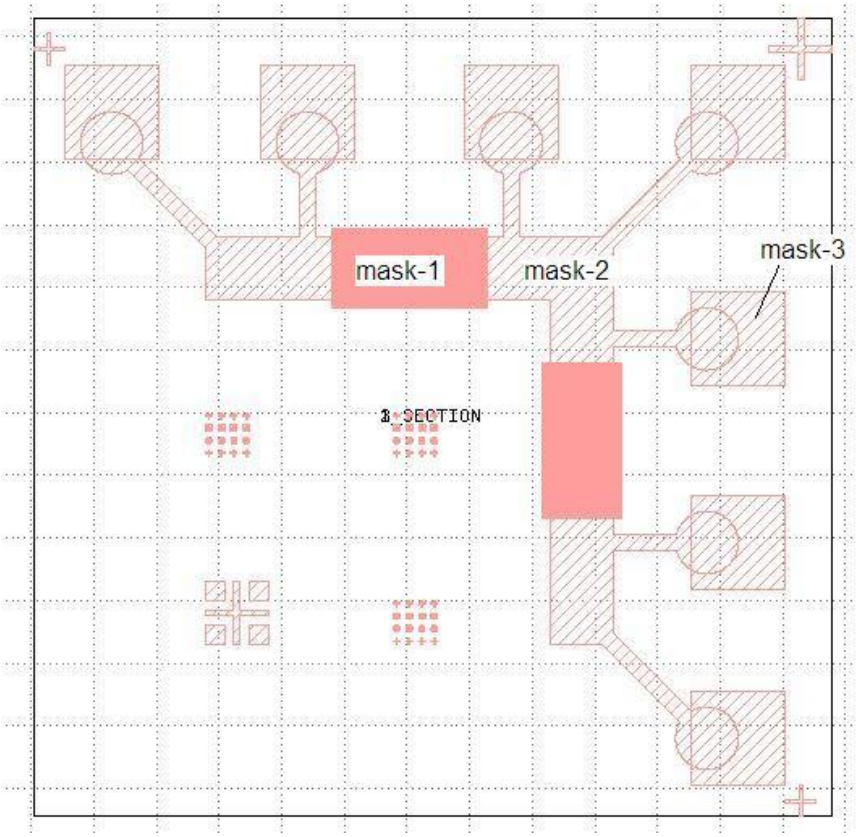

Figure 3.2: The proposed F/S hybrid design, and the masks. Drawing of one set of F/S hybrid showing three masks in overlapped view used for the fabrication of three constituent layers through a sequential growth mechanism.

We used a resist-mask made of positive tone AZ 1518 as a replication of the photo-mask printed on acetate film. Also, steel shadow-masks for the growth of superconducting and electrical contact pad layers were newly designed and produced by a high-precision micro laser cutting tool.

All these masking tools were subtitled and introduced as per below:

- Mask-1: Photo-mask printed on acetate film for growth of magnetic substructures
- Mask-2: Steel shadow-mask for growth of superconducting overlayer
- Mask-3: Steel shadow-mask for growth of electrical contact pads atop

The F/S hybrid was mainly composed of a 6500 μm long, 1000 μm wide, and 300 nm thick superconducting PbBi-film with an underlying 200 nm thick magnetic Py-stripe patterned film. Py-stripes were spatially separated by 20 μm wide gaps, and oriented either parallel or perpendicular to the current flow direction over a segment of 2500 μm long distance across voltage leads of the superconducting S-bridge, Figure 3.3.

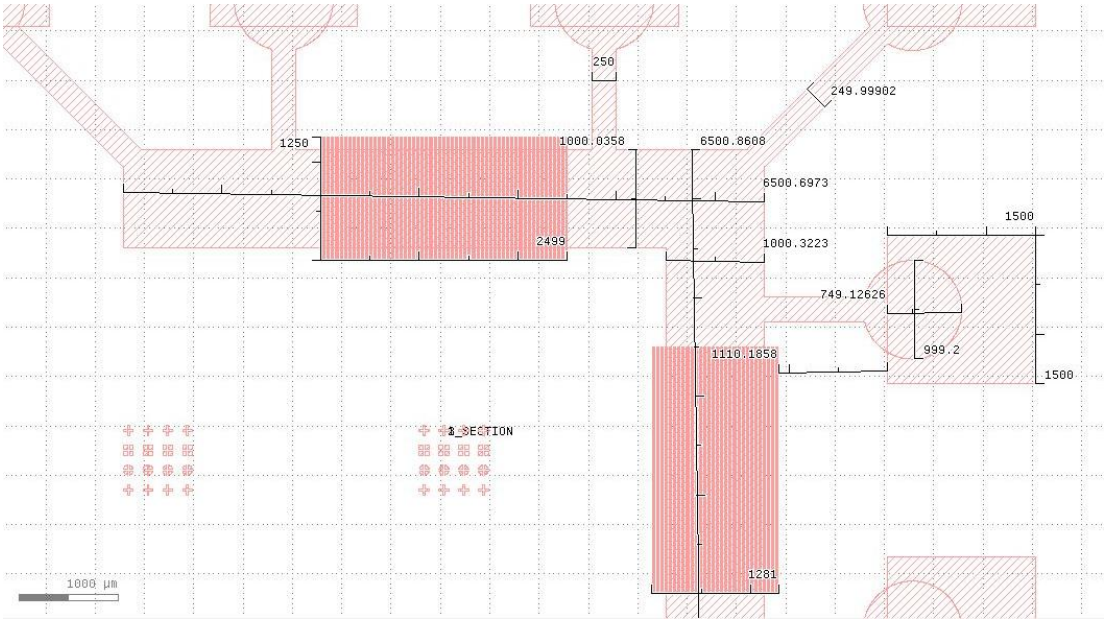

Figure 3.3: The design of the proposed F/S hybrid in µm scale. Linear arrays of magnetic substructures in a stripe-pattern with 20µm wide gaps and periodicity are oriented along and across the superconducting films (S-bridges). Square-shaped pads are designed atop as electrical contact points.

(a) Parallel Py-stripes;

Parallel Py-stripes are oriented along the superconducting film (S-bridge). The length of stripes was designed equal to the distance across voltage leads of the S-bridge, and the width of stripe-pattern was designed slightly extending the width of S-bridge with a few microns to ensure a full spatial coverage of the segment underneath the S-bridge.

(b) Perpendicular Py-stripes;

Perpendicular Py-stripes are oriented transverse to the superconducting film (S-bridge). The length of stripes crossing the S-bridge was designed slightly longer than the width of the bridge with a few microns, and the width of stripe-pattern was designed equal to the distance across voltage leads of the S-bridge. So, we ensured a full spatial coverage of the segment underneath the S-bridge.

3.1.1 Phase-1

3.1.1.1 Fabrication of Magnetic Substructures

In Phase-1, thin Py-stripes were grown in micron scale by means of photolithography technique in which a multi-step process sequence has been performed. Photolithography efforts were conducted at the Nanotechnology Research Center of Erciyes University, ERNAM. The equipment and the materials used in our lithography process are listed as per below:

Photolithography Facility at ERNAM
Equipment
Mask Aligner: MIDAS MDA-400M (5" mask, 3" substarte, vacuum contact mode)
Spin Coater: WS-650MZ-23NPP
Hot plate for soft baking
Materials
Photo-mask: 3" acetate film fixed on 5" blank quartz
Photoresist: Positive tone AZ 1518
Developer: AZ 351B
Remover AZ 100 (for lift-off)

As it is a low-cost and practical solution, we designed and printed photo-masks (Mask-1) on special silver-coated acetate films in 3600 dpi resolution at a printing house. The dark-field printed 3" size acetate film was placed and fixed onto 5" blank quartz to complete the required photo-mask arrangement. The replica of this photo-mask was then transferred onto the photoresist layer, which was coated on Si-substrate.

A series of chemical treatments enabled us to grow thin magnetic substructures on top of Si-substrate. Photolithography is an optical means for transferring patterns onto a substrate through a number of steps such as align, UV-expose, develop, and lift-off. The type of photoresist, developer, developing time and temperature are all key parameters forming the required resist pattern in well-quality.

Before starting up the photolithography process, we applied a standard cleaning procedure to remove any contaminants such as atmospheric dust, lint from wipers, bacteria, solvent residue, water residue, oil, moisture, etc. from the silicon wafer

surface. Si-substrates were cleaned with acetone and ethanol under ultrasonic agitation for 5 min each, rinsed with DI water, and finally dried with blowing dry nitrogen.

In micro-fabrication step of Phase-1, we used positive tone AZ 1518 Photoresist. In wet chemical development of positive tone photoresists, UV-exposure decomposes the development inhibitor and developer solution only dissolves photoresist in the exposed areas. Firstly, Si-wafer was held on a spinner chuck by vacuum and photoresist was spin-coated at 4000 rpm onto a 3" Si-substrate by using WS-650MZ-23NPP spin coater.

Coated photoresist was pre-baked (soft-baked) at 100 °C on a hot-plate for 50 seconds. We baked the coated resist to evaporate solvent and to densify the resist after spin-coating. Using a hot plate, temperature rise starts at bottom of wafer and works upward allowing the solvent in the resist to evaporate more easily and thoroughly. But, it is needed an extremely smooth and well-balanced surface for good thermal contact and heating the wafer uniformly.

The photo-mask was aligned with the Si-wafer for a uniform UV-exposure. A fine alignment of Si-substrate with photo-mask was succeeded by using MIDAS MDA-400M mask aligner in vacuum contact process mode. The geometric pattern on the photo-mask was optically transferred onto the photoresist layer to form 20 μm wide trenches to serve as a mold for the subsequent Py vapor deposition process.

After pattern transfer onto the resist layer, a mixture of bath solution was prepared by diluting AZ 351B Developer with deionized water. Samples were submerged in the solution for about 90 seconds, and followed by rinsing in deionized water and drying with nitrogen blow-off. Resist layer on the Si-substrate was inspected under optical microscope view to check the clearance of trench openings and the overall quality of the resist layer. In the end of photolithography process, we obtained a resist-mask, i.e. a replica of the photo-mask on the Si-substrate. The micro-patterned resist, the so-called resist-mask, consists of an array of regularly spaced, parallel, and elongated trenches.

Trench openings in the resist layer were filled-in with sputtered-Py vapor, and overall top surface of resist layer was also coated. Py-stripes were grown in 200 nm thick by magnetron sputtering technique.

After film deposition, the samples were soaked in a glass-beaker of acetone with ultrasonic agitation to lift-off the remaining resist layer. We used AZ 100 to remove the remaining resist. When the resist was stripped off the Si-substrate, Py-film deposited on the resist surface was also lifted-off, and so the Py-film on the Si-substrate was remained in the desired stripe-pattern. The standard post cleaning procedure using IPA, DI water, and drying with Nitrogen blow-off has been applied. After cleaning process, samples were checked under optical microscope view to be sure if the samples have been completely free of any resist residue on the substrate surface. In case any bit of resist residue is left, then cleaning process is repeated. Figure 3.4 shows an optical microscope image of magnetic stripes after lift-off process. The resultant pattern was consisted of periodic, equally-spaced, and alternating parallel Py-stripes.

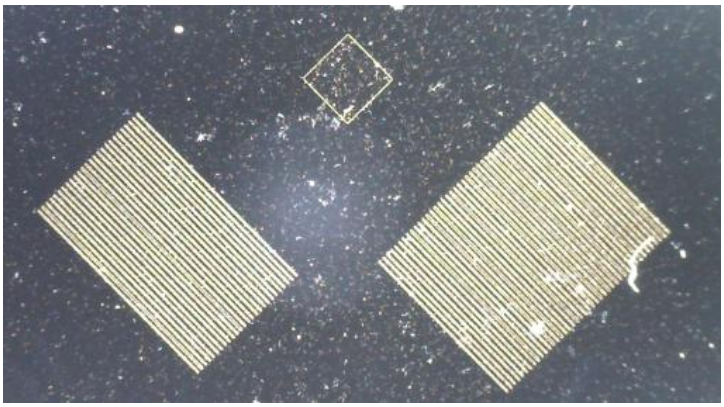

Figure 3.4: An optical microscope image of patterned-film after lift-off process. There are 2 arrays of magnetic stripes aligned in two orthogonal directions. The black-background belongs to the Si-substrate, and the parallel elongated lines are magnetic stripes. Each stripe is 20 μm wide and about 200 nm height in size. The space between adjacent stripes is 20 μm.

As a final step of Phase-1, magnetic substructures were overcoated with a 30 nm thick Al_2O_3 insulation layer by RF magnetron sputtering technique. Then, the samples were subject to a well-defined heat-treatment in a homemade vacuum annealing furnace for transforming into ferromagnetic microstructure. The annealing process was applied the same as in Phase-1 of the previously introduced Fabrication Progress Chart-1.

3.1.2 Phase-2

3.1.2.1 Fabrication of Superconducting Overlayer

Figure 3.5 shows a steel shadow-mask, the so-called Mask-2, used for fabrication of superconducting S-bridges. It was laser-cut on a piece of steel-sheet 6.5 cm square and 0.15 mm thick. Mask-2 has four sets of shadow-masks, and each set consists of two cascaded F/S hybrids, one for parallel and the other for perpendicular Py-stripes. This unique design enables us to fabricate three sets of F/S hybrid samples and one bare control sample simultaneously under identical fabrication conditions.

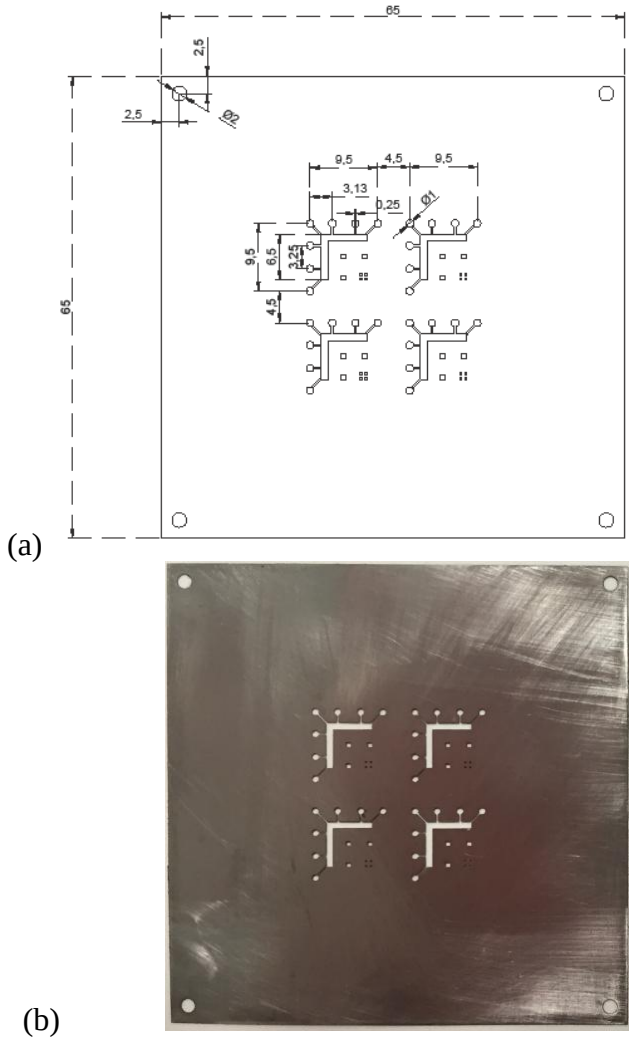

Figure 3.5: Steel shadow-mask (Mask-2) is used for fabrication of superconducting S-bridges: (a) design, and (b) laser-cut steel shadow-mask.

The fabrication sequence from this stage forward has been applied the same as in Phase-2 of the previously introduced Fabrication Progress Chart-1.

3.1.3 Phase-3

3.1.3.1 Fabrication of Electrical Contact Pads

Figure 3.6 shows a steel shadow-mask, the so-called Mask-3, used for fabrication of electrical contact pads. It was laser-cut on a piece of steel-sheet 6.5 cm square and 0.15 mm thick. Mask-3 has four sets of shadow-masks, and each set consists of two cascaded F/S hybrids, one for parallel and the other for perpendicular Py-stripes. This unique design enables us to fabricate three sets of F/S hybrid samples and one bare control sample simultaneously under identical fabrication conditions.

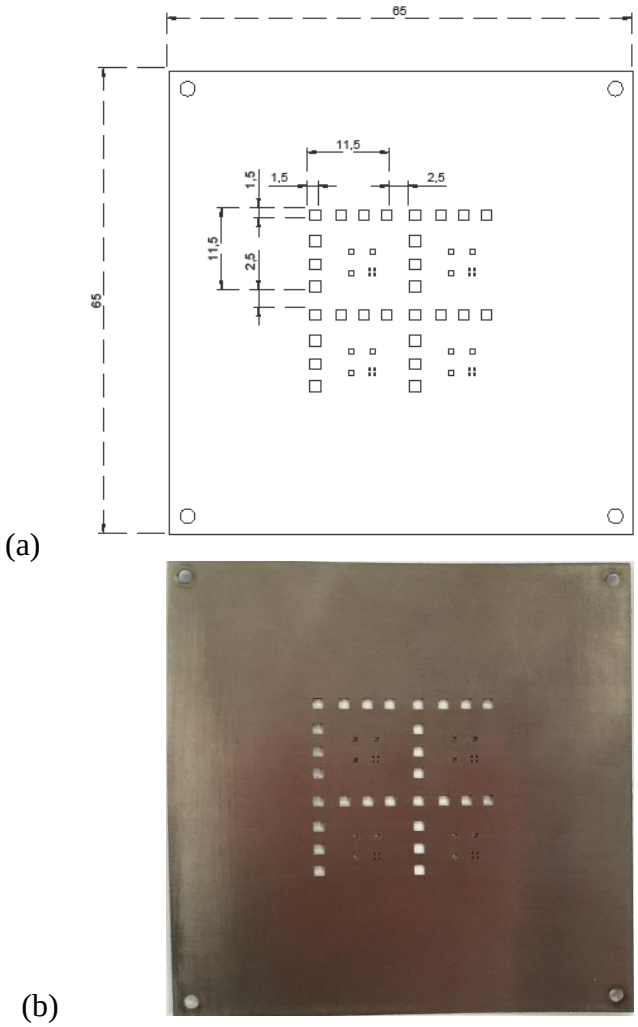

Figure 3.6: Steel shadow-mask (Mask-3) is used for fabrication of electrical contact pads: (a) design, and (b) laser-cut steel shadow-mask.

The fabrication sequence from this stage forward has been applied the same as in Phase-3 of the previously introduced Fabrication Progress Chart-1.

3.2 MICRO-FABRICATION WITH FS-LASER LITHOGRAPHY PROCESS

Surface material ablation by short pulsed-laser irradiation is a new and promising technique for precisely micro structuring thin-films [26]. Using this technique, selective film scribing and etching could also be managed without using any mask. With this motivation, we experimentally studied on this technique as introduced in Figure 3.7.

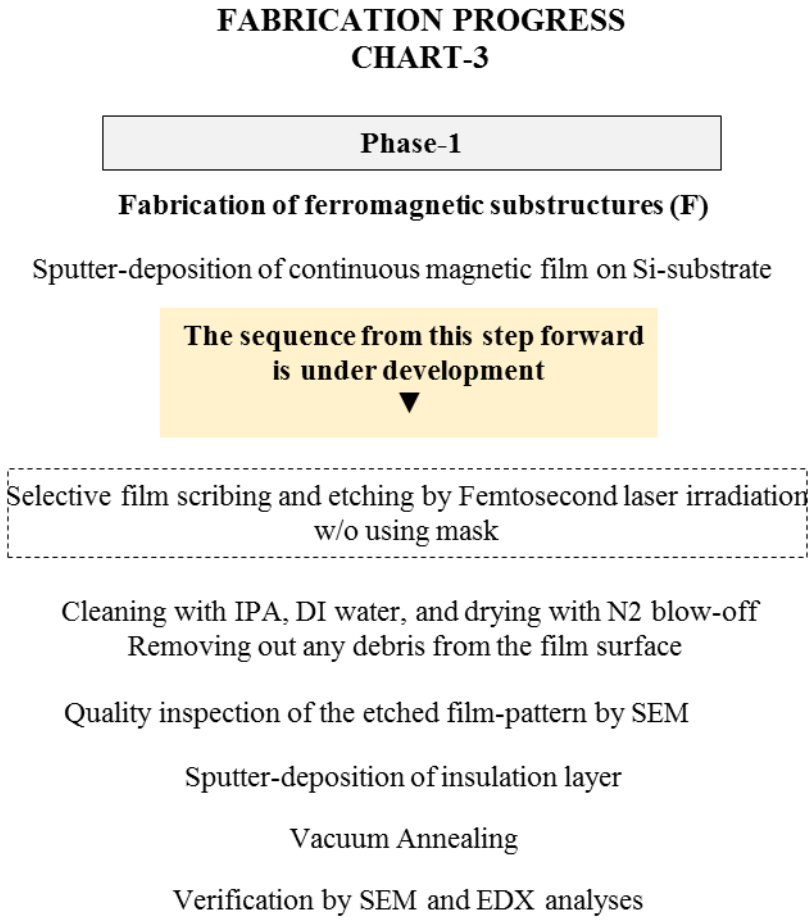

Figure 3.7: Fabrication process with pulsed-laser assisted micro-patterning technique. Fabrication Progress Chart-3 is currently under development.

Magnetic thin Py-films were sputter-deposited on sapphire substrates in 200 nm thickness, and selectively patterned by femtosecond-laser irradiation. Following the laser ablation process, samples were cleaned with acetone and IPA with the help of cue tip. We performed a number of micro-structural analyses of the laser-processed Py-films using scanning electron microscopy (SEM) technique. Figure 3.8 shows an SEM image of the laser-ablated thin-film with debris on film surface before cleaning.

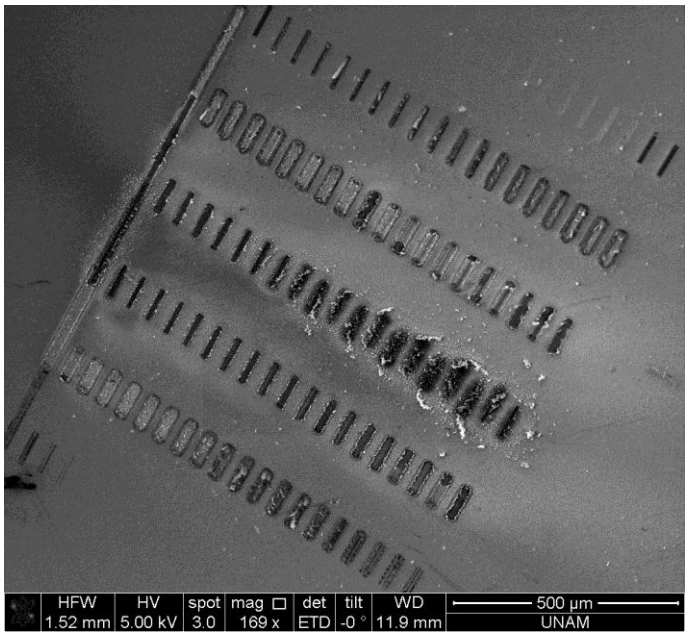

Figure 3.8: Scanning electron micrograph (SEM) with 169x magnification of the laser-ablated thin-film with debris on film surface before cleaning.

Figure 3.9 shows the scanning electron micrograph (SEM) of the laser-ablated thin-film after cleaning. All debris was removed from the film surface. Several micro channels were formed by femtosecond-laser ablation in various optical distances.

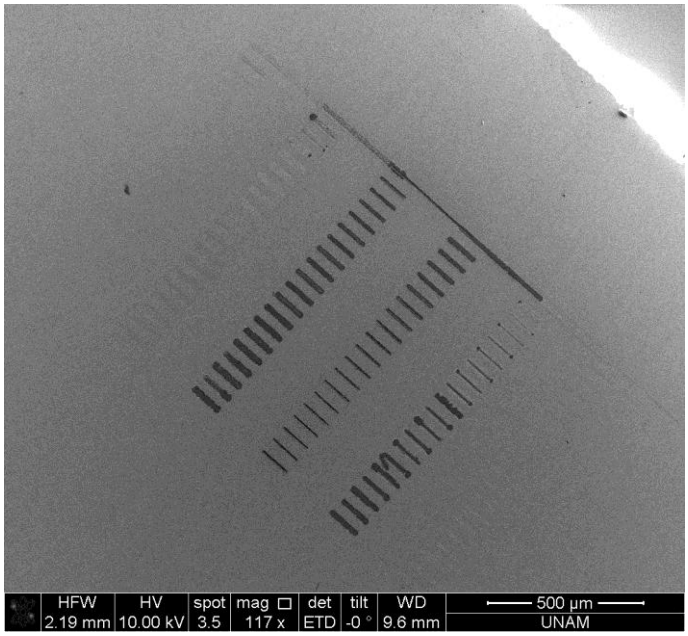

Figure 3.9: Scanning electron micrograph (SEM) with 117x magnification after sample cleaning. Several micro channels were formed by femtosecond-laser ablation in various optical distances.

Depending on the focusing conditions, elliptical shape micro-channels were obtained without ablating any material from the substrate surface as shown in Figure 3.10.

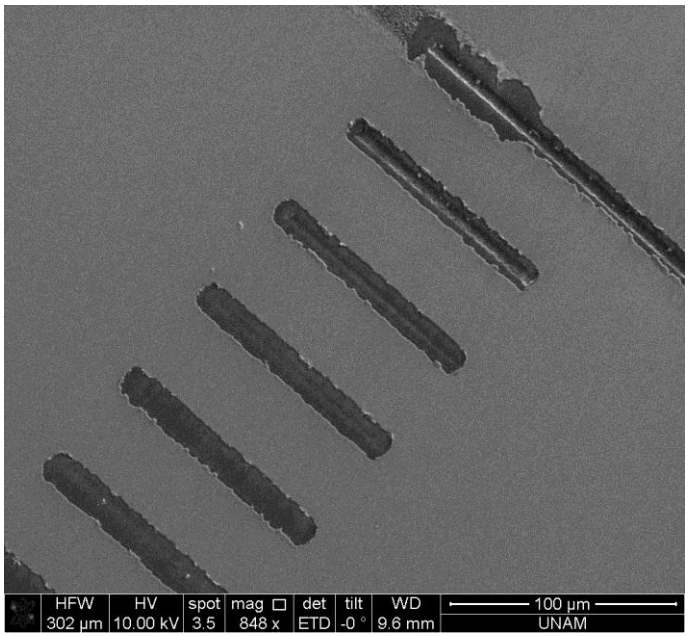

Figure 3.10: Scanning electron micrograph (SEM) of the micro-patterned thin-film at 848x magnification.

Figure 3.11 shows a scanning electron micrograph (SEM) of a laser-ablated micro-channel after sample cleaning. The image was taken at 4000x magnification. There was no any attack on the sapphire substrate caused by laser irradiation. After laser ablation, deep grooves were formed depending on the laser spot diameter.

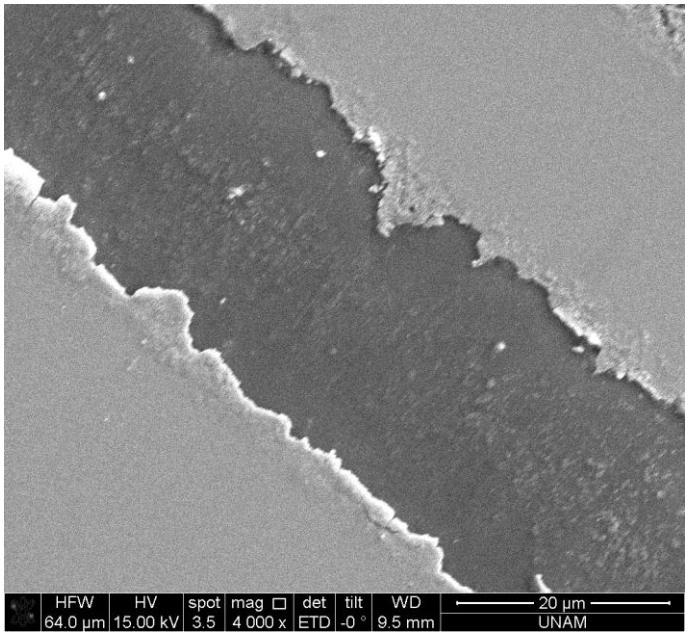

Figure 3.11: Scanning electron micrograph of a laser-ablated micro-channel at 4,000x magnification.

As reference to the above SEM micrographs, micro-patterning process was successfully performed using pulsed-laser scribing. Thin-film peeling without etching substrate was achieved, but it was not possible to observe in which the ideal focus point was happened. The minimum width of micro-channels was measured about 32 µm without any ablation of substrate surface as shown in Figure 3.12.

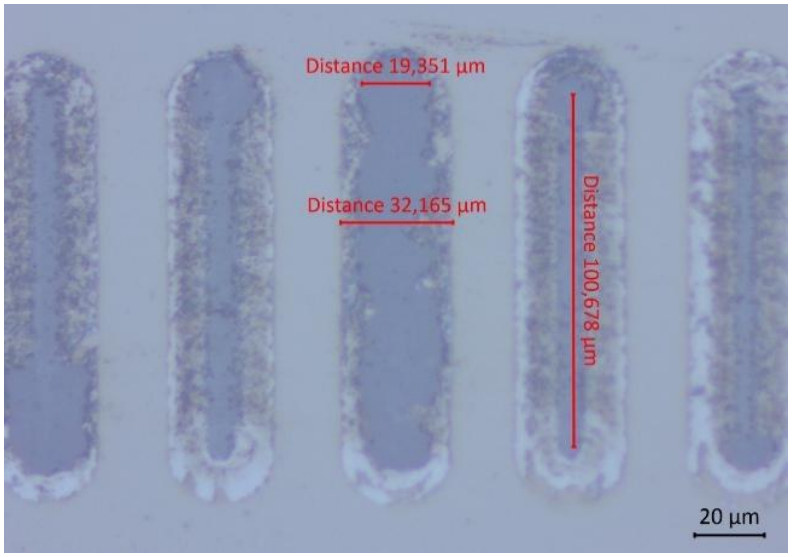

Figure 3.12: Microscope image with 50x objective lens.

The reason was that power was not enough at out of focus regimes of laser light to ablate sapphire, but on the other hand, it can easily peel thin-film from the substrate in

sections 1 to 3 as shown in Figure 3.13. But, this power was still so high that we could not precisely control the width of micro-channels. At the focus point, there was high energy, and so substrate was easily ablated.

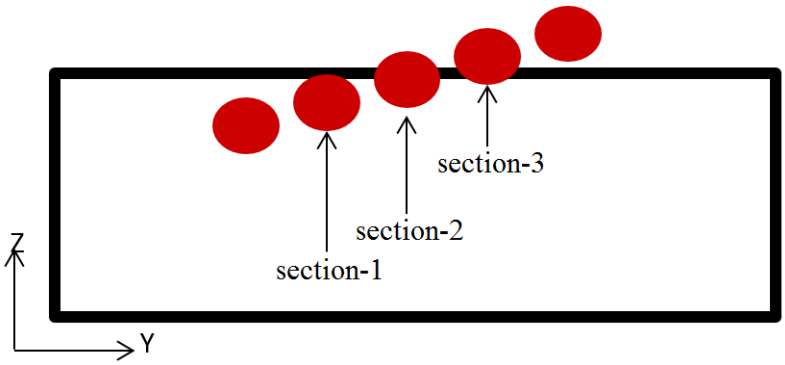

Figure 3.13: It can easily remove thin-film from the substrate in sections 1 to 3.

In the direct femtosecond-laser amplifier/microscopy setup which we used, the system was operated at 800 nm wavelength with about 180 fs pulse duration in 1 kHz repetition rate. The output power of femtosecond laser was 5 mW, which was tuned with half wave plate and polarizer system. Optical distance was changed with 1 µm steps for every line between 7.2 mm and 6.8 mm. One-pass process with a translation speed of about 200 µm/s successfully scribed 200 nm thick Py-films resulting in about 32 µm wide channels.

It has been observed with this experiment that this method could be utilized for nano/micro-patterning of thin Py-films. However, further studies need to be performed to optimize line scribing parameters according to the desired pattern size and shape, and better control of focusing is needed for a well-defined heat affected zone. Laser power can be decreased to 1 mW in order to achieve smaller width sizes of channels.

CHAPTER 4

THIN-FILMS CHARACTERIZATION

The cryogenics laboratory at Melikşah University has been equipped with a 9 T closed-cycle dry-cryostat cryogenics system (1.8-325 K). Before reporting the low-temperature experimental techniques and transport measurements, the cryogenics system and its basic operation were shortly introduced below.

4.1 INTRODUCTION TO CRYOGENICS LABORATORY

The cryogenics system has been mainly consisted of a 9 T superconducting magnet, a closed-cycle dry-cryostat, variable temperature insert (VTI), cryocooler with helium expansion cycle and cold-head device, control electronics and instrumentations.

Figure 4.1 introduces the cryostat and its integrated parts visually. A brief introduction about each system part and its function was given below [27]:

- **Superconducting Magnet;** by Cryomagnetics, Inc. The custom-designed superconducting magnet is a solenoid type, and built using twisted multi-filamentary NbTi wire in a copper matrix. The copper matrix in the wire acts as a form of quench protection along with diodes. The central field is 90 kGauss (9 T) at 4.2 K.
- **Cryostat;** a cryogen-free cryostat with no need of liquid cryogens for cooling down or normal operation. Measured sample base-temperature is 1.8 K, maximum sample test temperature is 300 K.

9 Tesla closed-cycle dry-cryostat cryogenics system (1.8 K – 325 K)

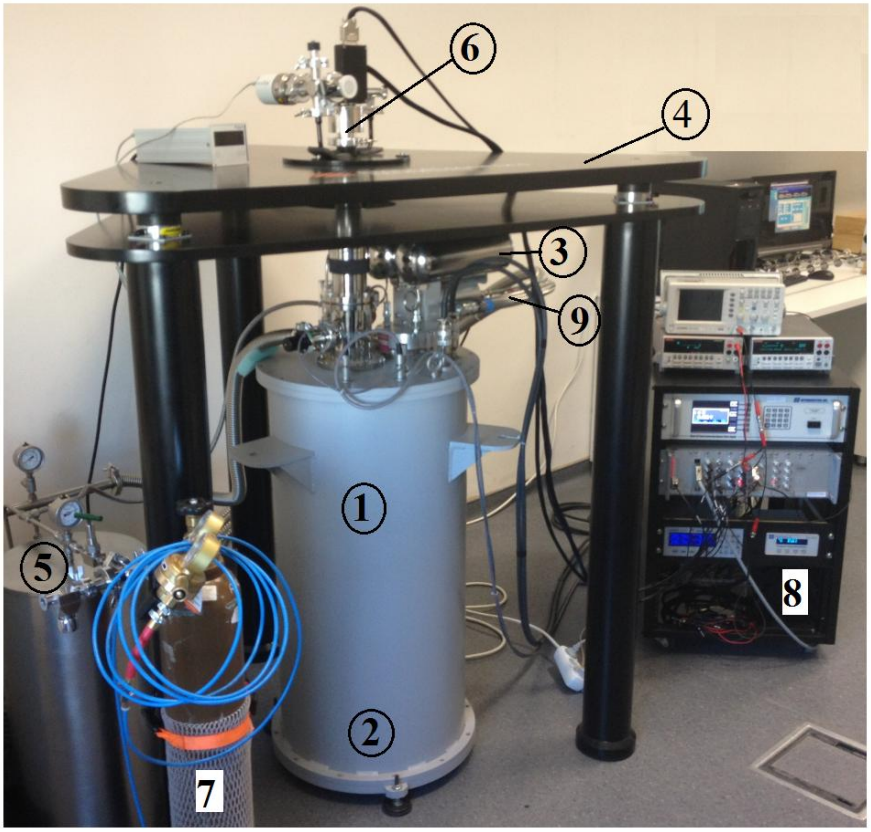

No.	Description
1	Cryogen-free Cryostat
2	Superconducting Magnet (9 T)
3	Pulse Tube Cryocooler (4.2 K)
4	Ultra-low vibration platform with pneumatically dampened tripods
5	Gas Handling System closed-loop operation of He for temperature control
6	Variable Temperature Insert (VTI) in the 49 mm dia. sample space
7	Helium exchange gas to fill in the sample space
8	Instrumentation & Control Electronics Superconducting Magnet Power Supply Current Source & Meter Cryogenic Temperature Monitor & Control Magnetic Field Monitor & Control Sensors
9	Helium flex-line to compressor module

Figure 4.1: Introduction of 9 Tesla closed-cycle dry-cryostat cryogenics system (1.8 K-325 K) at the cryogenics laboratory of Melikşah University [27].

- **Variable Temperature Insert (VTI);** the VTI uses a continuous flowing gas source which is cooled to less than 2 K by heat exchangers attached to the cryocooler and a needle valve. A continuous flow of dry helium is used to cool the tail of the VTI, and thus the exchange gas in the sample space. The sample itself sits in an exchange gas which is not part of the circulation loop to minimize any contamination. One heater (loop 2) is positioned on the exit of the needle valve, the so-called vaporizer. A second heater (loop 1) is positioned on the sample itself. The heaters are used to control the sample temperature. Two Cernox temperature sensors are used to monitor the temperature of the vaporizer and the sample [27].
- **Cryocooler;** manufactured by Cryomech, Inc. A cryogenic refrigeration system based upon a closed loop helium expansion cycle. It consists of a compressor package, helium flex lines and a cold head (expansion device). The compressor package houses the compressor module and all other components that cool and purify helium. The compressor package compresses the low-pressure helium returning from the cold head and provides clean high-pressure helium to the cold head. The helium flex lines transport helium between compressor package and the cold head. Finally, the cold head expansion device expands the helium using a pulse tube, and the heat exchangers on the cold head provide cooling at cryogenic temperatures by transferring heat to the helium within the system [27]. In case of not being able to cool the cryostat to base-temperature due to ice-blockage of the needle valve which may be caused by frost formation of any impurities available in the helium gas, then the system is warmed up, and re-charged with clean helium (reported impurities are 1.4 ppm O_2 and 1 ppm moisture typically).
- **Control Electronics;** the control electronics is an integral part of the system including; temperature controller, current sourcing and data acquisition instruments, magnet power supply unit, and the operating software.

4.2 EXPERIMENTAL TECHNIQUES

We used standard four-point probe technique to collect I-V data from the samples under various applied magnetic fields from zero to 7 kOe and at temperatures in the range of 3-10 K. Before reporting the low-temperature experimental results, a brief introduction about standard four-point probe technique and sample preparation steps was given below:

4.2.1 Standard Four-point Probe Transport Measurement Technique

4.2.1.1 Description

DC resistivity measurements have been conducted by means of four-point probe technique. Figure 4.2 shows the schematic sketch of the measurement setup.

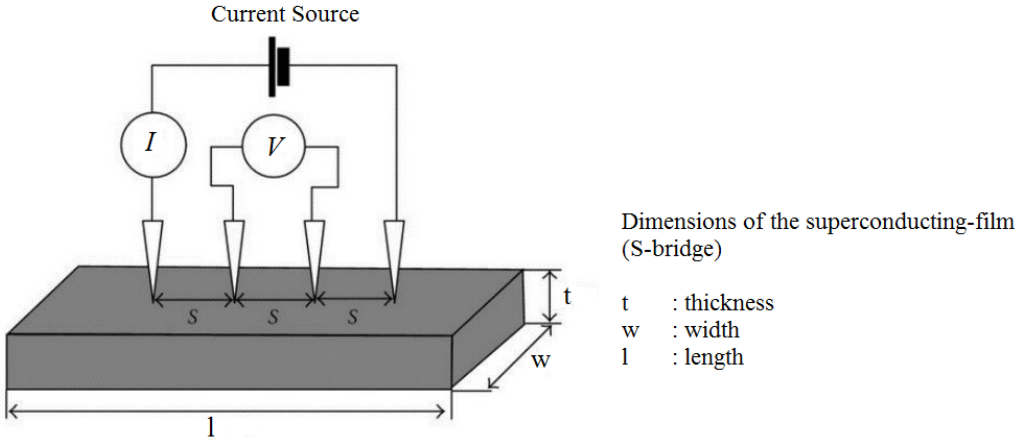

Figure 4.2: Schematic sketch of four-point probe transport measurement setup. A dc current of 100 μA flows in PbBi-film either along or across the underlying magnetic Py-stripes. I-V data were collected at temperatures in the range of 3-10 K while the samples were swept under an external field forward from zero to 7 kOe, and backward.

In order to determine the critical temperature (T_C) values; a dc current of 100 μA was passed through the superconducting film, and the voltage drops across voltage leads were measured while the samples were cooling from RT down to 3 K. The collected I-V data stream belonging to PbBi control sample and F/S hybrid samples were transferred to graphing workspace. Each data stream was processed, and the calculated R (T) data stream was plotted in the temperature range of 3 to 10 K. The critical values were defined by extrapolation of the resistance curves to zero. During I-V data collection,

temperature was swept from $T>T_C$ to $T<T_C$ at several H-fields, and then the T_C values were determined from the R (T) curves as a function of H to complete the phase diagrams of the samples. The externally applied H-field was swept from zero to 7 kOe, and then it was swept backward to the zero.

4.2.1.2 Sample Preparation before Transport Measurements

(a) Wire Bonding between F/S Hybrid Samples and the Sample Puck

For this very delicate operation, we used powder-free disposable latex gloves, fine tip tweezers, razors, toothpicks, vacuum grease, glass slides, 50 μm dia. copper wire, indium wire, soldering tool, and an optical microscope set on a vibration-free workbench. As cleanliness is very important to ensure a proper operation at low temperature, we first cleaned the sample puck with acetone and IPA, dried with nitrogen blow-off to get rid of any dirt and grease. We used lint-free tissue moistened with acetone. Pieces of 5 cm long copper wire (in 50 μm dia.) were used to make electrical connections from each silver contact pad to its respective pin on the sample puck. The copper wire pieces were soldered to pins on sample puck, and straightened gently. Then, we applied a little amount of vacuum grease on the gold-coated surface of the sample puck with the help of a toothpick for ensuring better thermal conductivity of samples at LT. Silicon substrate was gently placed on the greased-surface of the puck. A small piece of indium was picked up with a toothpick, and delicately pressed onto the silver contact pad, so that indium was sticked on silver pad. Each loose end of copper wire was held with a fine tip tweezers, and gently kept in close with silver contact pad under optical microscope view. And, another small piece of indium was picked up with a toothpick, and delicately pressed toward the silver contact pad so sandwiching the loose end of copper wire. Figure 4.3 shows the samples wire-bonded onto the puck.

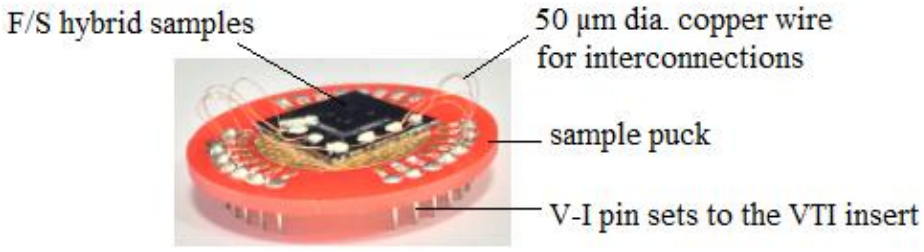

Figure 4.3: Wire-bonding between F/S hybrid samples and V-I pin sets of sample puck.

We designed such a sample puck that we were able to test multiple samples on it. Having completed wire-bonding process, we inspected all interconnections, solder joints and intact of contact pads under optical microscope view.

(b) Mounting the Sample Puck on the VTI Head

We inserted the sample puck onto VTI head, and performed a test measurement by flowing a dc current of 100 μA. Voltage drops across voltage leads were measured. This was the final electrical inspection of each sample before inserting into the cryostat. In case of any bad contact; we applied a little amount of silver paint on the bad contact pad, and waited for silver paint about 15 min to dry, and tested the samples again before inserting the VTI into the cryostat.

(c) Inserting the VTI into Cryostat

We set the temperature to 300 K. We flushed the system with helium gas, and slowly inserted the VTI into cryostat. We used the plastic centering ring and radiation shields as a guide during insertion so that the VTI head was not touching anywhere in the sample space. We tightened KF40 flange using its clamp. We flushed the sample space with helium gas couple of times to purge all the gas trapped inside sample space. We kept helium gas pressure inside sample space never less than 1 bar above the atmospheric. We cooled down or warmed up the sample with a max rate of 2-3 K/min as higher rates may cause damage in time.

4.3 LOW-TEMPERATURE TRANSPORT MEASUREMENTS

In order to reveal the directional current flow dependency of superconductivity properties with respect to the orientation of underlying Py-stripes, we investigated the exclusive transport characteristics of the F/S hybrid samples, and analyzed the obtained data in graphing workspaces.

4.3.1 Control Sample

Figure 4.4 shows the typical normalized resistance curves of R(T)/R(8K) for the control sample without Py-stripes under various H-fields of 0, 0.5, 1, 2, 3, 5, and 7 kOe.

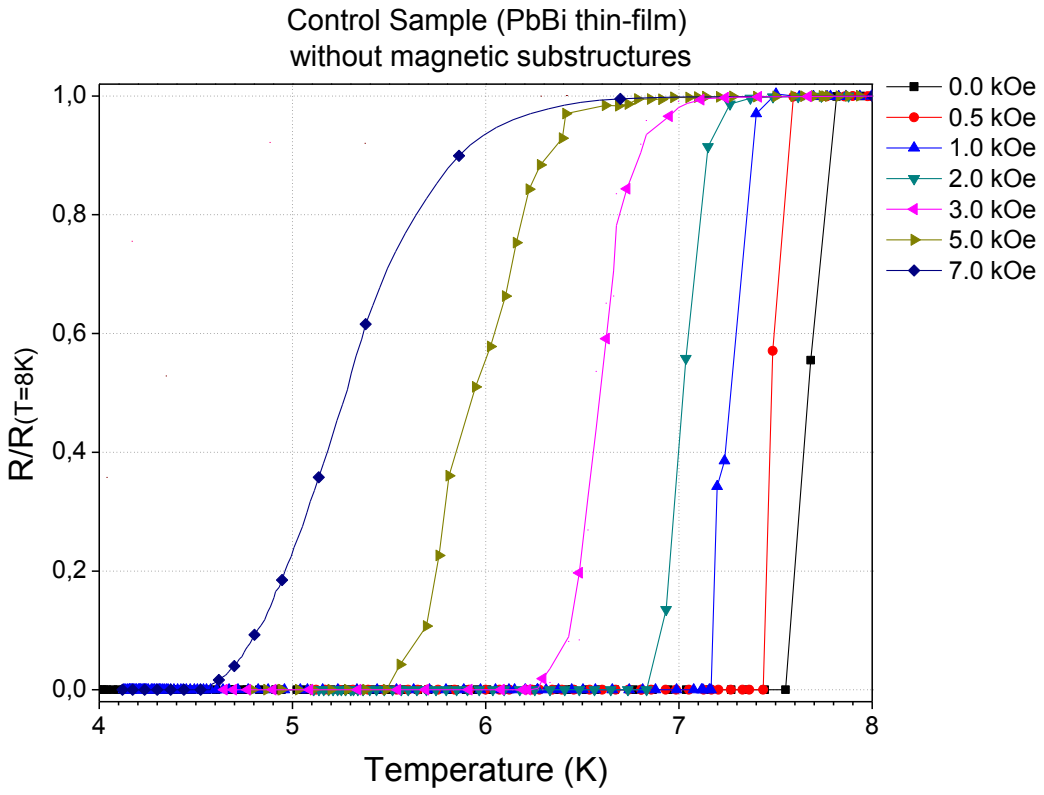

Figure 4.4: Normalized resistance curves of R(T)/R(8K) for the control sample without underlying Py-stripes under various H-fields from zero to 7 kOe. Onset Tc= 7.67 K at zero field.

4.3.2 F/S Hybrid with parallel Py-stripes

In this configuration, the parallel Py-stripes were oriented along the superconducting film (S-bridge). Figure 4.5 shows the typical normalized resistance curves of R(T)/R(8K) for the current flowing parallel to the ferromagnetic Py-stripes under various H-fields of 0, 0.5, 1, 2, 3, 4, 5, and 7 kOe.

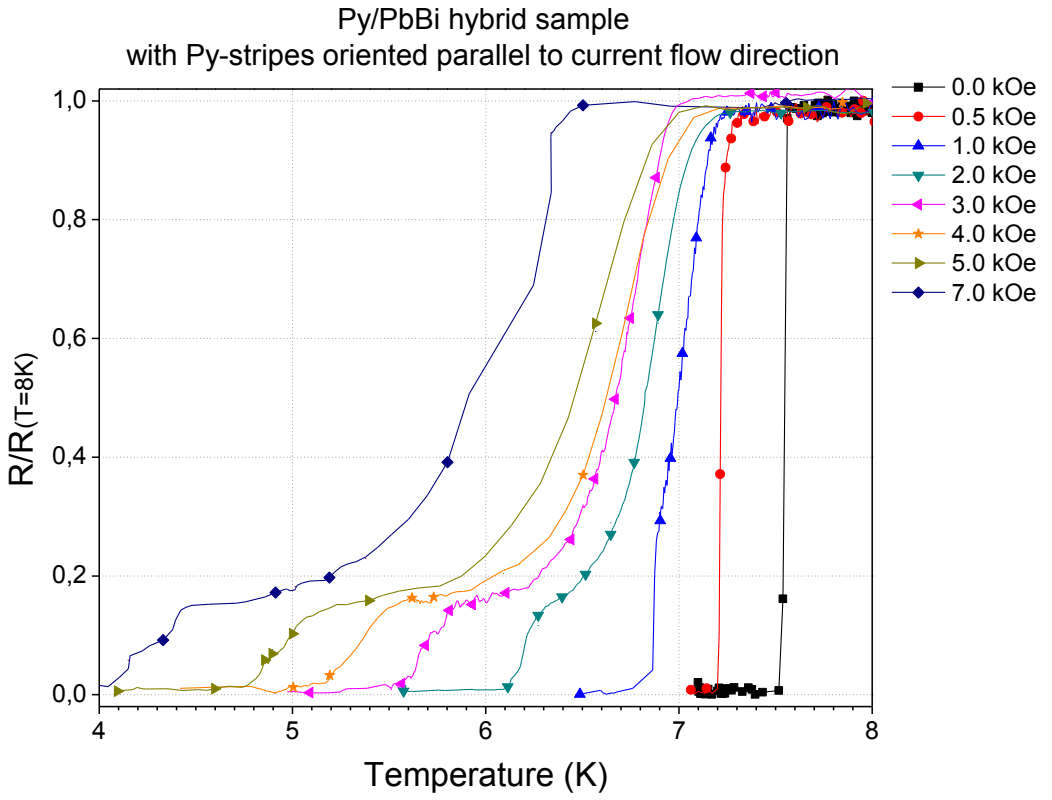

Figure 4.5: Normalized resistance curves of R(T)/R(8K) for the current flowing parallel to the ferromagnetic Py-stripes under various H-fields from zero to 7 kOe. Onset Tc= 7.67 K at zero field.

A different result occurs when Py-stripes were oriented parallel with the PbBi-film. Onset T_C values have been shifted to lower temperatures with respect to that of the control sample. The typical normalized resistance curves display a kink followed by a much slower decrease in the slope below onset critical temperature showing an inhomogeneous transition of the F/S hybrid with underlying parallel Py-stripes. The relative difference between the curves measured in the F/S hybrid with Py-stripes and in the control sample without Py-stripes becomes larger at lower temperatures.

Magnetic Py-stripes in parallel orientation to the PbBi-film have been polarized by the external magnetic field, and the resulting stray fields at the stripe edges caused the suppression of superconductivity, and increase of resistance. Thereof, easy current channels have been formed by the long edges of magnetic Py-stripes oriented parallel to the PbBi-film.

4.3.3 F/S Hybrid with perpendicular Py-stripes

In this configuration, the perpendicular Py-stripes were oriented transverse to the superconducting film (S-bridge). Figure 4.6 shows the typical normalized resistance curves of R(T)/R(8K) for the current flowing perpendicular to the ferromagnetic Py-stripes under various H-fields of 0, 0.5, 1, 2, 3, 4, 5, and 7 kOe.

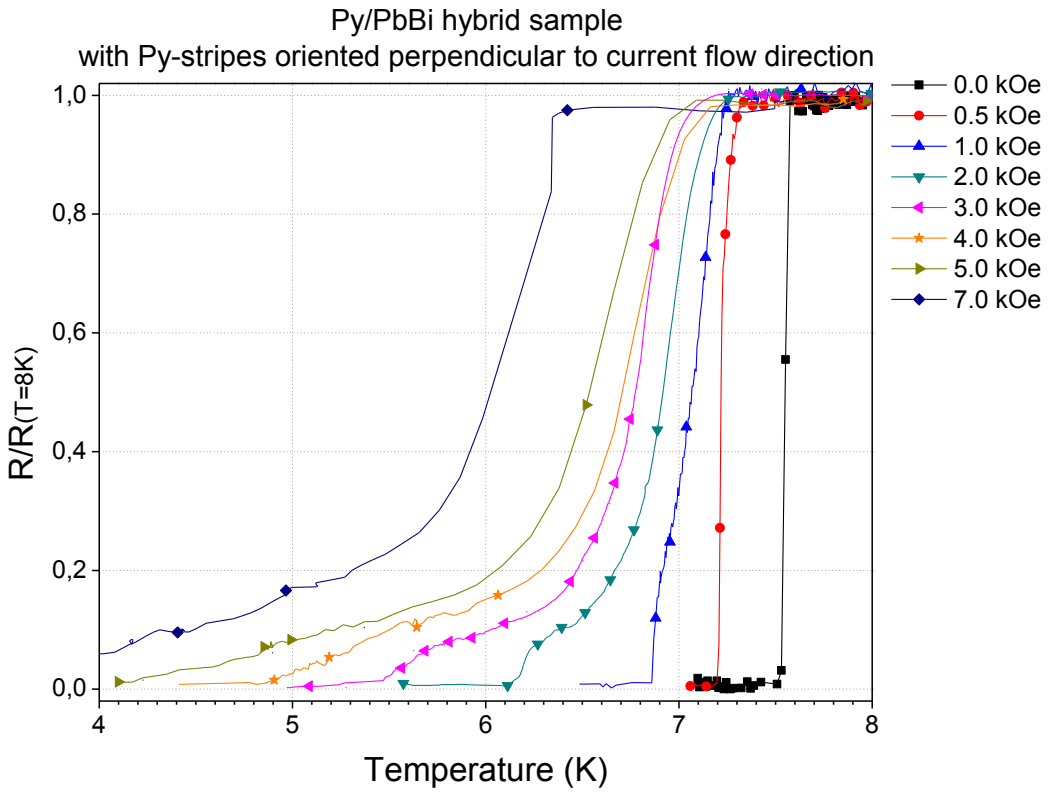

Figure 4.6: Normalized resistance curves of R(T)/R(8K) for the current flowing perpendicular to the ferromagnetic Py-stripes under various H-fields from zero to 7 kOe. Onset Tc= 7.67 K at zero field.

A different result occurs when the Py-stripes were oriented perpendicular to the PbBi-film. Onset T_C values have been shifted to lower temperatures with respect to that

of the control sample. The typical normalized resistance curves display a kink followed by a much slower decrease in the slope below onset critical temperature showing an inhomogeneous transition of the F/S hybrid with underlying perpendicular Py-stripes. The relative difference between the curves measured in the F/S hybrid with Py-stripes and in the control sample without Py-stripes becomes larger at low temperatures.

Magnetic Py-stripes in perpendicular orientation to the PbBi-film have been polarized by the external magnetic field, and the resulting stray fields at the stripe edges caused the suppression of superconductivity and increase of resistance. Thereof, continuous barriers have been formed for the transverse current flow through the long edges of magnetic Py-stripes.

4.3.4 The Transport Measurement Results

Referring to the low-temperature transport measurements of the F/S hybrids and the control samples, it has been unveiled that all samples have the same superconducting transition onset temperature, Tc = 7.67 K at zero field.

An anomalous widening of R (T) transition curve is present especially after the resistance fell to 20% of its residual resistance value as if there are two distinct transitions are present in the data. This indicates co-presence of superconducting and normal regions simultaneously in the superconducting film.

The F/S hybrids with underlying parallel and perpendicular Py-stripes exhibited parts with quite different T_C (H), so that defining the critical current density (J_C) is complicated and somewhat meaningless for these hybrid samples. This result also gives an anomalous extra broadening of R (T) in a magnetic field which makes H_{C2} (T) less reliable for that case. The midpoint of the R (T) curve or the extrapolation of the steepest part to R=0 was chosen to determine the H_{C2} (T) for inhomogeneous hybrid films.

The periodic modulation of applied magnetic field in the superconducting PbBi-film results in various H_{C2} (T) values for each sample. Figure 4.7 shows H_{C2} (T) plots belonging to the F/S hybrids with underlying parallel and perpendicular Py-stripes, and the control sample.

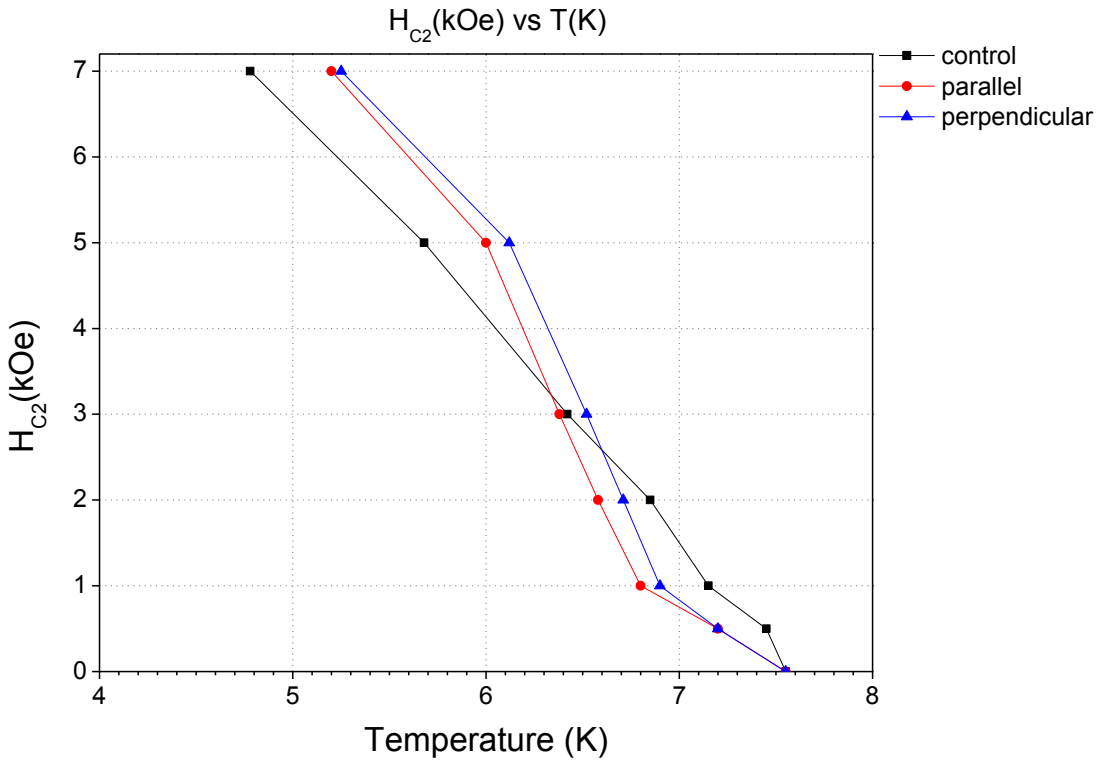

Figure 4.7: H_{C2} (T) for all samples when only the initial transition is considered.

Magnetic Py-film saturates out-of-plane between zero and 3 kOe. In this saturation regime of Py-film, F/S hybrids showed enhancement in the second critical field H_{C2} compared to the control sample due to the effect of magnetic pinning.

The resulting magnetic field in the superconducting film above the non-magnetic region is lower than the applied field, while higher than the applied field in the superconducting film above the Py-stripes.

The effective field is redistributed inhomogeneously across the Py-stripes. Since H increases as T decreases, a larger portion of the film over the non-magnetic regions becomes superconducting while a smaller portion of the film over the Py-stripes is driven normal by the field as the temperature is decreased.

Due to the high magnetic permeability of thin Py-stripes, the applied field is redistributed over the superconducting film resulting in a magnetic modulation pattern with low and high field regions. These two stripe-patterns are achieved by simply changing the orientation of the underlying Py-stripes in parallel or perpendicular to the

current flow direction. Due to the field localization by Py-stripes, intermittent superconducting and normal conducting regions are formed in PbBi-film. Depending on the current flow direction, the superconducting and normal conducting regions are naturally configured into either parallel or series connections of superconducting and normal conduction paths.

These effects can explain the differences among the measured H_{C2} for the F/S hybrids compared to that of the control sample. The resulting magnetic field in the superconducting film above the non-magnetic parts is lower than the externally applied magnetic field H, while the resulting magnetic field in the film above the magnetic Py-stripes is higher than the applied field H. This low and high periodic field variation in the superconducting film will result in different values of the H_{C2}, and for directions parallel and perpendicular to the underlying Py-stripes with respect to the control sample. Normalized resistance curves of the samples at 1 kOe, 3 kOe, and 5 kOe fields are shown in Figures 4.8, 4.9, and 4.10, respectively.

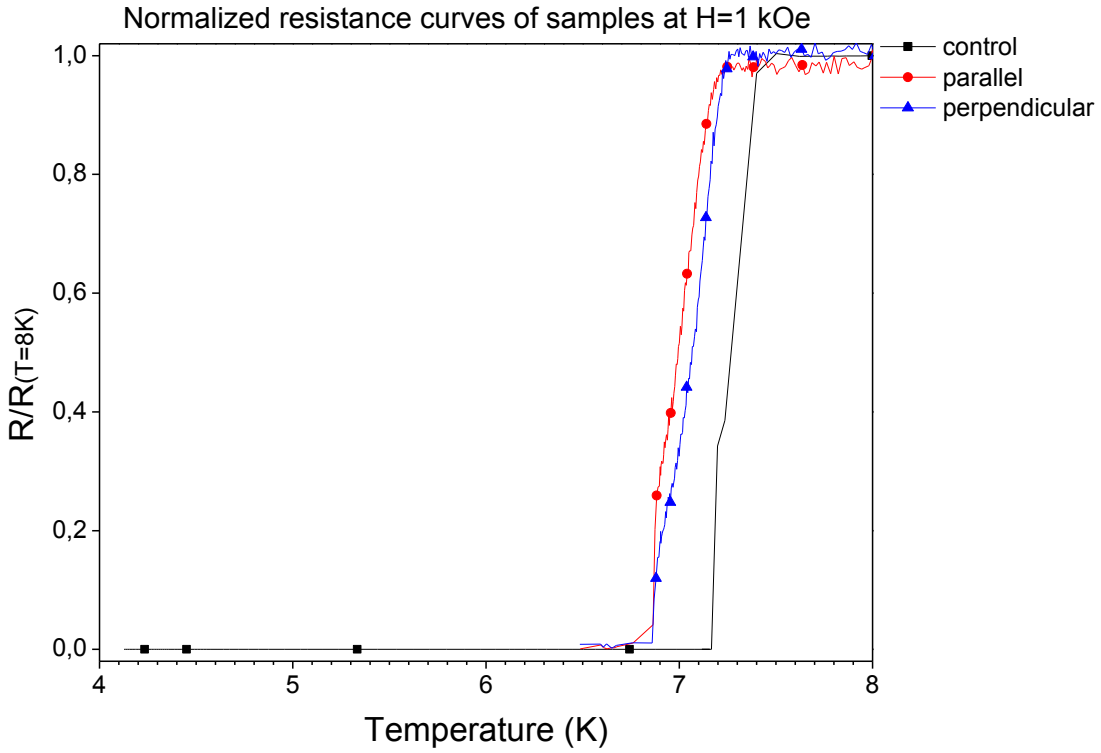

Figure 4.8: Normalized resistance curves of R(T)/R(8K) at H=1 kOe magnetic field.

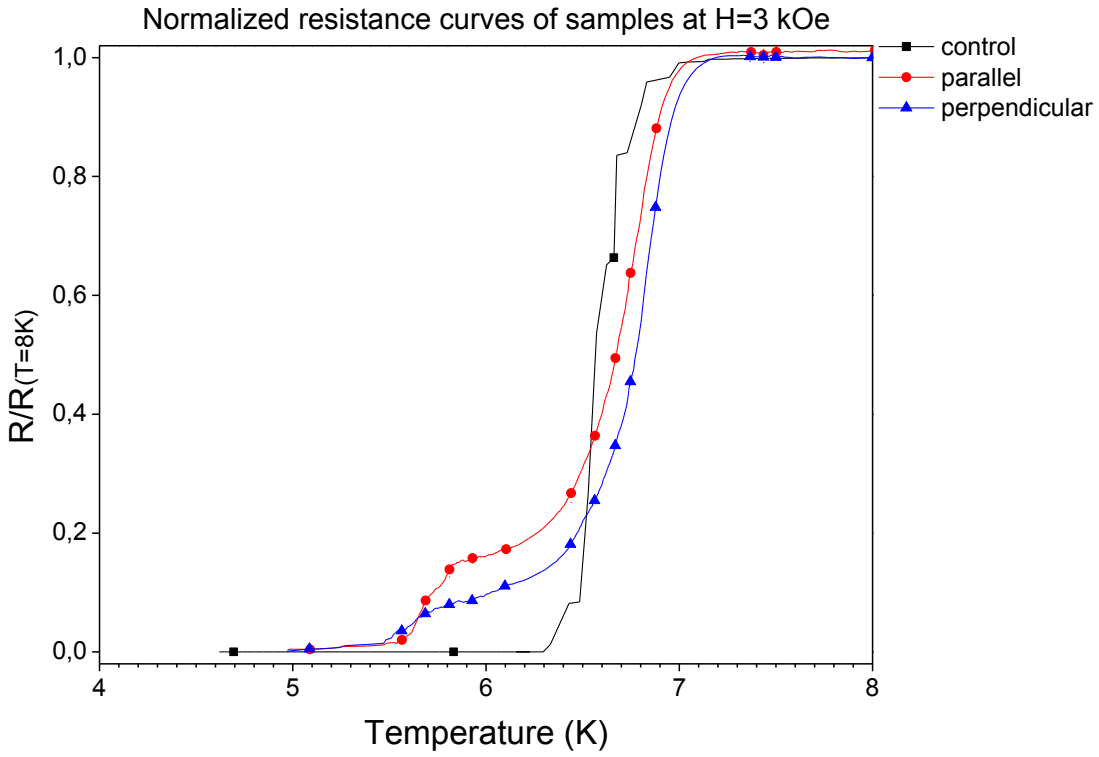

Figure 4.9: Normalized resistance curves of R(T)/R(8K) at H=3 kOe magnetic field.

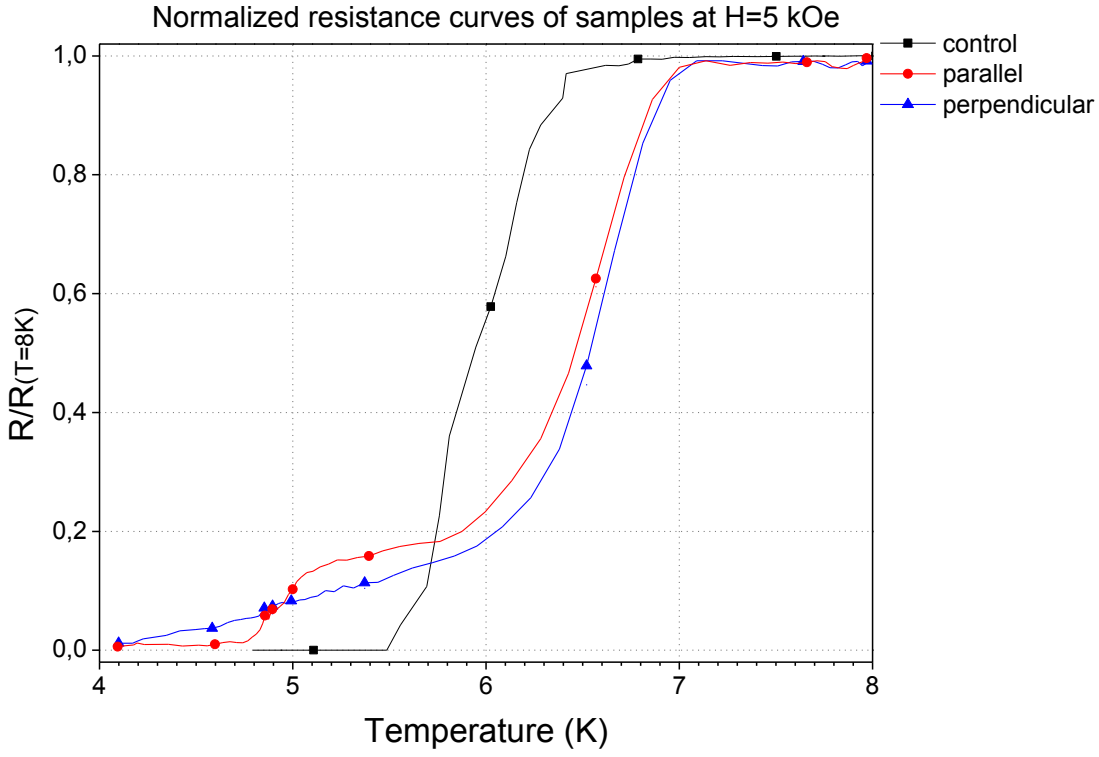

Figure 4.10: Normalized resistance curves of R(T)/R(8K) at H=5 kOe magnetic field.

Finally, we clearly observed that changing the orientation of magnetic Py-stripes with respect to the current flow direction, the superconducting properties such as T_C and H_{C2} can be controlled and regulated.

The corrugation of PbBi-film at the edges of Py-stripes causes a transverse deformation in the layered structure. The topographical effects due to this surface corrugation of the PbBi overlayer could be another topic of research, but not probed in the scope of our research here.

CHAPTER 5

MECHANICAL PROPERTIES of SUPERCONDUCTING MgB_2 THIN-FILMS

Magnesium diboride (MgB_2) is a simple, binary, non-oxide compound [28-30]. High-quality thin-films, Josephson Junctions and circuits made of MgB_2 are of high importance for future superconducting-electronic applications [31-33]. Its critical temperature (T_C) of 39 K is the highest amongst non-oxide superconductors. Figure 5.1 shows an illustrative presentation answering why MgB_2 could be a promising candidate for the future superconducting applications.

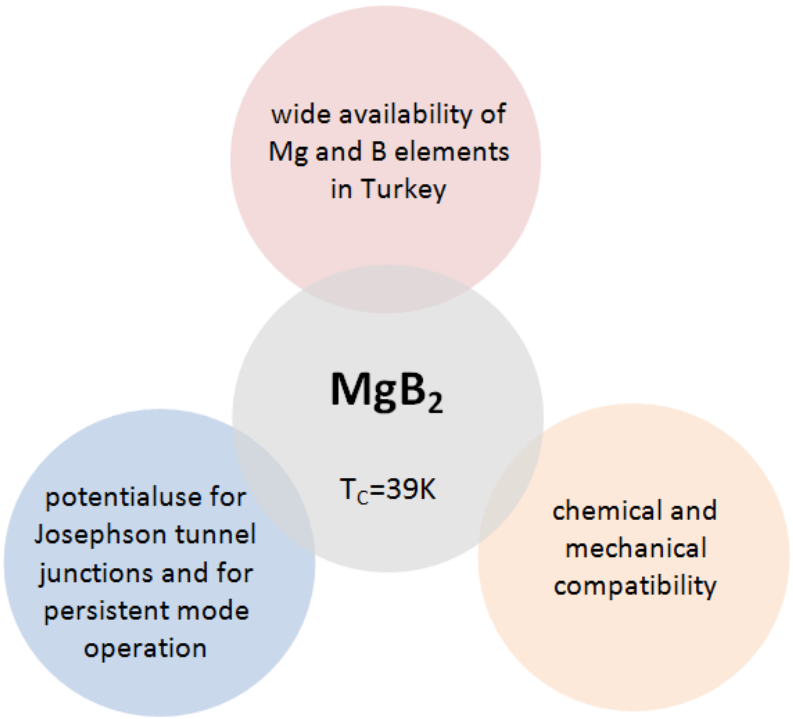

Figure 5.1: An illustrative presentation answering why MgB_2 could be a promising candidate for the future superconducting applications.

To date since the discovery of its superconductivity by the group of Akimitsu in 2001, several groups have reported on superconducting MgB_2 thin-films grown by various vapor-deposition techniques.

In [34], the research group led by Ozmetin studied on the fabrication and characterization of superconducting MgB_2 thin-films. So, we briefly reported on the mechanical properties of superconducting MgB_2 thin-films in this chapter.

5.1 FABRICATION

A composite sputtering target was manufactured from pure Mg powders with particle size of 44 μm and pure B powders with particle size of 2 μm. Powders were weighed using a precision balance. First, Mg powders were pressed inside a 2" diameter copper casing to form a thin-Mg layer for better thermal conductivity. Then, the weighed amounts of Mg and B powders were firmly pressed into the copper casing. Mg and B powders were separated half and half spatially as shown in Figure 5.2.

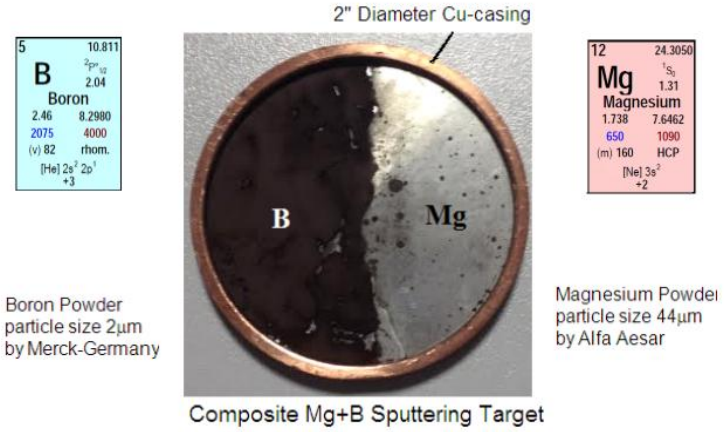

Figure 5.2: A homemade composite sputtering target was manufactured from pure Mg and B powders, spatially separated in half and half, and firmly pressed into a 2" diameter copper casing [34].

We used RF magnetron sputtering technique to grow MgB_2 thin-films both on silicon and sapphire substrates. The fabrication of high-quality MgB_2 thin-films proved to be complicated and challenging due to the large difference in vapor pressure between B and Mg elements, and also due to the fact that Mg oxidizes easily. Several measures were implemented to prevent Mg from oxidation by using LN_2 cold finger, and also by Mg-sublimation process to trap and confine free oxygen molecules in the chamber.

Figure 5.3 shows a photograph of the finalized MgB_2 thin-film samples grown both on silicon and sapphire substrates.

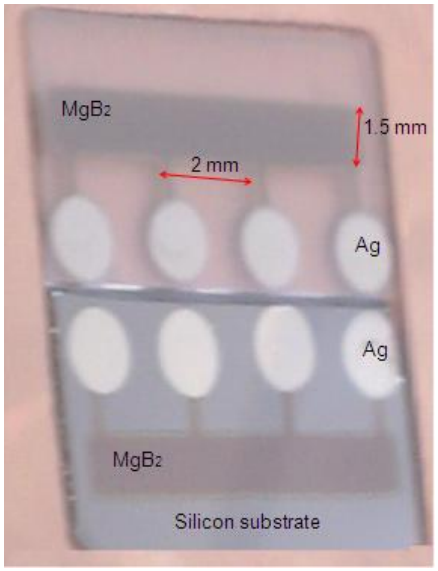

Figure 5.3: A photograph of the finalized MgB_2 thin-film samples grown on silicon and sapphire substrates [34].

5.2 CHARACTERIZATION

We conducted a number of analyses on the MgB_2 thin-film samples including chemical analysis by GIXRD, micro-structural analysis by SEM, and mechanical analysis by Nano-indentation tests.

5.2.1 Chemical Analysis by GIXRD

GIXRD technique allows pre-scanning of thin-films to adjust the X-ray incidence angle at around 1° such that it only receives signals from thin-film material instead of the substrate. GIXRD data for the as-deposited (shown in red at bottom) and annealed (shown in blue at top) MgB_2 thin-film samples were shown in Figure 5.4. Diffraction peaks at $2\theta=42.4°$ from plane (101) and at $2\theta=62°$ from plane (102) in the pattern reveal the successful constitution of MgB_2 phases.

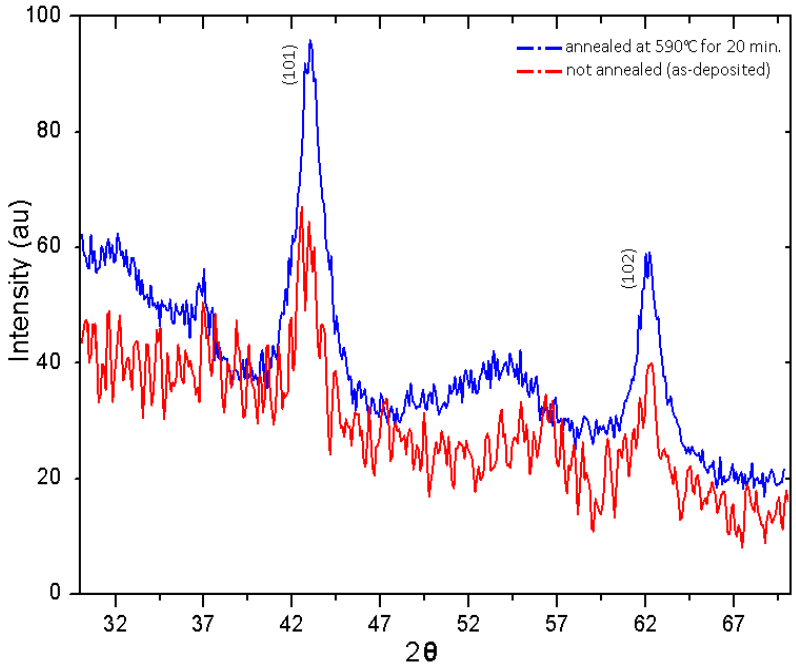

Figure 5.4: GIXRD data for as-deposited (red at bottom) and annealed (blue at top) MgB_2 thin-film samples. Diffraction peaks at $2\theta=42.4^0$ from plane (101) and at $2\theta=62^0$ from plane (102) in the pattern reveal the successful constitution of MgB_2 phases [34].

5.2.2 Micro-structural Analysis by SEM

Figure 5.5 shows a scanning electron micrograph from the surface of MgB_2 thin-film revealing an average grain size of about 25 nm in diameter.

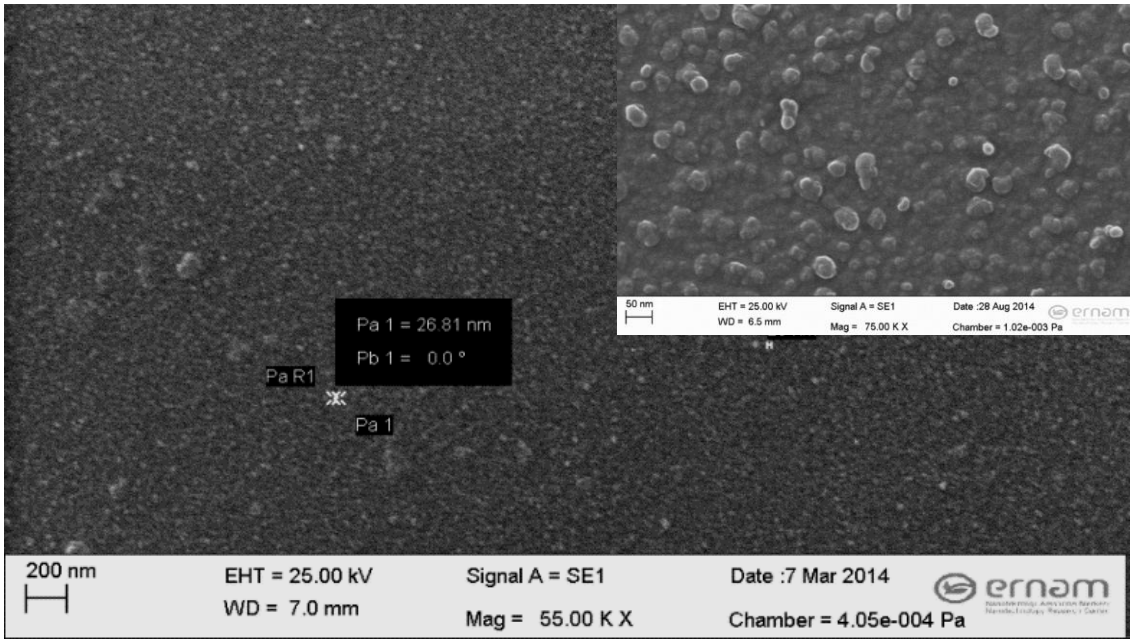

Figure 5.5: A top-view scanning electron micrograph of MgB_2 film with an inserted image taken at 75,000x magnification reveals grain sizes of 20-30 nm [34].

5.2.3 Mechanical Analysis by Nano-Indentation Test

Figure 5.6 shows the typical load-indentation depth curves generated during a Nano-indentation test indicating key parameters necessary for mechanical analysis of the sample. And, Figure 5.7 shows a plot of hardness vs. applied indentation test load.

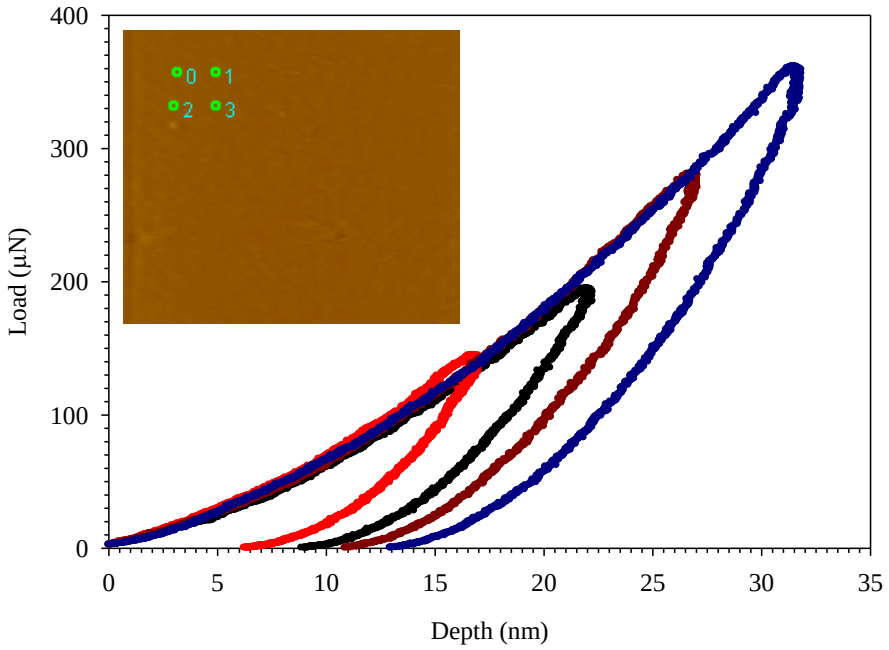

Figure 5.6: Nano indentation test load-depth curve of MgB_2 thin-film sample at room temperature [34].

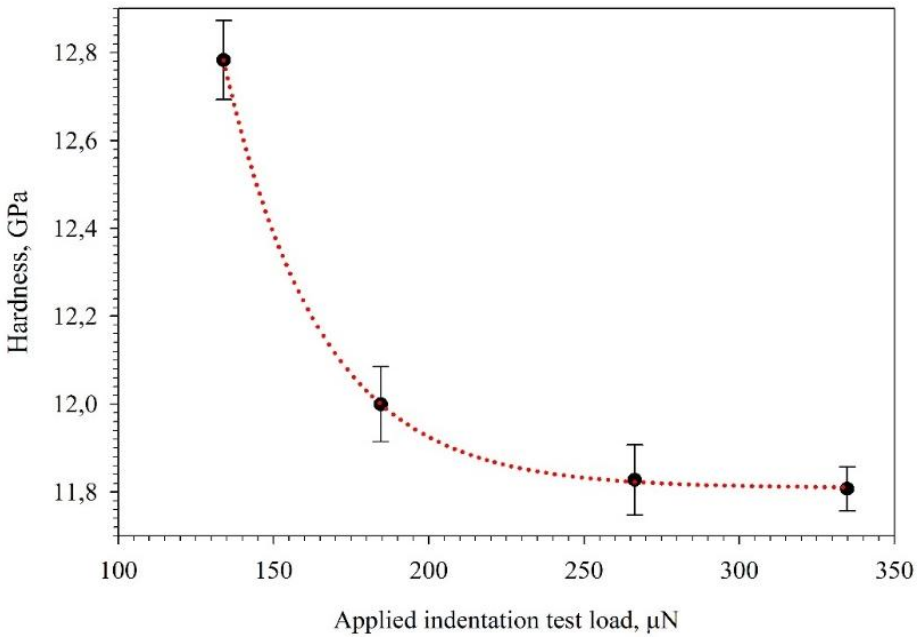

Figure 5.7: A plot of hardness vs. applied indentation test load [34].

Figure 5.8 shows a plot of elastic modulus vs. applied indentation test load.

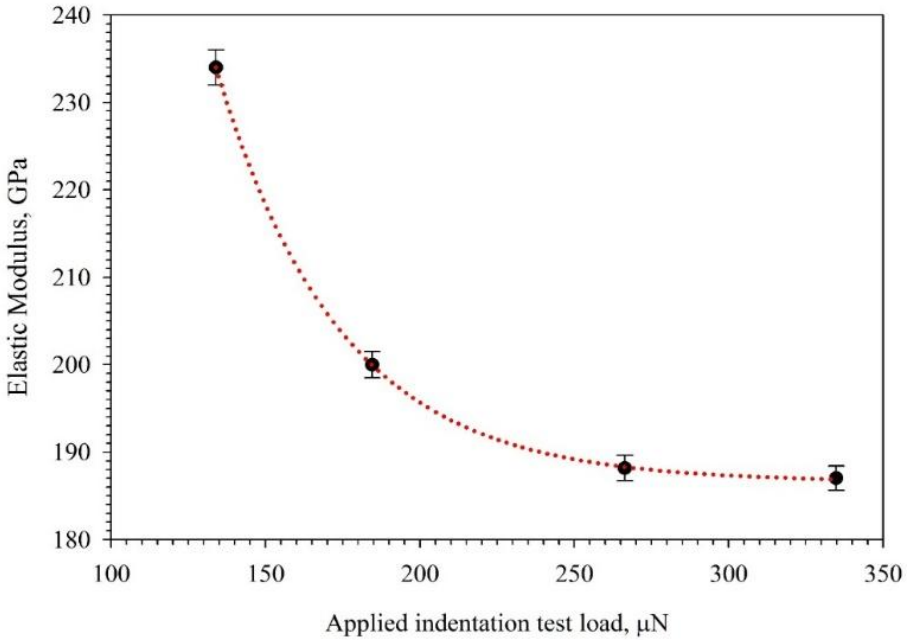

Figure 5.8: A plot of elastic modulus vs. applied indentation test load [34].

In conclusion, MgB_2 thin-films were uniform, well-textured and composed of homogeneously distributed ~25 nm grains. Nano hardness and elastic modulus values were found 11.72 GPa and 178.13 GPa, respectively [34].

CHAPTER 6

CONCLUSIONS

We fabricated superconducting PbBi-films with underlying segments of thin magnetically soft Py-stripes, which were grown in perpendicular and parallel orientations to the current flow direction. By comparing V-I characteristics of the F/S hybrid samples with the bare control sample without Py-stripes; we investigated the directional current flow dependency of the superconductivity properties.

Magnetic Py-stripes were polarized by the externally applied magnetic field, and the resulting stray fields at the stripe edges caused the suppression of superconductivity, and increase of resistance.

Easy current channels were formed by the long edges of magnetic Py-stripes when oriented along the PbBi-film, while continuous barriers were formed for the transverse current flow by the long edges of magnetic Py-stripes when oriented across the PbBi-film.

The H_{C2} second critical field data indicated that in the regime after the magnetic Py-stripes were saturated out of plane, F/S hybrids showed enhancement in the H_{C2} compared to the control sample due to the effect of magnetic pinning.

DC transport measurements revealed that magnetic Py-stripes, oriented along and across the superconducting films, introduce normal and superconducting channels or barriers for current flow resulting in change of superconducting properties, which can guide for designing and fabricating functional superconducting devices.

Micro-fabrication with photolithography process, a multi-step patterning process, was defined and successfully experimented as an alternative technique to grow magnetic substructures.

We also experimented femtosecond-laser assisted etching of thin magnetic films grown on sapphire substrates. With this maskless micro-patterning process, we successfully patterned 200 nm thick Py-films without ablating any substrate material. However, further studies need to be performed to optimize line scribing parameters according to the desired pattern's size and shape, and better control of focusing is needed for a well-defined heat affected zone.

In the Future;

The interaction between adjacent magnetic stripes due to the dipolar fields could be investigated. These effects are expected to influence the second critical field, H_{C2}.

The effects of transverse deformation and surface corrugation of the superconducting overlayer could be investigated specifically. In a recent research [23], it has been noted that when compared to flat superconducting films, the topographical corrugations of the superconducting overlayer near the edges of magnetic substructures could magnify the effect of underlying magnetic substructures on vortex dynamics resulting in additional vortex pinning effect.

By implementing a simple mechanical rotation mechanism, the directional current flow dependency behavior could be utilized to design a functional F/S hybrid device such as a low-power persistent current switch for superconducting applications.

APPENDIX A

INTRODUCTION TO LOW TEMPERATURE SCANNING HALL PROBE MICROSCOPY (LT-SHPM)

The here below introductory information about the Low Temperature Scanning Hall Probe Microscope (LT-SHPM) System and its operation has been collected and summarized from the Supplier's User Manual [35].

The LT-SHPM system mainly consists of microscope insert, sample puck, control electronics, microscope handling kit, and computer workstation. The system uses scanning tunneling microscope (STM) feedback to approach and track the surface as the specimen is scanned by the Hall sensor. Figure A.1 schematically illustrates the principle of an STM operation.

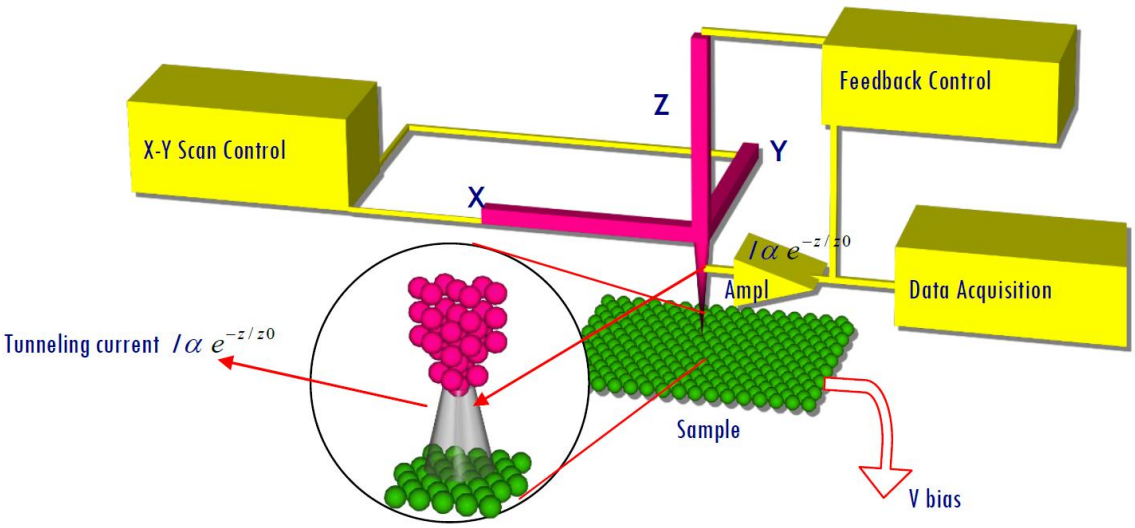

Figure A.1: Schematic illustration of the STM principles [35].

In an STM system, a biased tip scans the surface while the tunnel current is present between tip and the conducting sample as shown in Figure A.1 above.

The tunnel current is an exponential function of tip-sample separation and decays by a factor of ten for every one Angstrom increase in the separation. A piezoelectric ceramic scanner is used to move the tip/sensor in 3 dimensions, x-y and z. These ceramic materials change their dimensions if an electric field is applied to them.

In constant current mode STM operation, the tunneling current is kept constant, using a feedback circuit while we scan the surface. The feedback circuit supplies voltage (V_Z) to the z direction scanner piezo, which moves the tip with picometer resolution up and down, in order to keep the tunnel current constant. When the sample and the Hall probe chip are in close proximity, the tunneling current is achieved between the STM tip and the sample. The tip/sensor scans by applying appropriate voltages, V_x and V_y to the x and y piezoelectric scanner, the topography z (x,y) of the sample is obtained by recording V_z (x,y).

Figure A.2 shows the principle of SHPM operation. The microscope can be operated in the following modes:

a) Scanning Tunneling Microscope (STM),
b) Atomic Force Microscope (AFM), and
c) Scanning Hall Probe Microscope (SHPM).

SHPM is a quantitative and non-invasive technique for imaging “localized surface magnetic field distribution on sample surfaces” with high spatial and magnetic field resolution of about 50 nm over a wide range of temperatures from 30 mK to 300 K.

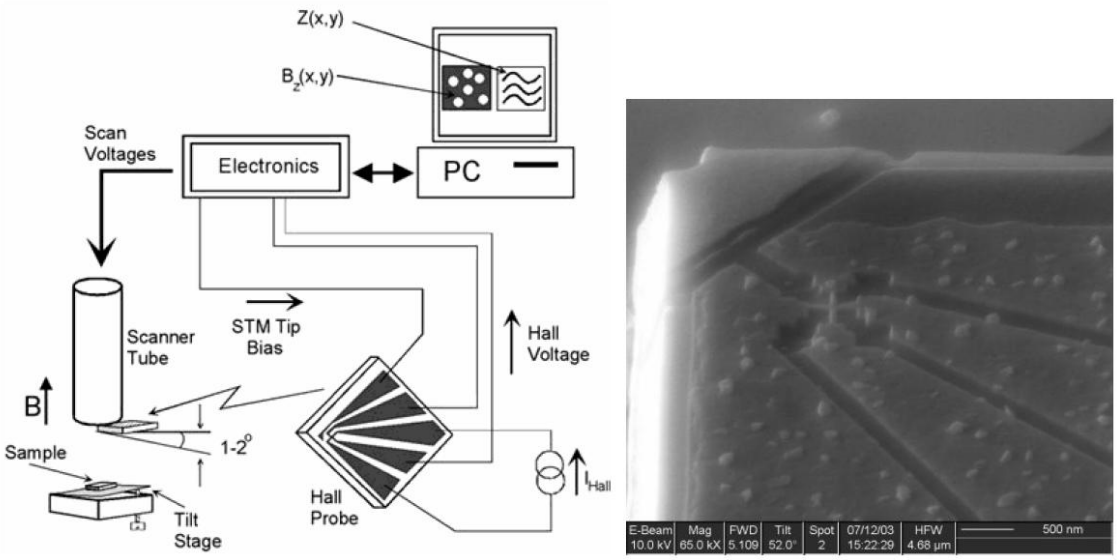

Figure A.2: Principle of SHPM and Hall Sensor [35].

In SHPM, a nano-Hall probe is scanned over the sample surface to measure the perpendicular component of the surface magnetic field using conventional STM positioning techniques as shown in Figure A.2 above.

The Hall sensor is micro fabricated close to a gold-coated corner of a deep etch mesa, which serves as an STM tip. The Hall probe chip is tilted ~1 degree with respect to sample ensuring that the corner of the mesa is the highest point.

The microscope can be run in two modes: STM tracking and lift-off mode. In the STM tracking mode, the tunnel current between the corner of the Hall sensor chip and the sample is measured and used to drive the feedback loop enabling the simultaneous measurement of both STM topography and the magnetic field. This mode of operation gives the highest sensitivity because of the smallest probe-sample separation at all times, but with the drawback of being slow. In the lift-off mode, the Hall sensor is lifted-off to a certain height above the sample and the head can be scanned extremely fast (about 4s/frame) for measurements of the local magnetic field distribution [36].

LT-SHPM insert is composed of lemo connectors, SHPM head, and the radiation shields as illustrated in Figure A.3.

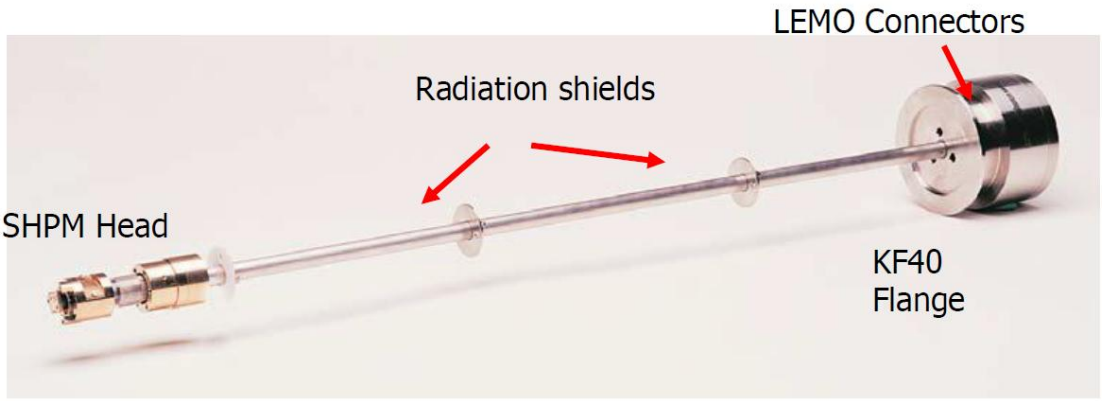

Figure A.3: LT-SHPM insert and the parts [35].

Figure A.4 shows the detailed picture of the LT-SHPM head and its components. The slider is a piezo-driven stick-slip inertial slider, which moves the slider puck along the glass tube (z-direction) and the sample holder with respect to the sample puck in x-y directions. The shield is fitted over the microscope head to protect it from impacts while it is lowered into the cryostat, as well as sustaining temperature uniformity and electrical shielding. A small coil is also wound on the shield to be able to apply small external magnetic fields.

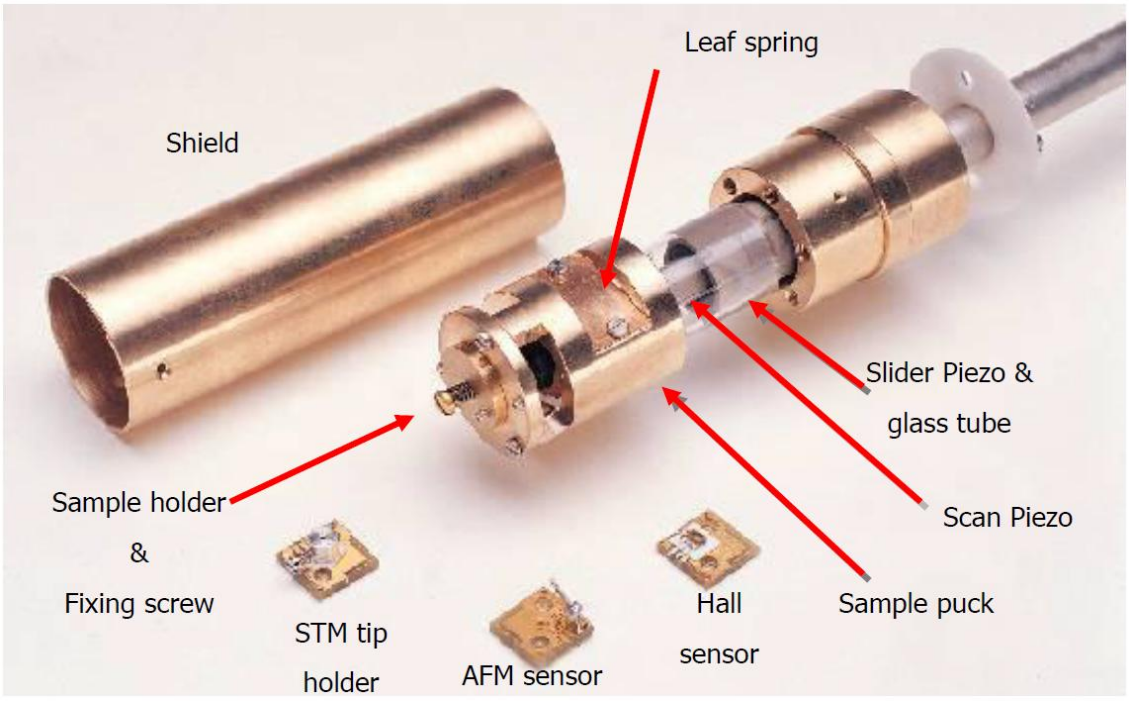

Figure A.4: Detailed view of LT-SHPM [35].

We run the microscope in STM mode first in order to get acquainted and gain confidence as the STM tips are disposable and cheap. We prepared STM tips in accordance with the following instructions:

We mounted the STM tips while the tip holder was not attached to the LT-SHPM head. We clean the STM tip holder in acetone and then dry it to get rid of any dirt and grease. Wire cutter is also cleaned before cutting the wire. We used Pt-Ir (%10) alloyed wire. We take 6-7 mm long wire piece. Holding it tight with the pliers, we cut it using the wire cutter with ~ 45° angle to the wire axis. We cut it as we pull the wire cutter. Then, we inspect the tip under the optical microscope to be sure that the tip is sharp. If it is not sharp enough, the same process is repeated. We clean the tip by squirting clean acetone and then we dry it with blowing some dry nitrogen. We put the sharpened tip into the holder and screw it tight. The tip must be secured properly in its place. The STM tip is made ready as shown in Figure A.5.

Figure A.5: STM tip [35].

The Hall sensors are shown in Figure A.6. It has an integrated STM tip fabricated on one corner of the Hall probe chip. The Hall sensor is fabricated on chip approximately 10 μm away from the STM tip. We use STM feedback to bring the Hall sensor in close proximity with the sample surface and then scan it by STM tracking without crashing or scratching the Hall sensor. This assures that the Hall probe is kept as close as possible to the sample surface without actually contacting the surface.

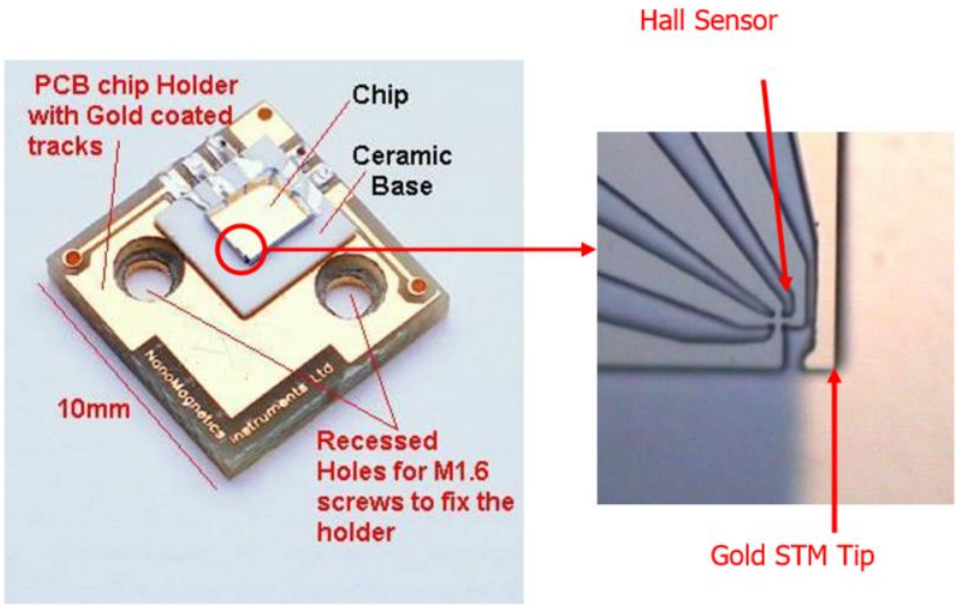

Figure A.6: Hall probe holder, Hall probe chip, Hall sensor, and STM tip [35].

Before mounting the Hall probe (HP) on the scan head, we first carefully inspect if the bonding wires are intact under 50x optical microscope, there are 2-3 bonding wires for each electrical contact for safety. Then, we inspect the active area and the tip of the Hall sensor under 200x optical microscope. We make sure that the HP and gold tip are clean, otherwise we clean it first with acetone and then with isopropyl alcohol in a very gentle ultrasonic agitation. Then, we blow dry it gently taking care about the bonding wires. We take a picture of the Hall probe with an optical microscope to record the condition of the HP before starting the experiment as shown in Figure A.7.

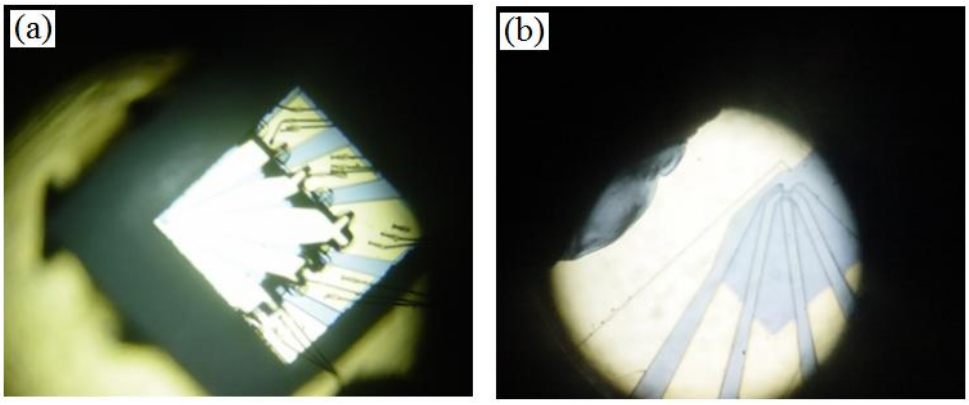

Figure A.7: Inspection of Hall sensor and gold STM tip. (a) Gold bonding wires of HP, (b) Hall sensor and gold STM planar tip on chip under optical microscope view [35].

Before mounting the sample on the sample holder, coating the sample surface with gold assures that the bias voltage between the STM tip and the sample is uniform throughout the surface. Thermal evaporation is commonly used to coat the sample surface. Later, the sample is mounted on a gold coated x-y slider puck with conductive silver paint. Continuity must be established between the gold coated sample surface and the x-y slider puck by smearing excess silver paint over the sample side to the gold layer on the sample surface. For samples that are smooth and devoid of sharp feature profiles, a 5 to 10 nm thick gold layer is sufficient. If the sample has sharp features or it is not smooth, the thickness of the gold layer must be increased to accommodate possible discontinuities in the gold layer. The sample surface needs to be cleaned typically with isopropanol and thoroughly dried with dry nitrogen flow. Cleaning the surface with acetone poses some risks to both the continuity of the silver paint and the structural integrity of the sample since silver paint and common photoresists are soluble in acetone.

The sample should have a conductive surface, free from thin oxide layers. A thin layer of oxide may grow on most samples, which can cause a false conductive measurement. This is because we pierce through the oxide with the multimeter probes when we measure it. However, this can cause a serious tip wear in the Hall sensor and make it unusable. The samples with oxidized surfaces should be coated with a thin layer of gold for long lifetime of STM tips and Hall sensors. The sample should be glued onto the sample holder (top part of xy slider) with a silver conductive paint. First, we check that the glass hemispheres attached to the xy-slider top and bottom parts are clean and not chipped. In an ultrasonic bath with acetone, we clean the xy slider (top and bottom), the sample slider, and slider puck. We mount the samples as flat as possible and allow 15-30 min for the silver paint to dry. After the paint dries, electrical continuity should be checked between the sample and sample holder using a multimeter, a resistance of about 10 ohms is sufficient. Figure A.8 illustrates the mounting of the sample on the holder, and then to the sample slider puck.

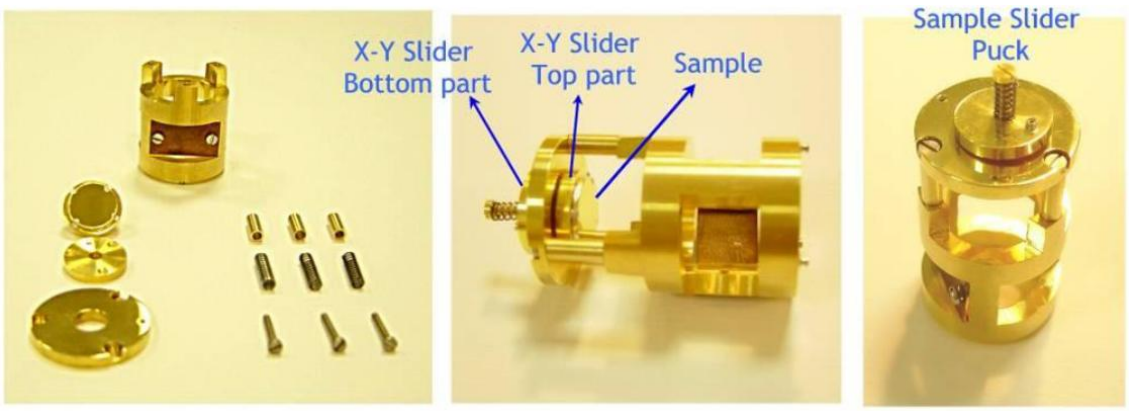

Figure A.8: Mounting the sample on the holder, and then to the puck [35].

Then, we sandwich the sample slider fixed piece between the xy-slider top and bottom parts with the M2 screw with spring as shown in Figure A.8 above. The top and bottom parts of the xy-slider have three hemispheres which slide on the fixed piece (the sample slider). We tighten the spring just enough to make sure that xy-slider can slide on fixed piece when it is jerked laterally. The assembled sample holder is then flipped over and fixed to the slider puck with three M1.6 screws and compression springs. These springs are used to align the sample-Hall probe angle. We adjust the screws to make the samples perpendicular to the cylinder axis. Then, we attach the wiring which connects the fixed piece to the xy-slider bottom part electrically using the push pins and sockets.

Then, we proceed with the next step of mounting the sample puck on the LT-SHPM. The slider puck and the glass tube on which the puck slides have to be very clean. If the glass tube is dirty, we have to use stripes of clean lint-free tissue moistened with acetone, and wipe the surface very gently as shown in Figure A.9. Cleanliness is very important to ensure proper operation at low temperatures.

Figure A.9: Cleaning the glass slider tube [35].

The slider puck is attached to the glass tube by using a leaf spring and two special M1.6 stainless steel screws. Then, we connect the wire with push pin connectors at both ends to the connector at the slider puck close to the leaf spring. This wire supplies the sample bias voltage to the puck. Loosening the screws and rotating the puck, the spring faces the earth; this should pull the spring down due to gravity. Then, gently slide the puck over the glass tube carefully avoiding contact with the tip and Hall probe. The slider puck touches the glass tube by 4 contacts at the puck body and spring itself. We stop when the 4 contacts of the puck touch the glass. Then, we rotate the whole LT-SHPM insert so that the screws fixing the spring are at the top. Then, we slowly tighten the screws one turn at a time one after another until they both are fully tight. When the screws are loose, the puck will fall or not move upward. The LT-SHPM is engineered such that the slider puck works reliably at every temperature from mK to 300 K providing that the leaf spring is fully tightened. We thread the other end of the wire through one of the holes and connect into the V_{Bias} connector at the distribution PCB positioned above the head. To check the electrical continuity, we take a piece of thin wire and gently touch it to the puck and the LT-SHPM body; this should bring the sample bias voltage displayed on the screen to zero. The sample bias voltage is short-circuited. We position the optical zoom microscope; we connect all leads of the LT-SHPM to the SPM controller and place the LT-SHPM close to the optical microscope as shown in Figure A.10.

Figure A.10: Slider operation and sample adjustment setup [35].

We switch the SPM control electronics power on and run the SPM program. The slider is driven by the stick-slip slider control card at the SPM control electronics. The card generates a special voltage pulse and multiplexed to the relevant electrodes by relays under software or keypad control. Outputs are short-circuit protected. SPM

control program is run according to the instructions set in the LT-SHPM user manual [35]. Then, we proceed with the next step of adjusting of the Hall sensor-sample angle. The sample should be tilted around 1.25° with respect to the Hall probe as shown in Figure A.11.

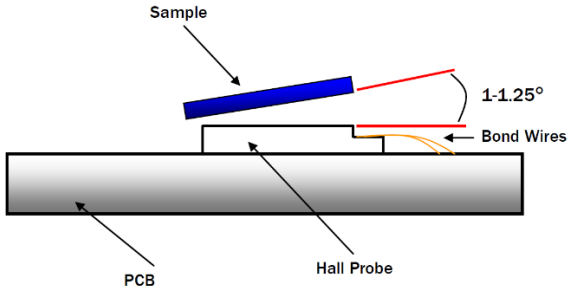

Figure A.11: Adjusting the Hall sensor-sample angle [35].

During the adjustment, we use a zoom microscope and light illumination from the bottom using a light source to view the angle. In order to ensure that the STM tip is the closest point of the Hall probe to the surface, the angle between the Hall probe chip plane and the sample surface plane must be adjusted ideally to 1.25°. Since one of the three spring loaded screws located on the top part of the slider puck was aligned earlier to be in line with the Hall probe diagonal, the angle can be adjusted to the desired value by rotating the other two set screws.

Angle adjustment is generally the most difficult and time consuming part of the preparation process. If the angle is set too shallow, the Hall probe remains too close to the sample surface and may possibly be damaged. If the angle is too steep, the probe chip corner can hit the surface without the STM tip registering tunneling current and also the Hall probe will remain too far from the surface resulting in a weaker Hall signal. We must check the angles repeatedly by rotating the microscope back and forth by 90° as the adjustment is being made.

After final adjustments are successfully completed, we set the temperature to 300 K while flushing the system with helium gas. We carefully and slowly insert the microscope into the cryostat. We use the plastic centering ring and the radiation shields as a guide during insertion so that the head is not touching anywhere in the sample space. We tighten the KF40 flange using its clamp. We flush the sample space with helium couple of times to purge all the gas trapped inside the space. The helium gas

pressure inside the sample space is never less than 1 bar. The sample space has to be flushed with pure helium gas several times and left with helium gas before cooling the system down while the control electronics is turned off. During operation, the helium gas pressure inside should not drop below about 500 mbar, otherwise HV discharges may occur, and may move the slider up resulting in damage of the Hall probes or the piezo elements. The LT-SHPM is cooled down or warmed up with a maximum rate of 2-3 K/min.

When ready to operate the microscope, we attach all the signal cables, switch on the SPM control electronics, and run the program. We first check that the communication between the electronic unit and the computer is well-established. This can be done simply by looking at the bottom left of the SPM software window. We enter the desired bias voltage and the tunneling current value. Typical values are -0.1 V and 0.5 nA, respectively. For safer operation, 0.1 V > V_{Bias} > -0.1 V range is recommended. The sample is tilted with respect to the sensor. The LT-SHPM is designed such that the upper right corner of the scan area is the highest point on the sample. Therefore, we need to approach the surface at that point. Automatic approach sequence is followed to approach the sample surface.

When the desired V_z is achieved, stability should be observed. If not stable, there is a danger that there could be some debris on the surface or the chip corner has been crashed on the sample due to a high tilt angle. If everything is fine, it is safer to do Lift-off scans. Then, we can proceed with the Fast SHPM scans where the head is scanned mush faster to get images. The images are acquired line by line and displayed on the screen as the image is formed from scan lines.

The SPM controller program automatically handles the temperature changes and adjusts itself. We read out the sample space temperature from the temperature controller. There is also a Cernox temperature sensor wired up with 4-leads to monitor the temperature of the microscope.

Imaging of Stray Magnetic Fields by SHPM:

The SHPM is used for the quantitative measurement and imaging of the perpendicular out-of-plane component of the stray magnetic fields produced by ferromagnetic micro-structures. The sample is scanned at room temperature on a piezo controlled X-Y stage at a height of approximately 5 μm above the micro-magnet arrays. The measured field profiles are used to derive the spatial variation in the field above the ferromagnetic substructures.

The ferromagnetic substructures are imaged in the presence of an in-plane magnetic field normal to the superconducting film. The amplitude of magnetic field variation is smaller than that actually present on the surface of the film due to the decay of the field strength with distance out from the film surface. These scans are taken at room temperature about 5 μm above the ferromagnetic substructures near the ends of stripe edges under the action of an in-plane magnetic field normal to the film surface. Table A.1 introduces a number of scan parameters set in an SHPM measurement.

Table A.1: SHPM scan parameters belonging to an example measurement.

Scan Parameters	
Sample	: hard disk, 80 Gb/platter
HP sensor	: 1 μm size PHEMT
Scan area	: 20 x 20 μm²
Image size	: 256 x 256 pixel²
Scan speed	: 8 μm/s
P-I-D-Div	: 100-1-1,500-14,000
Set I_tunneling	: 1,5 nA
Leakage current	: 0,9 nA
Set V_bias	: -0,1 V
Set I_Hall current	: 50 μA
R_Hall coefficient	: 0,002 ohm/G
Software gain	: 10
Bandwidth BW	: 0,1 kHz

Figure A.12 shows STM topography and SHPM images of a sample track.

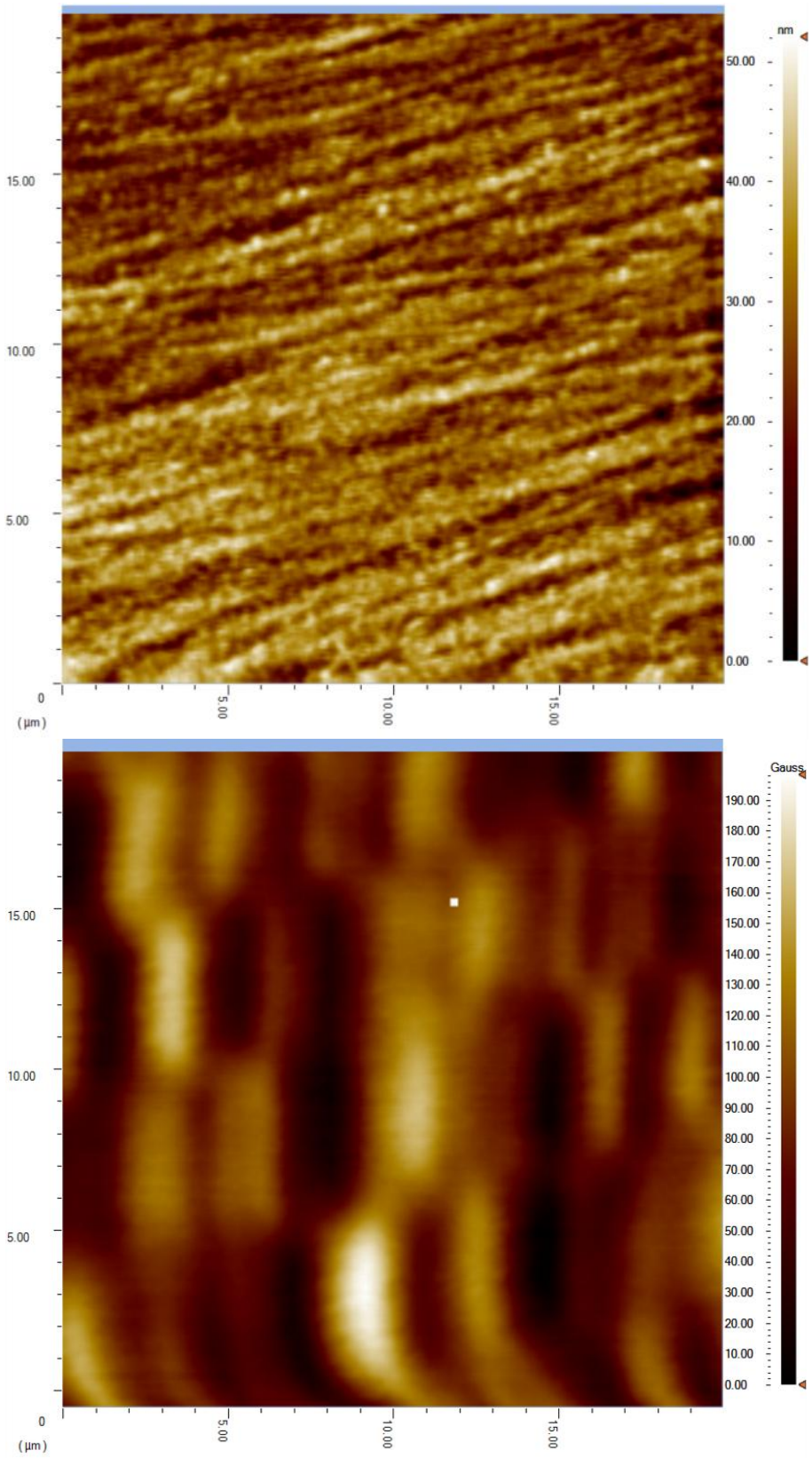

Figure A.12: STM topography (top) and SHPM images (bottom) of a sample track.

Figure A.13 shows an image at lift-mode and an SHPM image from cross section.

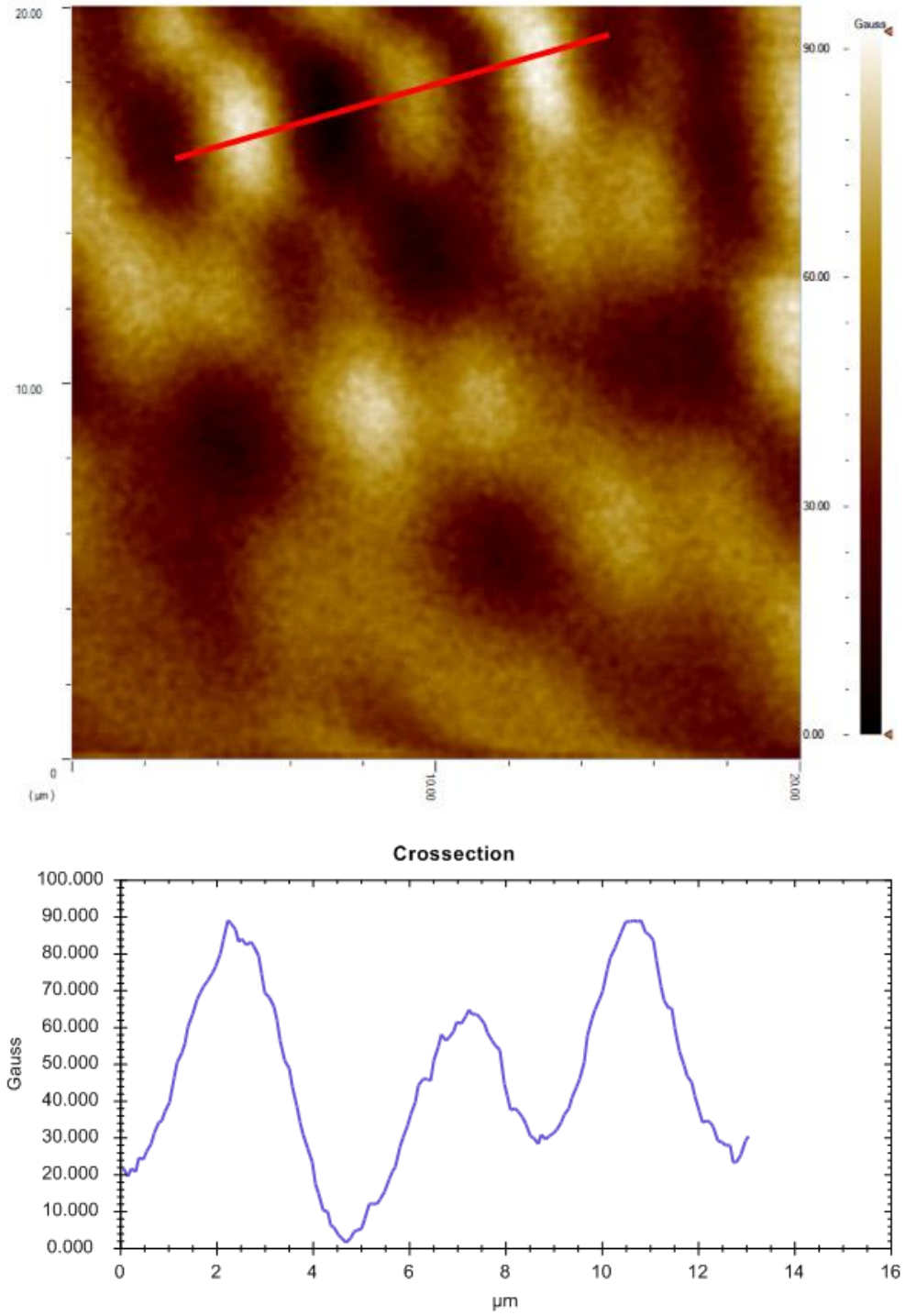

Figure A.13: Image at lift-mode (top) and SHPM image from cross section (bottom).

REFERENCES

[1] A.E. Ozmetin, M.K. Yapici, J. Zou, I.F. Lyuksyutov, and D.G. Naugle, "Micromagnet-superconducting hybrid structures with directional current flow dependence for persistent current switching", *Appl. Phys. Lett*. 95, 022506, 2009.

[2] A.E. Ozmetin, E. Yazici, K. Kim, K.D.D. Rathnayaka, I.F. Lyuksyutov, and D.G. Naugle, "Hysteresis of the phase diagram in the ferromagnet–superconductor hybrids", *Int. J. Mod. Phys. B*, Vol. 27, No.15, 2013.

[3] A.E. Ozmetin, "A method for simulating the superconducting properties in ferromagnetic–superconducting hybrid systems", *ACES, The 29th Int. Review of Progress in Applied Computational Electromagnetics*, Monterey, CA, Vol. Modelling and Simulation in Electromagnetic Engineering, 2013.

[4] A.E. Ozmetin, K.D.D. Rathnayaka, D.G. Naugle, I.F. Lyuksyutov, "Strong increase in critical field and current in magnet–superconductor hybrids", *J. Appl. Phys*. 105 (2009) 07E324.

[5] I.F. Lyuksyutov, D.G. Naugle, A.E. Ozmetin, M.K. Yapici, and J. Zou, "Vortex pinning by an inhomogeneous magnetic field", *J. of Supercond. and Nov. Magn*. 23 (6), pp.1079–1082, 2010.

[6] S. Erdin, I.F. Lyuksyutov, V.L. Pokrovsky, and V.M. Vinokur, "Topological textures in a ferromagnet–superconductor bilayer", *Phys. Rev. Lett*. 88, 017001, 2001.

[7] S. Erdin, A.F. Kayali, I.F. Lyuksyutov, and V.L. Pokrovsky, "Interaction of mesoscopic magnetic textures with superconductors", *Phys. Rev*. B 66, 014414, 2002.

[8] L.N. Bulaevskii, E.M. Chudnovsky, and M.P. Maley, "Magnetic pinning in superconductor–ferromagnet multilayers", *Appl. Phys. Lett*. 76, 2594, 2000.

[9] Z. Yang, M. Lange, A. Volodin, R. Szymczak, and V.V. Moshchalkov, "Domain-wall superconductivity in superconductor–ferromagnet hybrids", *Nature Materials* 3, pp. 793–798, 2004.

[10] M.Z. Cieplak, X. Cheng, C.L. Chien, and H. Sang, "Origin of pinning enhancement in a ferromagnet–superconductor bilayer", *J. Appl. Phys*. 97, 026105, 2005.

[11] V. Vlasko-Vlasov, U. Welp, G. Karapetrov, V. Novosad, D. Rosenmann, M.Iavarone, A. Belkin, and W.-K. Kwok, "Guiding superconducting vortices with magnetic domain walls", *Phys. Rev. B* 77, 134518, 2008.

[12] L.Y. Zhu, T.Y. Chen, and C.L. Chien, "Altering the superconductor transition temperature by domain-wall arrangements in hybrid ferromagnet–superconductor structures", *Phys. Rev. Lett*. 101, 017004, 2008.

[13] A.I. Buzdin, "Proximity effects in superconductor–ferromagnet heterostructures", *Rev. Mod. Phys*. 77, pp. 935-976, 2005.

[14] I. F. Lyuksyutov and D. G. Naugle, *Int. J. Mod. Phys. B* 17, 3713, 2003.

[15] I. F. Lyuksyutov and D. G. Naugle, *Int. J. Mod. Phys. B* 17, 3441, 2003.

[16] I.F. Lyuksyutov and V.L. Pokrovsky, "Ferromagnet–superconductor hybrids", *Adv.in Phys*., Vol.54, No.1, pp. 67–136, 2005.

[17] M. Velez, J.I. Martin, J.E. Villegas, A. Hoffmann, E.M. Gonzalez, J.L. Vicent, and I.K.Schuller, "Superconducting vortex pinning with artificial magnetic nanostructures", *J. Magn. Magn. Mater*. Vol. 320, No. 21, pp. 2547–2562, 2008.

[18] J.C.Lodder, "Patterned nanomagnetic films", in D.Sellmyer and R.Skomski (Eds.), *Advanced Magnetic Nanostructures*, Chapter 10, pp. 261-293, Springer US, 2006.

[19] M.Kustov, P. Laczkowski, D. Hykel, and et al, "Magnetic characterization of micropatterned Nd-Fe-B hard magnetic films using scanning Hall probe microscopy", *J. Appl. Phys.* Vol. 108, No. 6, pp. 063914-063914-7, 2010.

[20] F. Dumas-Bouchiat, L. F. Zanini, M. Kustov, and et al, "Thermomagnetically patterned micromagnets", *Appl. Phys.Letters*, Vol. 96, No. 10, 2010.

[21] A. A. Abrikosov, "On the magnetic properties of superconductors of the second group", *Zh. Eksp. Teor*. Vol. 32, pp. 1442–1452, Engl. transl.: *Sov. Phys. JETP*, Vol.5, pp.1174– 1182, 1957.

[22] A. A. Abrikosov, and L. P. Gorkov, "Theory of superconducting alloys with paramagnetic impurities", *Zh. Eksp. Teor*. Vol. 39, pp. 1781–1796, Engl. transl.: *Sov. Phys. JETP*, Vol. 12, pp. 1243–1253, 1961.

[23] V.K.Vlasko-Vlasov, E.Palacious, D.Rosenmann, J.Pearson, and et al, "Self-healing patterns in ferromagnetic-superconducting hybrids", *Supercond.Sci.Technol*., Vol. 28, No. 3, 035006 (8pp), 2015.

[24] A.E.Ozmetin, *Magnetic imaging of micrometer and nanometer-size magnetic structures and their flux-pinning effects on superconducting thin films*, PhD Dissertation, Texas A&M University, 2009.

[25] A.E.Ozmetin, E.Ongun, M.Kuru, and E.Yazıcı, "Fabrication and characterization of ferromagnetic-superconducting hybrid films grown by combined PVD techniques", *Proceedings of the Science and Applications of Thin Films Conference (SATF2014)*, Çeşme-İzmir, 15-19 Sep 2014, *Applied Surface Science*, Vol. 350, pp. 2-5, 2015.

[26] B.A. Peterson, W.C. Patterson, F. Herrault, D.P. Arnold, and M.G. Allen, "Laser-micro machined permanent magnet arrays with spatially alternating magnetic field distribution", *Proceedings of the 12th International Workshop on Micro and Nanotechnology for Power Generation and Energy Conversion Applications*, Atlanta, 2-5 Dec 2012, pp. 319-322, PowerMEMS 2012.

[27] Cryomagnetics, Inc., *Operating Instruction Manual for Superconducting Magnet System with Variable Temperature Insert*, Tennessee, 2012.

[28] J. Nagamatsu, N. Nakagawa, T. Muranaka, Y. Zenitani, and J. Akimitsu, "Superconductivity at 39 K in magnesium diboride," *Nature*, Vol. 410, No. 6824, pp. 63–64, 2001.

[29] W. N. Kang, H. J. Kim, E. M. Choi, C. U. Jung, and S. I. Lee, "MgB_2 superconducting thin films with a transition temperature of 39 K," *Science*, Vol. 292, No. 5521, pp. 1521–1523, 2001.

[30] S. H. Moon, J. H. Yun, H. N. Lee, and et al., "High critical current densities in superconducting MgB_2 thin films," *Applied Physics Letters*, Vol. 79, No. 15, pp. 2429–2431, 2001.

[31] J.Rowell, "Magnesium diboride: Superior thin films," *Nature Materials*, Vol. 1, No. 1, pp. 5–6, 2002.

[32] S.Fabretti, P.Thomas, M.Meinert, I.-M.Imort, and A.Thomas, "Fabrication of superconducting MgB_2 thin films by magnetron co-sputtering on (001) MgO substrates", *J. of Supercond. and Nov Magn.*, Vol 26, No. 5, pp 1879-1882, 2013.

[33] H.Shimakage, K.Tsujimoto, Z.Wang, and M.Tonouchi "All-MgB_2 tunnel junctions with aluminum nitride barriers", *Applied Physics Letters*, Vol. 86, No. 7, 072512 (3 pages), 2005.

[34] A.E.Ozmetin, O.Sahin, E.Ongun, M.Kuru, "Mechanical characterization of MgB_2 thin films using nanoindentation technique", *Journal of Alloys and Compounds*, Vol. 619, pp. 262-266, 2015.

[35] NanoMagnetics Instruments, *Introduction to Low-Temperature Scanning Hall Probe Microscope (LT-SHPM), and User Manual*, www.nanomagnetics-inst.com.

[36] A. Oral, S. J. Bending, and M. Henini, "Real time scanning Hall probe microscopy", *Appl. Phys. Lett*. Vol. 69, No. 9, pp. 1324-1326, 1996.